

AD-784 962

LONG RANGE MATERIALS RESEARCH

Robert A. Huggins

Stanford University

Prepared for:

Advanced Research Projects Agency

30 June 1974

DISTRIBUTED BY:

**NTIS**

**National Technical Information Service  
U. S. DEPARTMENT OF COMMERCE  
5285 Port Royal Road, Springfield Va. 22151**

**FIRST ANNUAL TECHNICAL REPORT**

**July 1, 1973 - June 30, 1974**

**Long Range Materials Research**

**Sponsored by  
Defense Advanced Research Projects Agency  
ARPA Order No. 2470**

**Program Code Number: 3D10**

**Contractor: Stanford University**

**Effective Date of Contract: June 1, 1973**

**Contract Expiration Date: May 31, 1975**

**Amount of Grant: \$429,000**

**Grant Number: DAH C15 73 G15**

**Principal Investigator: Robert A. Huggins  
Phone: (415) 497-4118**

**Short Title: Long Range Materials Research**

**The views and conclusions contained in this document are those of the authors and should not be interpreted as necessarily representing the official policies, either expressed or implied, of the Defense Advanced Research Projects Agency or the U. S. Government.**

Reproduced by  
**NATIONAL TECHNICAL  
INFORMATION SERVICE**  
U S Department of Commerce  
Springfield VA 22151

**Center for Materials Research  
Stanford University  
Stanford, California 94305  
(415) 497-4118**

178

## TABLE OF CONTENTS

I. INTRODUCTION	1
II. GENERATION OF COHERENT VACUUM ULTRAVIOLET AND SOFT X-RAY RADIATION	3
S. E. Harris, J. F. Young, and A. H. Kung	
A. Introduction	4
B. Generation of Vacuum Ultraviolet Radiation	4
C. Tunable Vacuum Ultraviolet Radiation	5
D. Harmonic Generation at High Field Strengths	10
E. Holography in the Vacuum Ultraviolet	12
F. References	14
III. DETECTION OF X-RADIATION	16
C. W. Bates, Jr.	
A. Introduction	17
B. Research Progress to Date	18
C. References	20
IV. SUPERPLASTICITY AND WARM WORKING OF PLAIN HIGH CARBON STEELS	21
O. D. Sherby, J. C. Shyne, C. M. Young, and B. Walser	
1. <u>Warm Working and Superplasticity of Plain High Carbon Steels</u>	22
A. Introduction	22
B. Processing	23
C. Elevated Temperature Deformation	24
D. Electron Transmission Studies of the 1.9% Carbon Steel	32
E. Ambient Temperature Properties	39
F. References	46
2. <u>Breakdown of Lamellar Microstructures During Warm Working</u>	47
V. SUPERPLASTICITY OF Pb-Sn AND Pb-Sn-Au ALLOYS	50
C. R. Barrett and A. E. Geckinli	

VI. SYNTHESIS OF NEW TYPES OF CATALYST MATERIALS	53
J. P. Collman, M. Boudart, D. N. Marquardt, J. G. Fripiat, K. T. Chow, J. B. Diamond, and K. H. Johnson	
1. <u>Synthesis and Characterization of Supported Organometallic Radium(I) Catalysts</u>	54
2. <u>Structure Insensitive and Structure Sensitive Catalytic Reactions</u>	55
3. <u>The Structure and Bonding of Lithium Clusters</u>	58
A. Introduction	58
B. Results and Discussion	65
(1) Equilibrium internuclear distance	65
(2) Spin-orbital levels of the clusters	74
(3) Binding energy and other data	83
C. References	90
VII. DEVELOPMENT OF ELEVATED TEMPERATURES ELECTROCRYSTALLIZATION TECHNIQUES	91
I. V. Zubeck, P. A. Pettit, U. Cohen, R. C. DeMattei, R. S. Feigelson, and R. A. Huggins	
A. Introduction	92
B. Investigation of the LaB <sub>6</sub> System	94
C. Electrodeposition of Niobium Alloys Superconductors from Molten Fluorides	116
D. Continuous Growth	158



# **1. INTRODUCTION**

## I. INTRODUCTION

This is the first annual technical report on the research program entitled "Long Range Materials Research," covering the period June 1, 1973 through May 31, 1974. This program is composed of four separate programs as follows:

1. Harmonic Generation and Detection of X-Ray Radiation
2. Superplasticity and Warm Working of Metals and Alloys
3. Synthesis of New Types of Catalyst Materials
4. Development of Elevated Temperature Electrocrystallization Techniques

Progress in each of the subareas during the first year of this program will be described separately in the succeeding sections of this report.

**II. GENERATION OF COHERENT VACUUM ULTRAVIOLET  
AND SOFT X-RAY RADIATION**

**S. E. Harris**  
**Professor of Electrical Engineering**

**J. F. Young**  
**Research Associate, Hansen Laboratories**

**and**

**A. H. Kung**  
**Research Associate, Hansen Laboratories**

## A. Introduction

In the present report we summarize the status of our various programs aimed at the development of techniques for the generation of coherent ultraviolet, vacuum ultraviolet and soft x-ray radiation. Results of a program aimed at the application of this radiation to sub-micron fabrication and to holographic microscopy will also be reported.

During the past twelve months, we have demonstrated efficient third harmonic generation of high power, high energy pulses at  $1.06\mu$  into the ultraviolet, we have generated continuously tunable radiation in the vacuum ultraviolet using a newly developed high power broadly tunable visible source. In application, we have produced a holographic grating with a fringe spacing of  $836 \text{ \AA}$  and recorded far-field Fraunhofer holograms of sub-micron particles. Details of these results appear in subsequent sections.

We note that the present program is supported both by the Advanced Research Projects Agency and the Office of Naval Research.

## B. Generation of Vacuum Ultraviolet Radiation

The technique of phase matched harmonic generation in gases was first proposed and demonstrated two years ago in this laboratory. Since then we have obtained up to 10% energy conversion efficiency in a Rb-Xe mixture for the process of third harmonic generation from  $1.064\mu$  to  $3547 \text{ \AA}$ . The technique has also been extended into the vacuum ultraviolet region. In early experiments, we employed a phase-matched mixture of Cd and Ar in the



ratio of 1 part Cd to 25 parts Ar to generate 1773 Å. Subsequent experiments have yielded 1520 Å and 1182 Å. For radiation shorter than 1470 Å, we found that a mixture of inert gases could be used. By using the technique of continuous circulating system to allow dynamic mixing of 1 part xenon to 10.5 parts argon we have successfully generated the third harmonic of 3547 Å at 1182 Å with demonstrated phase matching output power enhancement of up to  $10^4$ . Careful pump depletion measurements have verified that better than 1% energy conversion for this process has been achieved. Power dependence measurements and linear absorption measurements at 1182 Å indicate that the parameters used have reached the saturation regime. By lengthening the interaction region and operating at lower total pressures we believe that higher conversion efficiencies can be obtained. However, the large absorption cross-section by xenon at 1182 Å may limit the ultimate efficiency of this process due to loss in the inactive regions. Until the efficiency of the 1182 Å conversion process can be improved the approach of cascading several efficient third-order nonlinear processes to shorter wavelengths will have to shift from depending on having high power densities at 1182 Å. At present the shortest wavelength generated by this technique is 887 Å (Fig. 1).

#### C. Tunable Vacuum Ultraviolet Radiation

An alternate approach toward generation of soft x-ray radiation is to make use of resonantly enhanced nonlinear optical susceptibilities to obtain very high conversion efficiencies with relatively low input power.

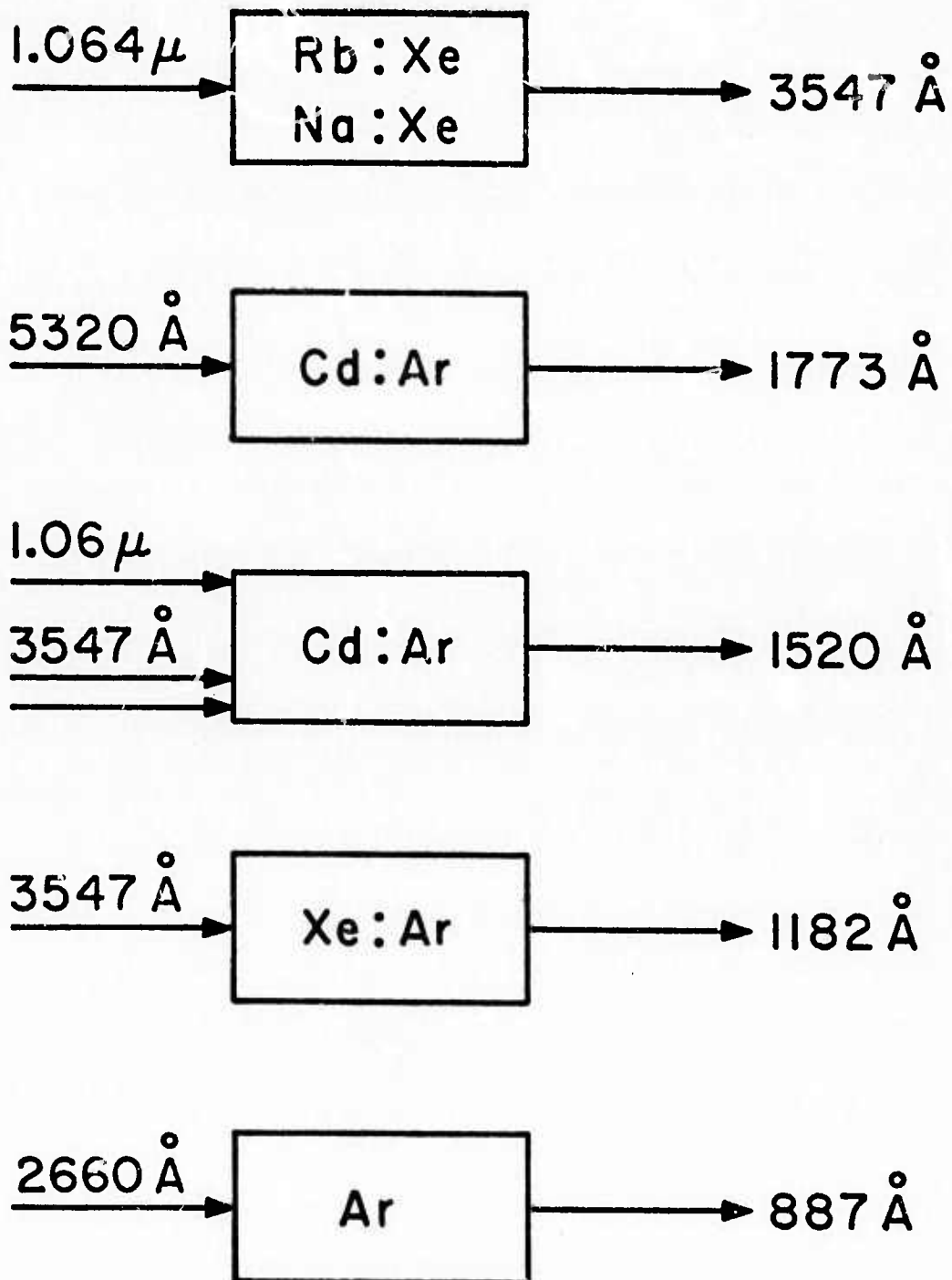


Fig. 1--Summary of experiments for generation of vacuum ultraviolet radiation.

Toward this goal, we have recently completed the construction of a high power tunable picosecond source using a quadrupled Nd:YAG laser pumped ammonium dihydrogen phosphate parametric generator-amplifier arrangement. By changing the phase-matching temperature of the ADP crystals, continuously tunable radiation from 4200 Å to 7200 Å with typical bandwidths of 2 Å has been generated. The pulse width is estimated to be approximately 50 picoseconds and the peak power is more than 1 megawatt. By focusing tight the radiation from this source into a cell containing pure xenon at 100 torr, we have obtained tunable radiation spanning the region from 1180 Å to 1950 Å (Fig. 2). Additional dye amplifiers can be inserted eventually to boost the power output of the tunable source. Etalons and spatial filters could be inserted to improve the temporal and spatial coherence of the beam. Ultimately, we will use this same source to generate 1202 Å. Two photons of 1202 Å is resonant with the 1s-2s transition in helium and will allow efficient generation into the 400 Å region. For this process, we calculate that the two-photon absorption allowed incident power density to be  $2 \times 10^{10} \text{ W/cm}^2$ . Thus, for a cell containing 10 torr of helium, corresponding to an interaction length of approximately 1 cm due to absorption at 401 Å by helium, the required incident peak power at 1202 Å will be  $5 \times 10^4$  watts and the resulting conversion efficiency will be  $10^{-4}$ . The output power will increase linearly with input power beyond this operating point due to linear absorption at the third harmonic (Fig. 3). In a related experiment, employing resonant two-photon pumping, we have up-converted infrared radiation at 10.6μ and 9.26μ to the near ultraviolet at 3321 Å and 3305 Å with photon conversion in excess of 50%. Other

# TUNABLE VUV

$$\begin{aligned}\omega_i &= 7200\text{\AA} \longrightarrow 5320\text{\AA} \\ \omega_s &= 5320\text{\AA} \longrightarrow 4200\text{\AA} \\ \omega_p &= 2660\text{\AA}\end{aligned}$$

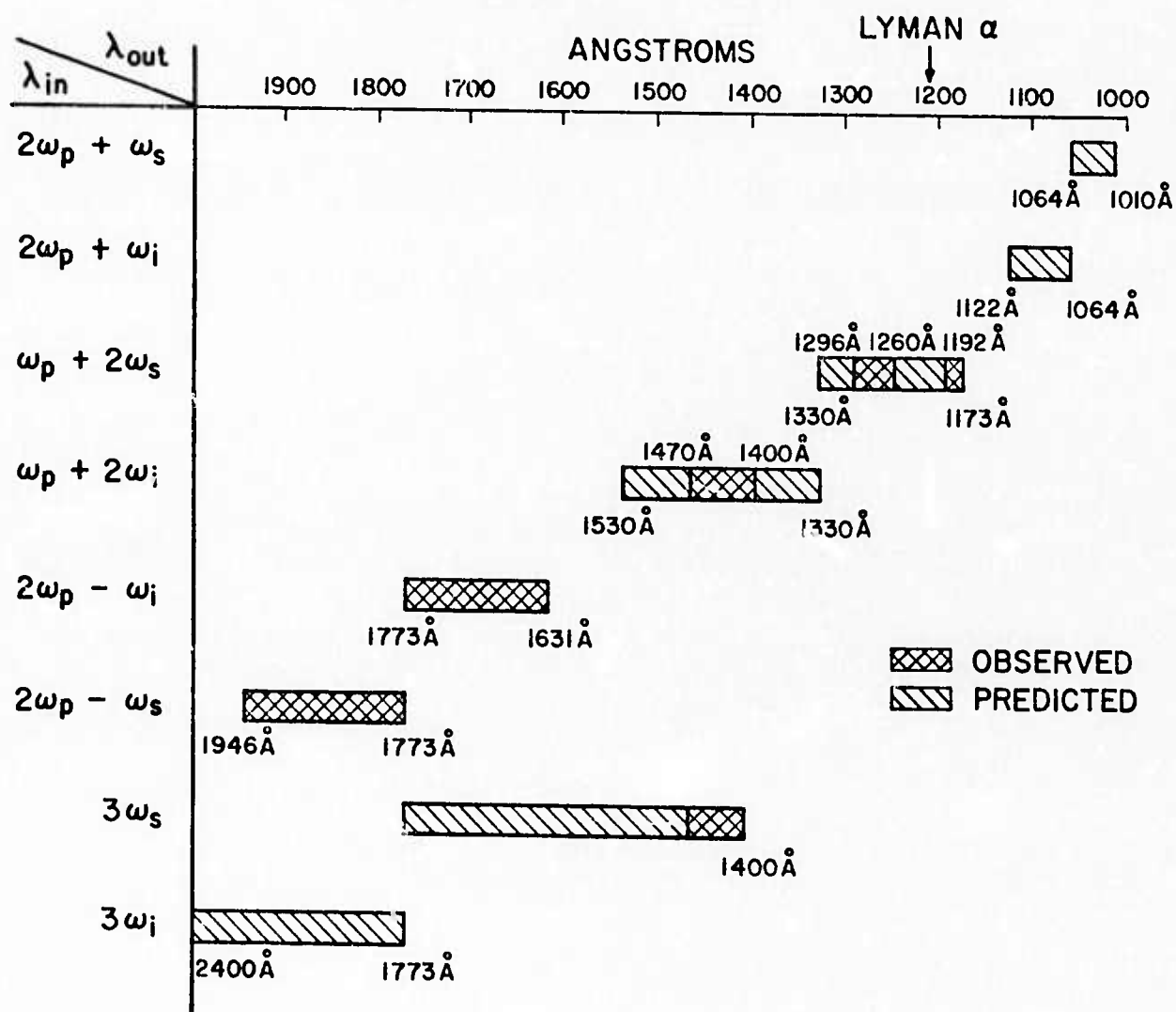


Fig. 2--Results of tunable VUV generation in pure xenon.



# 401 Å GENERATION IN He

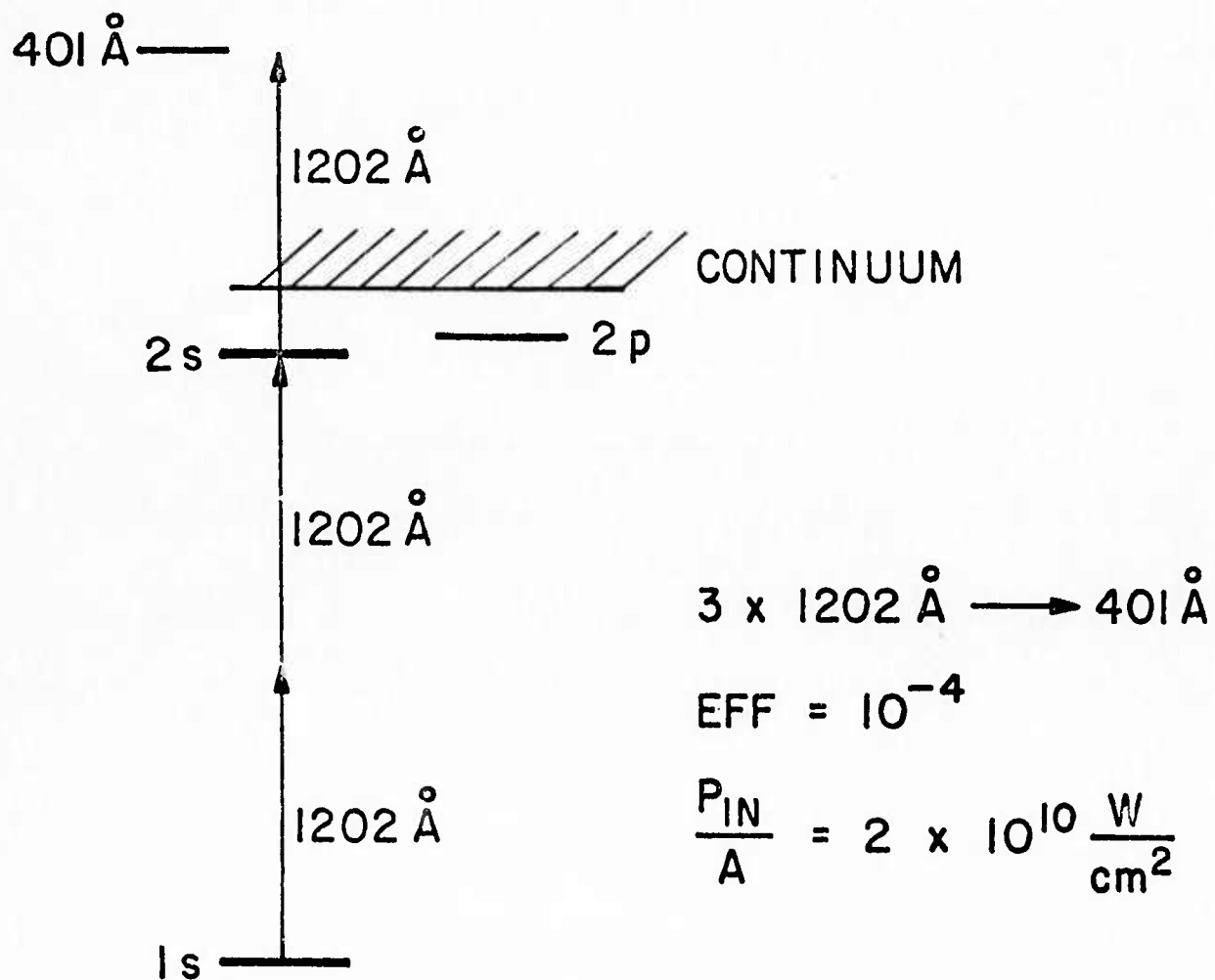


Fig. 3--Proposed scheme of 401 Å generation in He.

applications of the tunable source include study of singly ionized metal vapor as a generation medium, far infrared generation, coherent source for high power electron beam pumped excimer amplifiers and picosecond spectroscopy.

#### D. Harmonic Generation at High Field Strengths

Due to the lack of intermediate resonances or suitable atomic species, harmonic generation into the vacuum ultraviolet or soft x-ray region usually requires power densities of at least a few times  $10^{10}$  watts/cm<sup>2</sup> and very often more than  $10^{12}$  watts/cm<sup>2</sup>. It is known that at these field strengths the energy levels of an atomic system show intensity dependent shifts. By using the density matrix formalism we have in the past year performed a general analysis of the resonance positions of an atomic system in the presence of an intense electromagnetic field and its effect on harmonic generation in atomic vapors. We found that with the ability to predict the amount of frequency shift, it is possible to allow the atomic system to shift into resonance with harmonics of the incident frequency and thus generate efficiently the higher harmonics. As an example we considered the generation of 198 Å by a five-photon mixing process in Li<sup>+</sup> (Fig. 4). By initially tuning the incident frequency such that four times this frequency is about 3000 cm<sup>-1</sup> from the unshifted 2s level of Li<sup>+</sup>, we showed that at a power density of  $4.9 \times 10^{14}$  W/cm<sup>2</sup> the system becomes four-photon resonant and conversion efficiency of about 10% is possible. It should be noted though that the resonances are very sharp and hence a high power laser with amplitude stability of better than 1% is required.

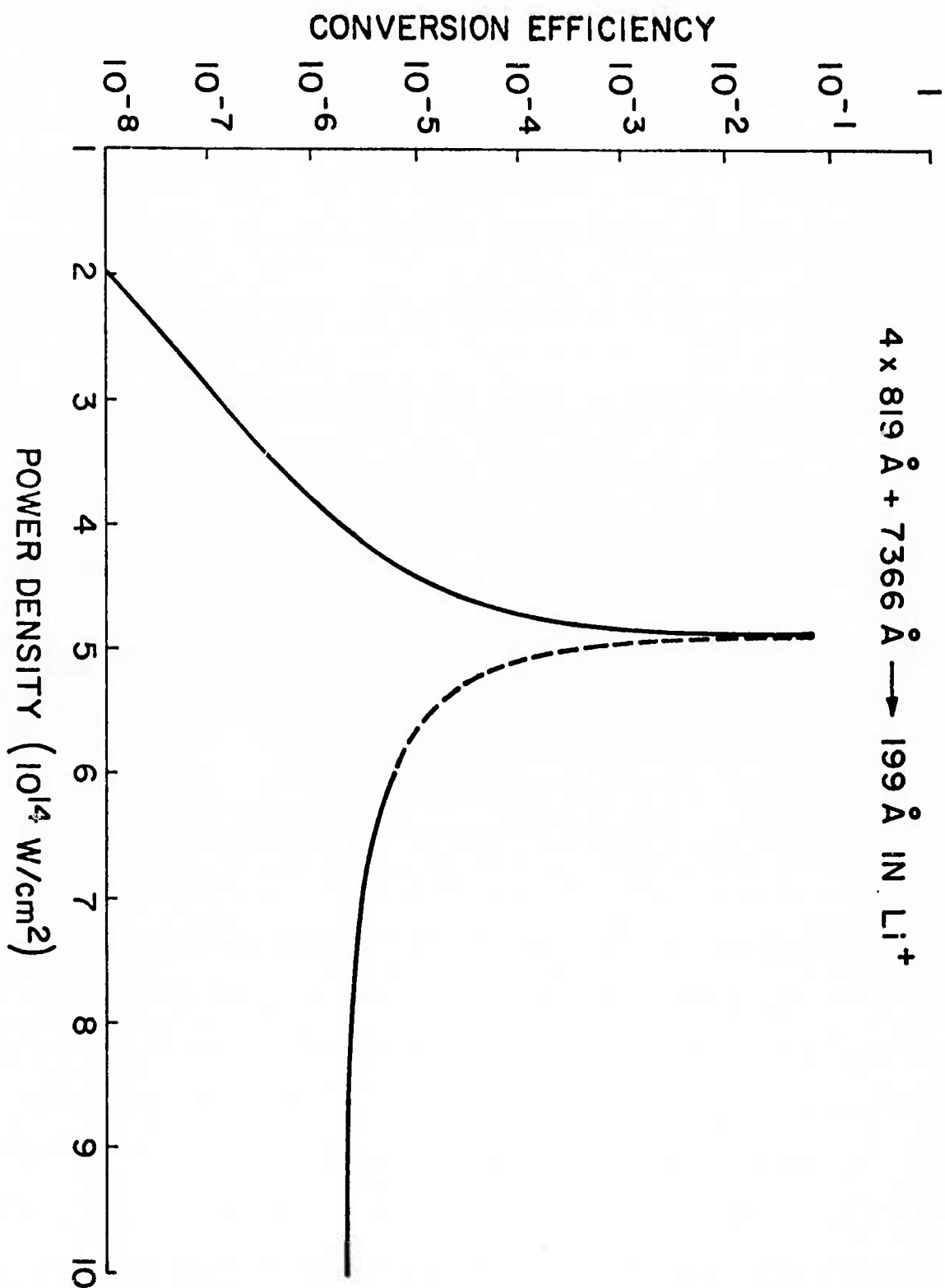


Fig. 4--Conversion efficiency for generation of 199 Å radiation using a 5-photon mixing process. In the dashed region the medium is positively dispersive.

### E. Holography in the Vacuum Ultraviolet

We have conducted an exploratory study of the feasibility of using coherent vacuum ultraviolet radiation for holography. This work has led to the first demonstration of holographic techniques in the vacuum ultraviolet spectral region. Coherent 1182 Å radiation was used to produce a holographic grating with a fringe spacing of 836 Å and to record far-field Fraunhofer holograms of sub-micron particles. The holograms were recorded in polymethyl methacrylate (PMMA) and read out with an electron microscope.

The resolution capabilities of PMMA were evaluated by recording a series of holographic gratings with progressively finer fringe spacings. The finest fringe spacing produced was 836 Å (Fig. 5). This high resolution capability makes it possible to use simple holographic recording geometries which allow large angles of interference between the reference and object waves and which do not require VUV optical components of diffraction limited quality.

Far-field Fraunhofer holograms of latex spheres ranging in diameter from 1.305 μ to 0.365 μ were recorded. The spheres were supported about 25 μ above the PMMA recording medium and illuminated with a single beam of 1182 Å radiation. A scanning electron microscope was used to read out the holographic fringe patterns.

There are several possible applications of this work to the fields of microfabrication and microbiology. Direct applications for holographic gratings with very fine fringe spacings exist in the fields of integrated optics, microwave acoustics, and the study of superlattices. Biological



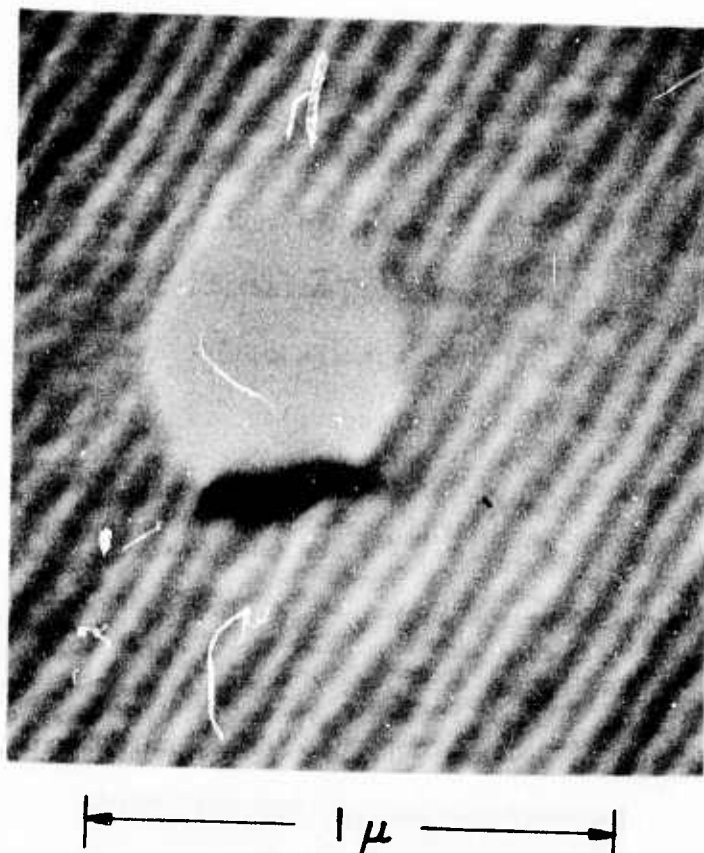


FIG. 5--SEM read out of 836 Å spaced fringes produced in PMMA by 1182 Å radiation. The round object is a 0.500μ diameter latex sphere placed on the fringes after development for magnification calibration. (25 KV electron potential, 80° sample tilt).

subjects such as cellular fine structure and viruses, heretofore observable only by electron microscopy, lie in the resolution range of VUV holography. Since some VUV wavelengths pass through centimeters of air, it might eventually be possible to examine living specimens.

This holography project was primarily supported by the JSEP.

#### F. References

1. S. E. Harris, J. F. Young, A. H. Kung, D. M. Bloom, and G. C. Bjorklund, "Generation of Ultraviolet and Vacuum Ultraviolet Radiation," Proceedings of the Laser Spectroscopy Conference, Vail, Colorado, June 1973.
2. S. E. Harris, "Generation of Vacuum Ultraviolet and Soft X-Ray Radiation Using High Order Nonlinear Optical Polarizabilities," Phys. Rev. Letters 31, 341 (August 1973).
3. S. E. Harris, A. H. Kung, E. A. Stappaerts, and J. F. Young, "Stimulated Emission in Multiple Photon Pumped Xenon and Argon Excimers," Appl. Phys. Letters 23, 232 (September 1973).
4. S. E. Harris and D. M. Bloom, "Resonantly Two-Photon Pumped Frequency Converter," Appl. Phys. Letters 24, 229 (March 1974).
5. D. M. Bloom, James T. Yardley, J. F. Young, and S. E. Harris, "Infrared Up-Conversion With Resonantly Two-Photon Pumped Metal Vapors," Appl. Phys. Letters 24, 427 (May 1974).
6. S. E. Harris and D. B. Lidow, "Nonlinear Optical Processes by van der Waals Interaction During Collision," Phys. Rev. Letters (submitted for publication).

7. G. C. Bjorklund, S. E. Harris, and J. F. Young, "Vacuum Ultraviolet Holography," Appl. Phys. Letters (submitted for publication).

8. E. A. Stappaerts, "Harmonic Generation at High Field Strengths, Frequency Shifts and Saturation Phenomena," Phys. Rev. (submitted for publication).

### **III. DETECTION OF X-RADIATION**

**C. W. Bates, Jr.**

**Associate Professor of Materials Science  
and Engineering**



## A. Introduction

Sodium activated cesium iodide CsI(Na) is one of the most rugged, stable and efficient room temperature alkali halide scintillator materials to come along in recent years (1965). Its large x-ray stopping power relative to the other alkali halides, its high conversion efficiency (12%) at its emission maximum of  $4200 \text{ \AA}$  makes it an ideal detector of x-rays in conjunction with a photocathode surface, radiographic film or a photomultiplier tube. It has made x-ray sensing systems employing zinc sulphide or calcium tungstate almost extinct<sup>(1,2)</sup>. Its narrow spectral output when bombarded by particles in the mev. range makes it also an excellent nuclear particle detector<sup>(3-19)</sup>. In spite of its immense practical possibilities and current uses, little work has been done on determining the specific luminescent mechanism in this material. As experimental techniques become more refined, it is becoming increasingly obvious that many of the activated alkali-halide which were originally thought to be well understood, such as KI(Tl) and KCl(Tl) need to be re-examined<sup>(20)</sup>. Another reason for studying CsI(Na) is that in at least one way, it is a simpler system to study than the thallium activated alkali halides. In CsI(Na), the emission at  $4200 \text{ \AA}$  cannot be due to transitions between crystal field split levels of the sodium ion in the CsI host crystals because no such levels exist to give this emission. The luminescent mechanism can thus be due to a trapping of a center or complex, already existing in the crystal by the sodium ion, or the creation of a center or complex due to the introduction of the sodium. In the thallium activated materials, evidence exists that the emission is due to transitions between crystal field split states of the thallium ion as well as the center responsible for the intrinsic emission in these crystals<sup>(20)</sup>. Thus CsI(Na) offers the unique possibility of studying centers responsible for the intrinsic emission

in the alkali halides at temperatures higher than normally observed, without the complicating effects of other emissions.

#### B. Research Progress to Date

We have measured the absorption, emission and excitation spectra of thin ( $\sim 1000 \text{ \AA}$ ) and thick ( $\sim 2\text{mm}$ ) samples of pure CsI and CsI(Na) with sodium concentrations between 0.01 and 1 mole percent at room, dry ice, and liquid nitrogen temperatures. We are planning to extend these measurements to liquid helium temperatures.

Our principal results can be summarized as follows:

##### Absorption

- (1) All measurements of absorption on pure CsI (Merck Suprapur) at room and liquid nitrogen temperatures are in agreement with previous measurements made on this material<sup>21,22</sup>, i.e. two exciton bands centered at  $2050 \text{ \AA}$  and  $2150 \text{ \AA}$  respectively.
- (2) The sodium activated material behaves quite similar to CsI doped with divalent cationic impurities like  $\text{Ca}^{++}$ ,  $\text{Sr}^{++}$ ,  $\text{Mn}^{++}$  and  $\text{Mg}^{++}$ , i.e. the shape of the tail of the fundamental absorption edge is strongly modified over that of the pure material. In particular an absorption band centered at about  $2500 \text{ \AA}$  is present in CsI (Na) which is not present in pure CsI and the intensity of this band is a function of heat treatment, the intensity being maximum for those samples which are tempered at  $150^\circ\text{C}$  for several minutes (1/2 hour) and then slowly cooled to room temperature. It is tempting at this time to suggest that the luminescent mechanism is the same for CsI(Na) and CsI doped with divalent cationic impurities. Because of the smaller size of their ions Na, Ca, Sr, etc. are expected to enter the CsI host interstitially giving rise to Cs vacancies and the possibilities for the position of localized excitons in the vicinity of such cation-cationic vacancy complexes has been

discussed previously.<sup>22</sup> However, the temperature dependence of the luminescence for the CsI with divalent cationic impurities is opposite to that of CsI(Na), i.e. it increases as one goes to lower temperatures, whereas the luminescence of CsI(Na) decreases as one lowers the temperature. Another important difference between the absorption of CsI(Na) and CsI doped with divalent cationic impurities is that the absorption peak occurring for CsI(Na) on the tail of the fundamental absorption is detectable at sodium concentrations of 6ppm, whereas for the divalent impurities one has to have about 100ppm for the peak to become observed.

#### Emission and Excitation

- (1) No emission at room temperature occurs for pure CsI.
- (2) A single emission at  $4200 \text{ \AA}$  occurs for CsI(Na).
- (3) As one lowers the temperature to liquid nitrogen temperature one sees the normal excitonic emissions in both pure CsI and CsI(Na). The  $4200 \text{ \AA}$  emission which occurs at room temperature is considerably reduced in magnitude and shifts to  $\sim 3900 \text{ \AA}$ .
- (4) If one lowers the temperature to liquid nitrogen and then heats the sample back up to room temperature one observes the appearance of two overlapping emission bands centered  $4400 \text{ \AA}$  and  $3920 \text{ \AA}$ . This occurs in both pure CsI and CsI(Na) but only in thin films of these materials ( $\sim 1000 \text{ \AA}$ ). Films 2mm thick do not show this emission and it is postulated that this emission is strain-induced. We are not aware that this has been reported on in the literature in this field. We are pursuing this as a separate investigation.
- (5) Excitation spectra for thin films of CsI and CsI(Na) have been taken, but we are still in the process of interpreting the results.

Future work will center on taking data at liquid helium temperatures.

C. References

1. C. W. Bates, Jr., Adv. in Electronics and Electron Physics 28a, 545, (1969).
2. C. W. Bates, Jr., Applied Optics 12, 938 (1973).
3. R. Hofstadter, Phys. Rev. 74, 100 (1948); 75, 976 (1949).
4. H. Kallmann, Phys. Rev. 75, 623 (1949).
5. E. C. Farmer, H. B. Moore, and C. Goodman, Phys. Rev. 76, 454 (1949).
6. C. E. Mandeville, and H. O. Albrecht, Phys. Rev. 80, 299 (1950).
7. R. Hofstadter, J. A. McIntyre, and H. I. West, Phys. Rev. 82, 749 (1951).
8. M. Furst and H. Kallman, Phys. Rev. 82, 964 (1951).
9. J. Bonanomi and J. Rossel, Helv. Phys. Acta. 25, 725 (1952).
10. W. Van Sciver and R. Hoffstadter, Phys. Rev. 87, 522 (1952).
11. B. Hahn and J. Rossel, Helv. Phys. Acta 26, 271, 803 (1953).
12. J. Schenck, Nature 171, 518 (1953).
13. A. W. Schardt and W. Bernstein, AEC Report BNL 1156 (1953).
14. F. S. Eby and W. K. Jentschke, Phys. Rev. 96, 911 (1954).
15. W. Van Sciver and R. Hofstadter, Phys. Rev. 97, 1181 (1955).
16. W. Van Sciver IRE Trans. on Nucl. Sci. NS-3, 39 (1956).
17. W. Van Sciver and L. Bogart, IRE Trans. on Nucl. Sci. NS-5, 90, (1958).
18. W. Van Sciver, Phys. Rev. 120, 1193 (1960).
19. F. S. Mozer, E. Bogott, and C. W. Bates, Jr., IEEE Trans. on Nucl. Sci. NS-15, 144 (1968).
20. J. Donahue and K. Teegarden, J. Phys. Chem. Solids 29, (1968).
21. J. E. Eby et. al., Phys. Rev. 116, 1099 (1959).
22. H. Lamatsch et.al., Phys. Stat. Sol. 41, 605 (1970); *ibid* 46, 687 (1971); *ibid* 48, 311 (1971).

**IV. SUPERPLASTICITY AND WARM WORKING  
OF PLAIN HIGH CARBON STEELS**

**O. D. Sherby**

**Professor of Materials Science  
and Engineering**

**J. C. Shyne**

**Professor of Materials Science  
and Engineering**

**C. M. Young**

**Research Associate, Materials Science  
and Engineering**

**and**

**B. Walser**

**Research Associate, Materials Science  
and Engineering**



# 1. Warm Working and Superplasticity of Plain High Carbon Steels

C. M. Young, B. Walser, E. Cady, S. Kayali and O. D. Sherby

## A. Introduction

During the past year our research has centered on a study of three unique new high carbon steels containing finely spheroidized cementite. It has been possible to produce these innovative microstructures in 1.3%C, 1.6%C and 1.9%C steels by various thermal-mechanical treatments in the warm range of temperatures (0.3 to 0.6 of the melting temperature). The recent addition of a 2.3%C steel combined with prior research on a 0.8%C steel extends the scope of this investigation on the properties of alpha iron containing a dispersion of spheroidized cementite from 12 v/o  $\text{Fe}_3\text{C}$  to 34.5 v/o  $\text{Fe}_3\text{C}$ . Since most steels contain carbon in the range 0.2 to 0.3 percent these high carbon materials are a clear departure from the nominal compositions used for structural steels and are approaching carbon compositions commonly thought of as cast irons. Our investigations have shown that these spheroidized high carbon steels have exceptional formability at elevated temperature as well as excellent ambient temperature properties, thus making these steels attractive to both the fabricator and the user. Commercial castings of these steels were obtained from a local foundry which had no experience in casting such high carbon materials. Yet, the properties obtained on these first castings indicate the tremendous potential inherent in this class of materials when all of the processing variables are understood and controlled. The low material cost (no deliberate alloying elements other than carbon) and the simple processing are definite attributes of these materials. The most exploitable

property of these spheroidized high carbon steels may be their high hardness and concomitant resistance to wear. These properties should make these steels ideal for slave dies, easily formed from master dies, for use in tooling and forming operations. Structural application with requisite complex shapes are other possible uses for these alloys.

In the following sections the processing technique to produce the spheroidized microstructures will be described first (Section A) followed by a section on elevated temperature properties (Section B) and microstructural features (Section C) and finally by a section describing the ambient temperature properties (Section D).

#### B. Processing

Several distinct thermal-mechanical processing techniques have been utilized to produce fine dispersions of cementite in these high carbon steels. In all cases, the key step to producing the fine spheroidized structures has been warm working. [We define warm temperature to be in the range  $0.35 - 0.65 T_m$ , where  $T_m$  is the absolute melting temperature of the material]. The warm range of temperature is important for the following reasons: (1) Atom mobility is enhanced by concurrent straining<sup>(1)</sup> to such a level that microstructural changes can occur rapidly compared to low temperature; (2) The deformation stresses are relatively high so that fine spheroidized cementite ( $Fe_3C$ ) microstructures result [previous work has shown that fine spheroidized structures are produced at high stresses<sup>(2,3)</sup>]; (3) The ductility is sufficiently great at warm temperatures so that the fairly large strains necessary to produce homogenous microstructures are possible before fracture<sup>(4)</sup>; and (4) There is usually no recrystallization due to a phase transformation on cooling from the warm working temperature to ambient temperature.

### C. Elevated Temperature Deformation

A typical stress-strain curve obtained during the deformation of the 1.3%C steel at a constant temperature of 650°C and a constant rate of elongation of about  $1.7 \times 10^{-4}$ /s is shown in Figure 1. These high carbon steels typically strain harden to large strains followed by strain softening during superplastic deformation. Strain softening is primarily attributable to the decreasing strain rate in a constant cross-head speed test. All three high carbon steels when properly spheroidized appear to exhibit "true superplasticity" ( $m > .4$ , elongations  $> 300\%$ ). The best results to date have been elongations of 488% for the 1.3%C, 485% for the 1.6%C and 380% for the 1.9%C. Samples deformed to these elongations are shown in Figure 2.

True superplastic deformation in fine structures is observed when the strain rate sensitivity exponent  $m$  (in  $\sigma = K\dot{\epsilon}^m$ ) is about equal to 0.5<sup>(5-9)</sup>. In order to determine if our high carbon steels are truly superplastic we have evaluated the strain rate sensitivity exponent by means of stress relaxation tests. Such tests are especially useful because they represent the strain rate sensitivity at essentially constant structure. In typical tests we deformed our high carbon steels in tension at 650°C at an initial strain rate of  $1.7 \times 10^{-4}$  secs<sup>-1</sup>. The samples were deformed to a total engineering strain of 100% and then the stress was allowed to relax under constant strain.

Analysis of stress relaxation tests can be done by either of two methods, both being basically equivalent. One method is that of Lee and Hart<sup>(10)</sup>, wherein the strain rate  $\dot{\epsilon}$  is given by

$$\dot{\epsilon} = - \frac{1}{K(L_0 + X)} \left( \frac{dP}{dt} \right) \quad (1)$$

in which  $L_0$  is the initial specimen length,  $X$  is the deformation experienced by the sample,  $\frac{dP}{dt}$  is the unloading rate, and  $K$  is the test machine stiffness,

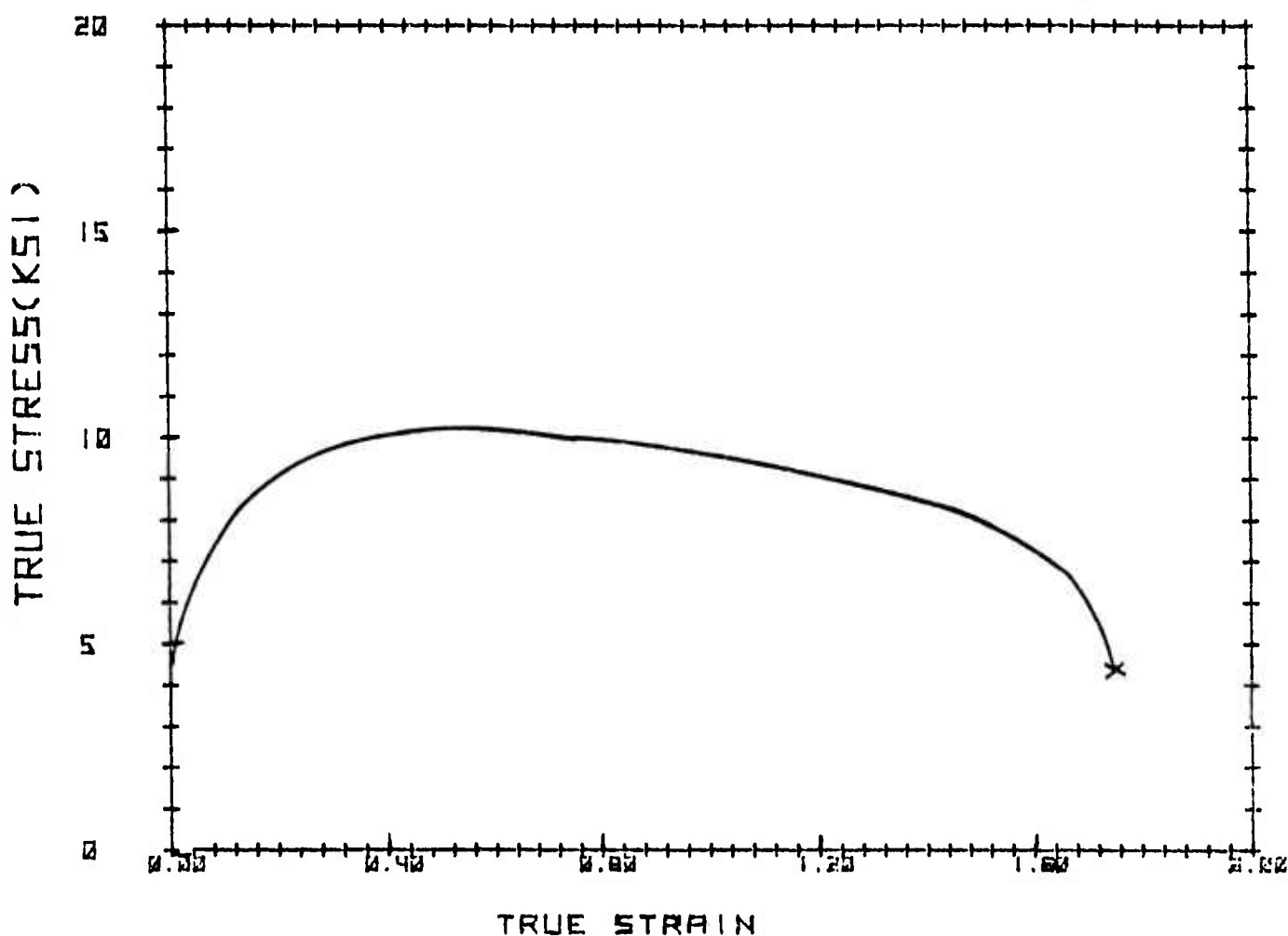


Figure 1. Typical elevated temperature stress-strain curve for Fe-1.3%C spheroidized steel deformed at 650°C and at a strain rate of  $1.7 \times 10^{-4}$ /s. The engineering elongation was over 480% or a true strain of more than 1.7. These finely spheroidized steels typically strain harden to large values of strain followed by strain softening. The strain hardening reflects some type of microstructural change with strain eventually leading to a superplastic like structure. The strain softening is primarily attributed to the decreasing true strain rate during the constant elongation rate test.

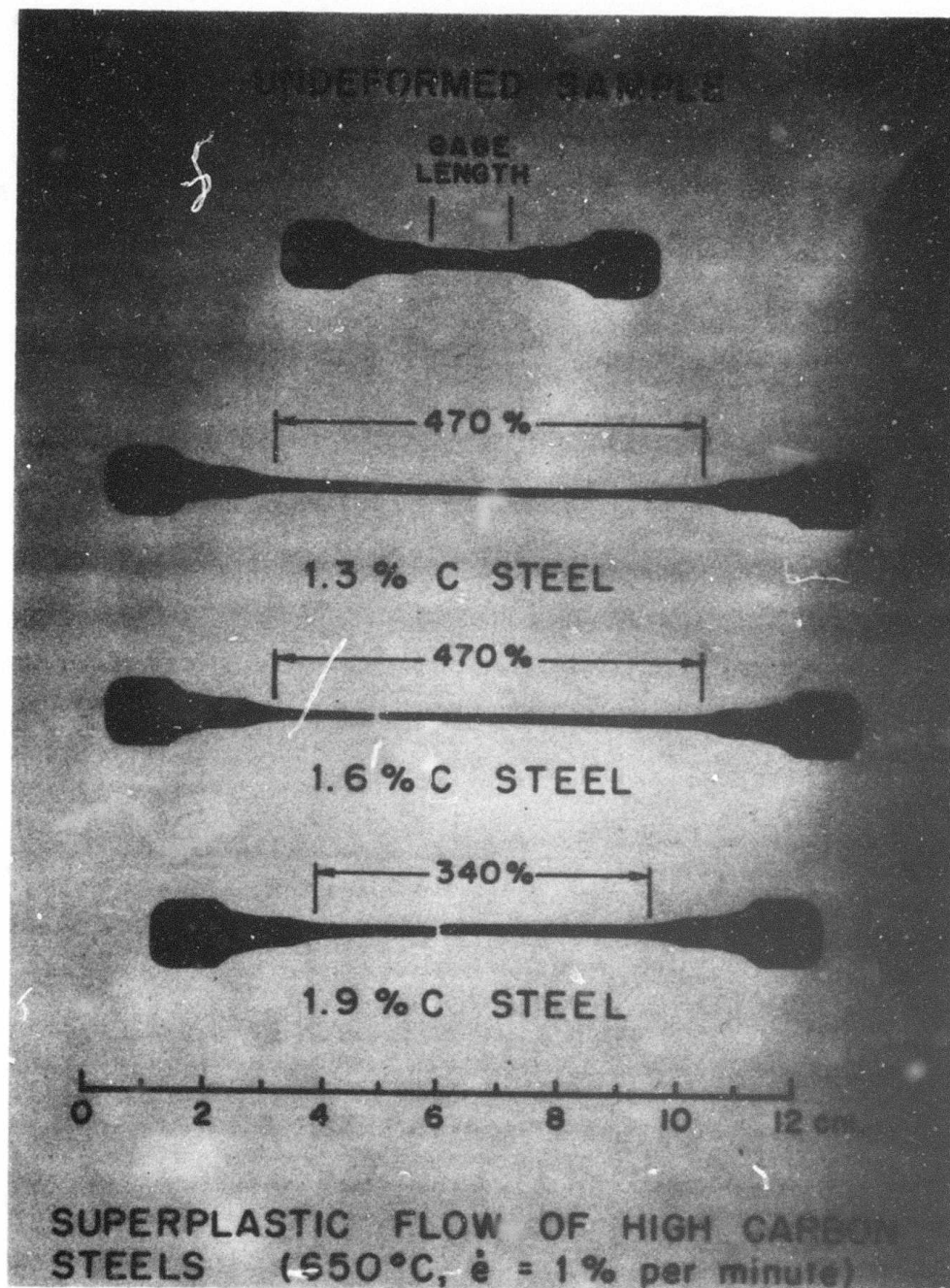


Figure 2. Typical fracture strains observed in ultra high carbon steel when in fine spheroidized condition.



given as  $\frac{1}{K} = \frac{1}{E} + \frac{1}{S}$  (where S is the stiffness of the testing machine itself and E is the dynamic elastic modulus of the test specimen). The stress at any given instant during stress relaxation is given by P/A where A is the area of the sample at the beginning of the relaxation test.

An alternate method, which will be used here, is to assume that the creep rate is proportional to a power of the stress, namely  $\dot{\epsilon} = K\sigma^N$ . During stress relaxation the following relation is maintained,

$$\dot{\epsilon}_e + \dot{\epsilon}_p = 0 \quad (2)$$

where  $\dot{\epsilon}_e$  is the elastic strain rate (equal to  $\frac{1}{E} \frac{d\sigma}{dt}$ ) and  $\dot{\epsilon}_p$  is the plastic strain rate (equal to  $K\sigma^N$ ). Thus,

$$-\frac{d\sigma}{dt} = KE\sigma^N \quad (3)$$

Dividing both sides by  $\sigma_o^N$ , where  $\sigma_o$  is the stress at the start of stress relaxation, and then taking reciprocals one obtains

$$-\frac{1}{\frac{d\sigma/\sigma_o}{dt}} = K' \left(\frac{\sigma_o}{\sigma}\right)^N \quad (4)$$

where  $K' = 1/KE \sigma_o^{(N-1)}$ . One can now take logarithms of both sides, obtaining the expression

$$\log - \left(\frac{d\sigma/\sigma_o}{dt}\right)^{-1} = \log K' + N \log \frac{\sigma_o}{\sigma} \quad (5)$$

Thus, a plot of  $\log - \left(\frac{d\sigma/\sigma_o}{dt}\right)^{-1}$  versus  $\log \frac{\sigma_o}{\sigma}$  should yield a straight line with the slope equal to N. We illustrate typical stress relaxation curves for a 1.3% carbon steel and a 1.6% carbon steel in Figure 3. We note the rapid rate of stress recovery with the stress decreasing to a quarter of its original value in less than 5 minutes. The specific values of N are calculated from the plots shown in Figure 4 where both N and its reciprocal "m" (the strain rate sensitivity exponent) are given for each of the three high carbon steels. As can be seen, rather good straight lines can be drawn through the

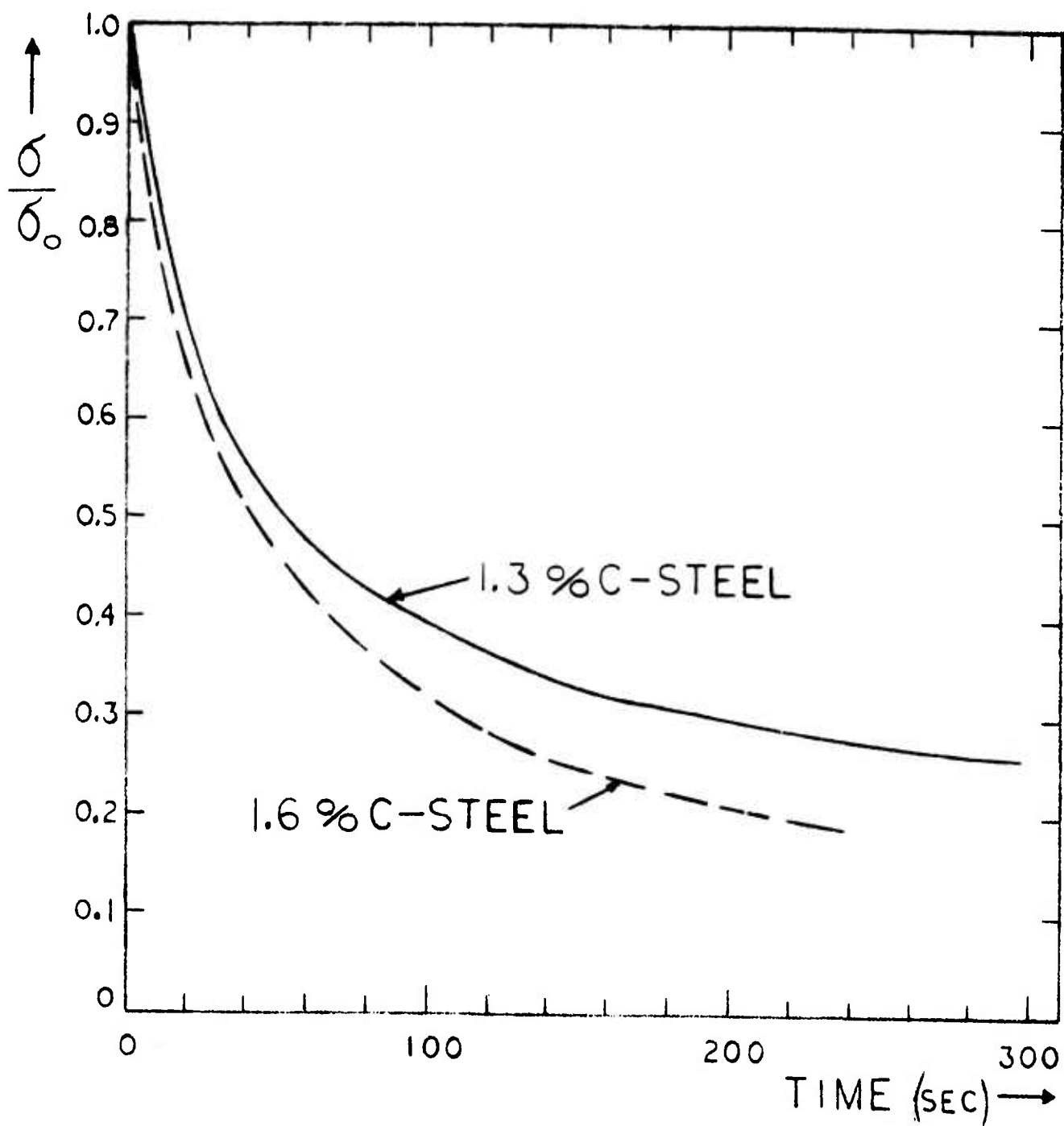


Figure 3. Stress relaxation curve for 1.3%C steel and for 1.6%C steel at 650°C after superplastic deformation to 100% engineering strain at  $\dot{\epsilon} = 1.7 \times 10^{-4}$  seconds<sup>-1</sup>.

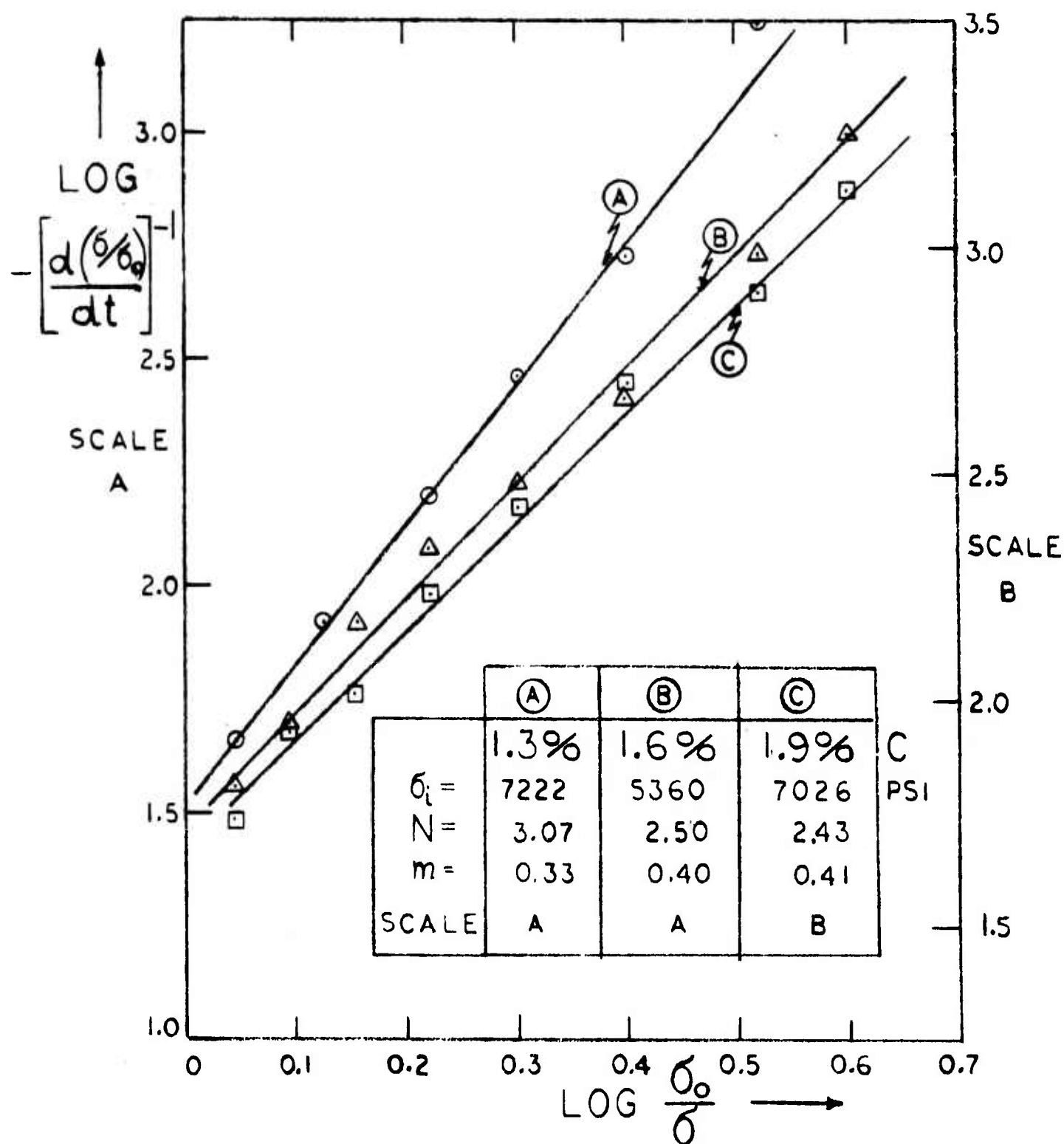


Figure 4. Stress relaxation data plotted as  $\log \left[ -\frac{d(\sigma/\sigma_0)}{dt} \right]^{-1}$  versus  $\log \sigma_0/\sigma$  for three different high carbon steels indicating the high strain rate sensitivity observed in these materials.

data (Figure 4) and  $m$  is shown to increase with increasing carbon content. Specifically,  $m = 0.33$  for the 1.3%C steel,  $m = 0.4$  for the 1.6%C steel and  $m = 0.41$  for the 1.9%C steel. Such high values of  $m$  are definite indications of superplastic type behavior. Further studies will center on determining the influence of strain rate and temperature on " $m$ " in order to optimize the range of superplastic behavior and determine the range of deformation variables over which superplasticity can be expected. Stress relaxation tests are also planned to measure  $m$  at various stages of straining (Figure 1) to gain insight into the superplastic deformation mechanism and its dependence on strain.

The increase in strain rate sensitivity of our high carbon steels with increase in carbon content is probably directly attributable to the decreasing grain size present with increasing amount of cementite. Indirect evidence for this suggestion is given in Figure 5 where stress-strain curves for the 1.9% carbon steel are shown at 650°C after various amounts of annealing, at 650°C, before testing. The initial strength of the material annealed for 15 hours prior to testing was double the initial strength of the material annealed for only two hours. This increase in strength is probably attributable to an increase in grain size during annealing for it is now well documented that the strength of superplastic materials at elevated temperature increases with an increase in grain size. Specifically<sup>(5-9)</sup>, it appears that  $\dot{\epsilon} \propto \frac{\sigma^N}{L^p}$  where  $N$  is typically 2.0 and  $p$  is about 3.0. Or, at a given strain rate, the flow stress can be written as a function of grain size as follows  $\sigma \propto L^{p/N}$  or  $\sigma \propto L^{2/3}$ . Thus, for a two-fold increase in strength (Figure 5) one would expect the grain size to increase by  $2^{3/2} = 2.8$ . This amount of grain growth in 15 hours is certainly reasonable and in line with our current observations (see, for example, Figures 8B and Figure 10).

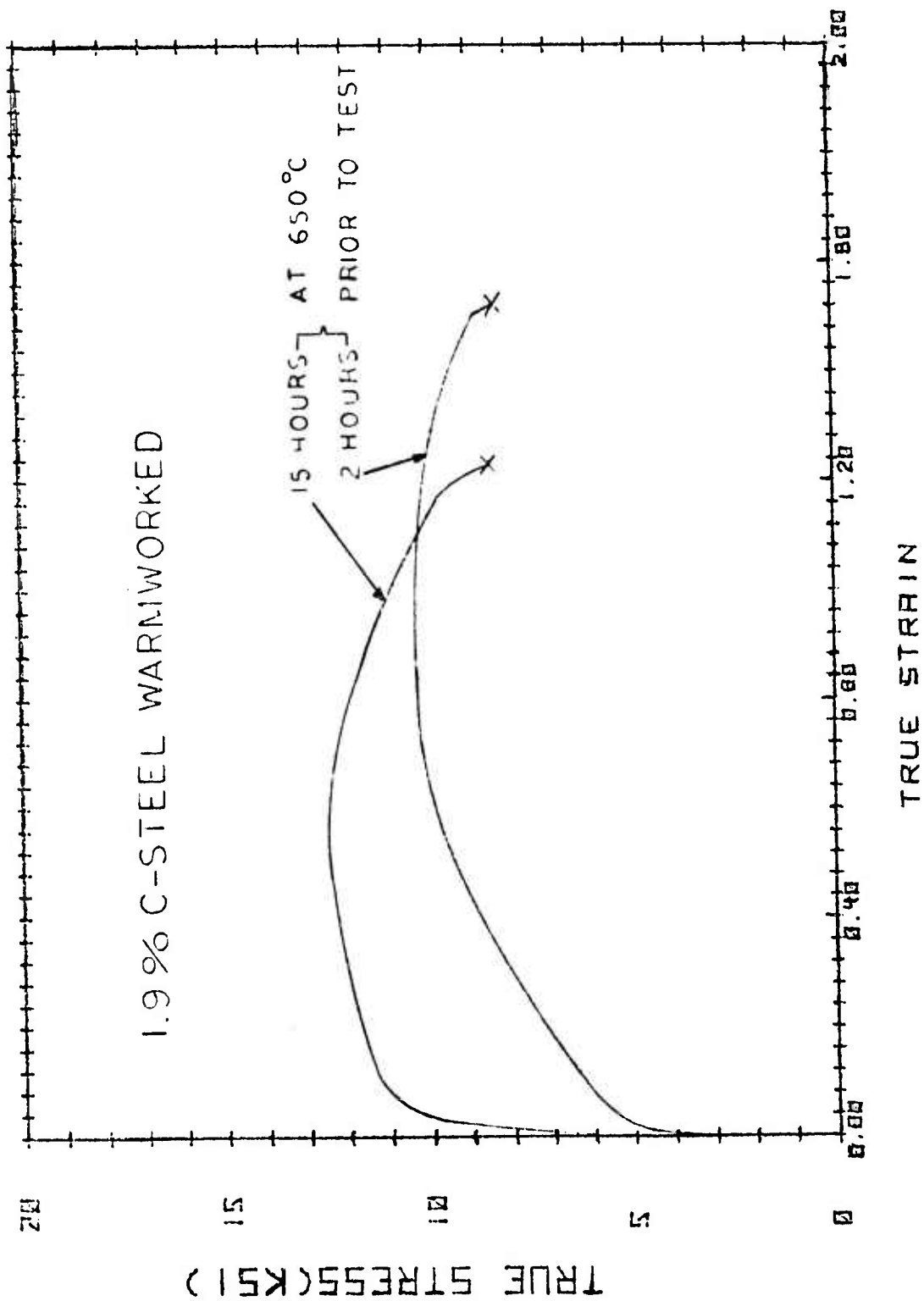


Figure 5. Influence of annealing time at 650°C on the true stress-true strain curve of a spheroidized 1.9%C steel (deformed at  $\dot{\epsilon} = 1.7 \times 10^{-4}$  seconds<sup>-1</sup>).



In Figure 6 we illustrate the influence of cementite content on the flow stress of iron at 650°C and at  $\dot{\epsilon} = 1.7 \times 10^{-4} \text{ sec}^{-1}$ . In the case of the high carbon steels the flow stresses reported were those obtained after 100% elongation. It is noteworthy that the flow stress first increases with carbon addition but then decreases with increased carbon additions. These results are consistent with our earlier interpretation that fine grain size leads to weakening in the superplastic range of temperatures and increasing the volume fraction of cementite leads to decreasing stable grain sizes (after warm working). It is rather remarkable to note that the ultra high carbon steels are as weak as pure iron under the stated conditions of testing.

#### D. Electron Transmission Studies of the 1.9% Carbon Steel

The fine scale of the spheroidized structures requires that electron microscopy be employed to correctly resolve the microstructure. Transmission electron microscopy of thin foils has been selected because of its ability to resolve individual dislocations, dislocation arrays and subgrains, grain boundaries, small particles, as well as second phase distributions and orientations. To prepare foils for transmission electron microscopy a longitudinal section was cut from the as-rolled plates or from the gage length of tested samples with an electrical discharge machine. This section was ground on #600 SiC-paper to a thickness of about 0.003". These thin plates were thinned at room temperature in a twin jet electropolishing unit using a window technique. The electrolyte was 150 grams  $\text{NaCrO}_4$  (anhydrous) in 750 ml acetic acid, at a voltage potential of 19-22 volts (closed circuit) using a moderate jet speed. After the first hole was perforated the sample was thoroughly washed in methanol and the edges were re-lacquered. This process was repeated several times until enough holes and bridges were produced. A small piece was then cut out for investigation. The foils were examined at 100 kV in a Philips 200 electron

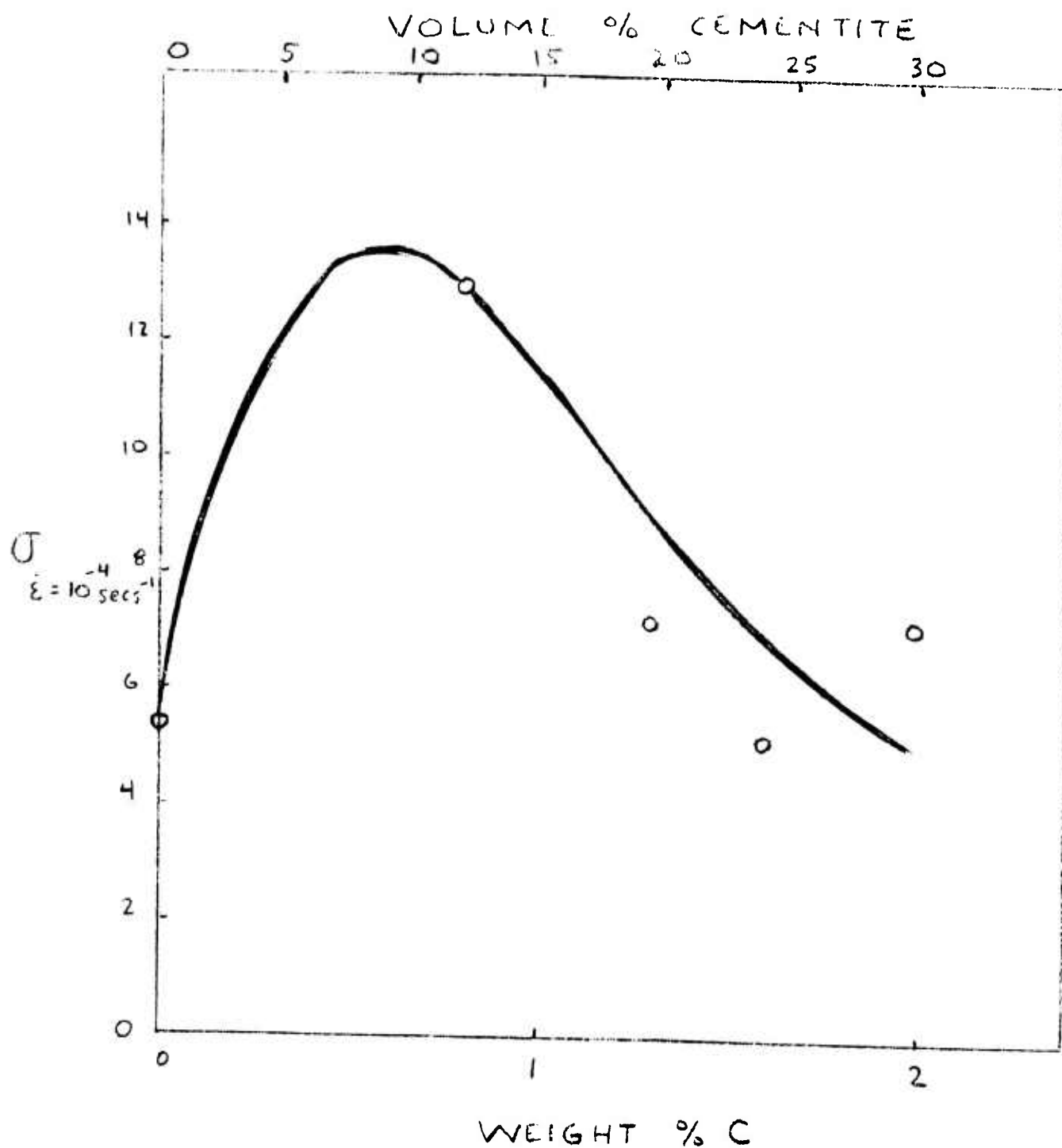


Figure 6. Influence of carbon content (distributed as fine spheroidized particles of cementite) on the flow stress of iron at 650°C and at  $\dot{\epsilon} = 1.7 \times 10^{-4} \text{ seconds}^{-1}$  (data taken from references 11, 12 and this investigation).

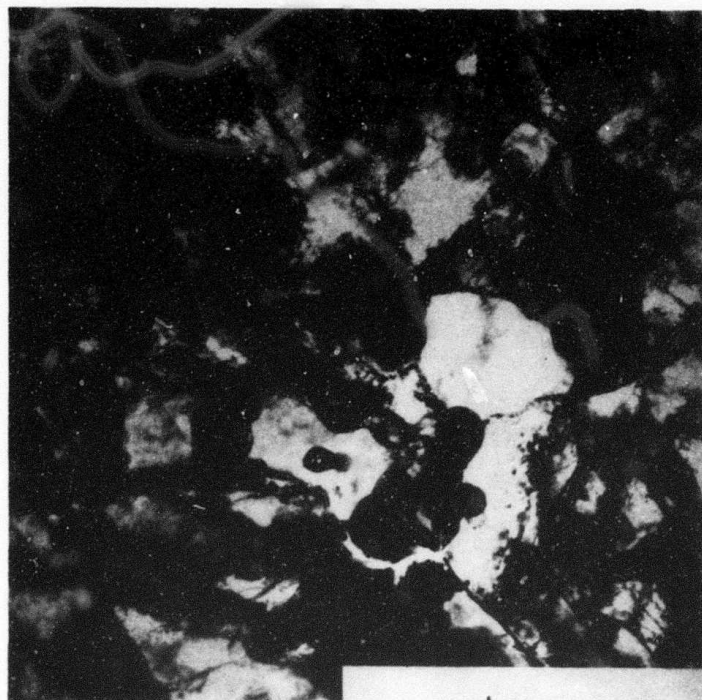
microscope. The TEM investigation was done on several samples of the 1.9%C steel: (a) as warm worked, (b) after superplastic deformation at 650°C and (c) after annealing at 650°C for 15 hours.

(a) As Warm Worked

The structure of the warm rolled plate is shown in Figure 7A (top). About three-quarters of the investigated material looks like this example: containing equiaxed grains and spheroidized carbides. There is a high dislocation density within the grains. To find out if the microstructure consists of subgrains or grains some diffraction and dark field studies were done. This study established that the material contains very fine grains, about 0.8 $\mu$ m average diameter (measured by intercept technique). Some evidence of subgrain formation was found but the working process produces a microstructure comprised primarily of very fine high angle grains. The carbides are very well distributed and most of them reside in grain boundaries. The warm working process leads to the desired spheroidization. The size of the carbides lies between 0.1 and 0.4 $\mu$ m. Some portions of the as-rolled material (about one-quarter) consisted of a pearlitic structure (Figure 7B). This may be caused by inadequate warm working strain to spheroidize all of the large amount of carbide contained in the 1.9%C steel.

The following conclusion can be made based on these micrographs. The material recrystallizes during warm working producing the very fine grain structure. The large volume fraction of carbide particles prevents grain growth during the thermal-mechanical processing operation. A subgrain structure is observed but because of the fine grains and the high dislocation density it is difficult to distinguish between subgrain and grain boundaries in normal bright field microscopy.

A

1  $\mu$ m

B

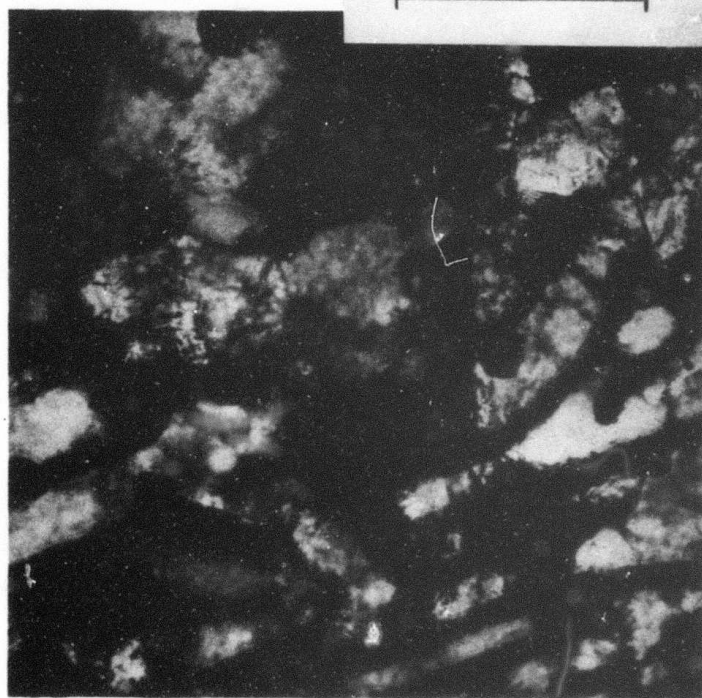


Figure 7. Transmission electron micrographs of 1.9%C steel as warm worked. Top, well spheroidized Fe<sub>3</sub>C between sub-micron grain of  $\alpha$ -Fe; bottom, incompletely spheroidized pearlite region due to limited warm working.

(b) As Superplastically Deformed 1.9%C Steel

We investigated two samples by transmission electron microscopy: one sample was deformed 100% at 650°C and the other was deformed 200% at 650°C. In general we could find two typical regions with respect to their microstructural appearance; one region exhibited a homogeneous distribution of carbides in a ferrite matrix and the other exhibited mainly ferrite with very few carbides. From the electrolytic polishing it is to be expected that the carbide-free areas are preferentially attacked and therefore thin enough for transmission electron microscopy. Most of the areas observed are like the example in Figure 8A (top). The ferrite grains are very clear of dislocations or subgrain boundaries. The high angle grain size is about 1 $\mu$ m even in these areas with very low carbide content. The carbides are mostly within grain boundaries and show a typical equilibrium appearance. In the case of carbides within grains, they show a perfectly spherical form. We can conclude that during superplastic formation an equilibrium structure is achieved, which does not change once it is formed. Figure 8B shows regions comprising the majority of the material which is more difficult to thin because of the large amount of carbide phase. This microstructure is typical for a superplastic material, i.e., fine equiaxed grains for both phases, large amount of second phase, no (free) dislocations within grains and no subgrain boundaries. The ferrite grain size is about 1 to 2 $\mu$ m and the carbide size ~0.5 - 1 $\mu$ m. The photomicrographs suggest that the carbides form a continuous network. This would be a bad feature for room temperature strength because of the brittleness of the continuous cementite at room temperature. Figure 9 illustrates some of the very seldomly observed dislocations and sub-boundaries within the superplastically deformed materials. Obviously the round carbides within grains act as pinning sites. But, in



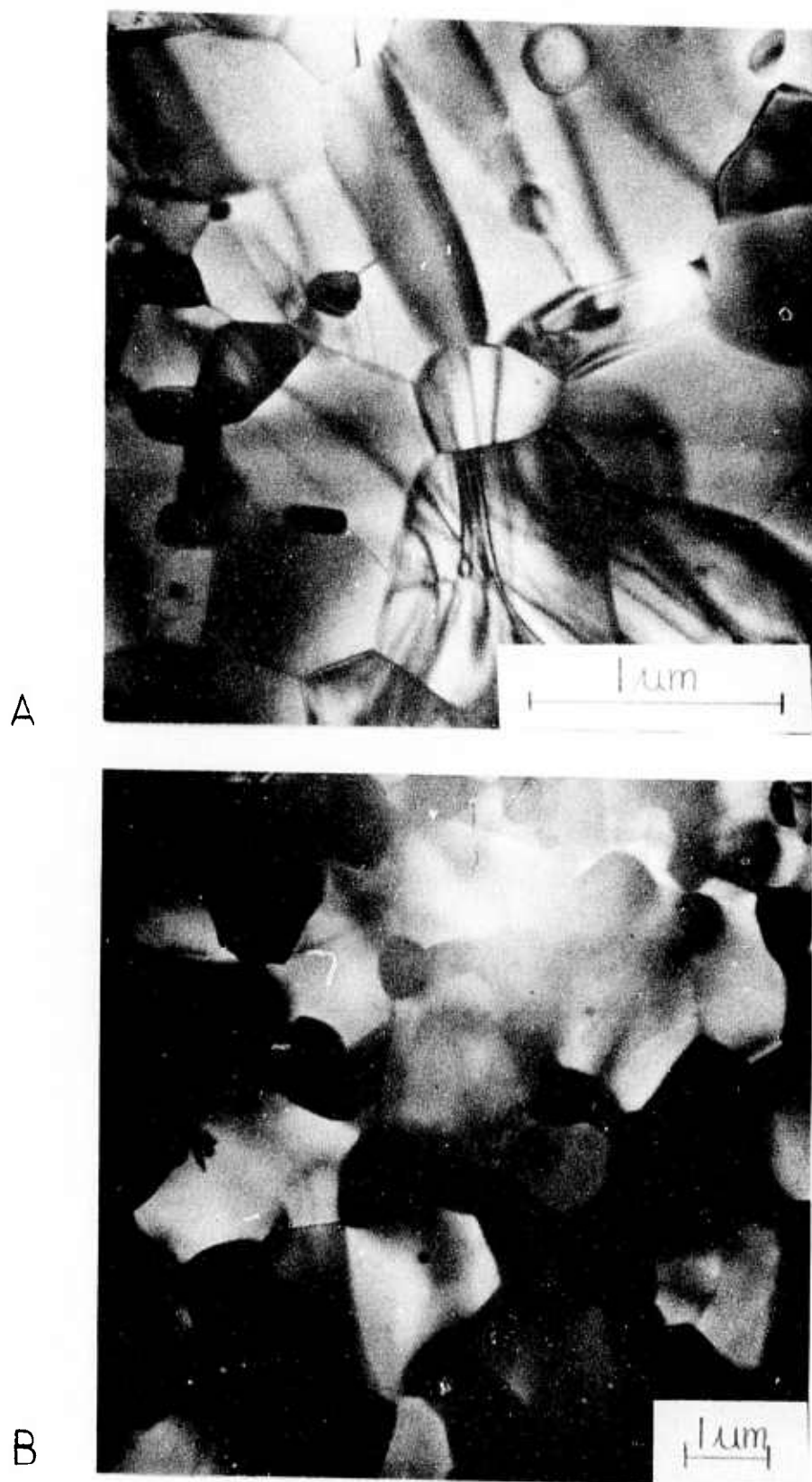


Figure 8. Spheroidized 1.9%C steel after 100% elongation at 650°C. Top, a region containing few carbides; bottom, a region containing a "normal" amount of  $\text{Fe}_3\text{C}$  second phase in the  $\alpha\text{-Fe}$  grain.

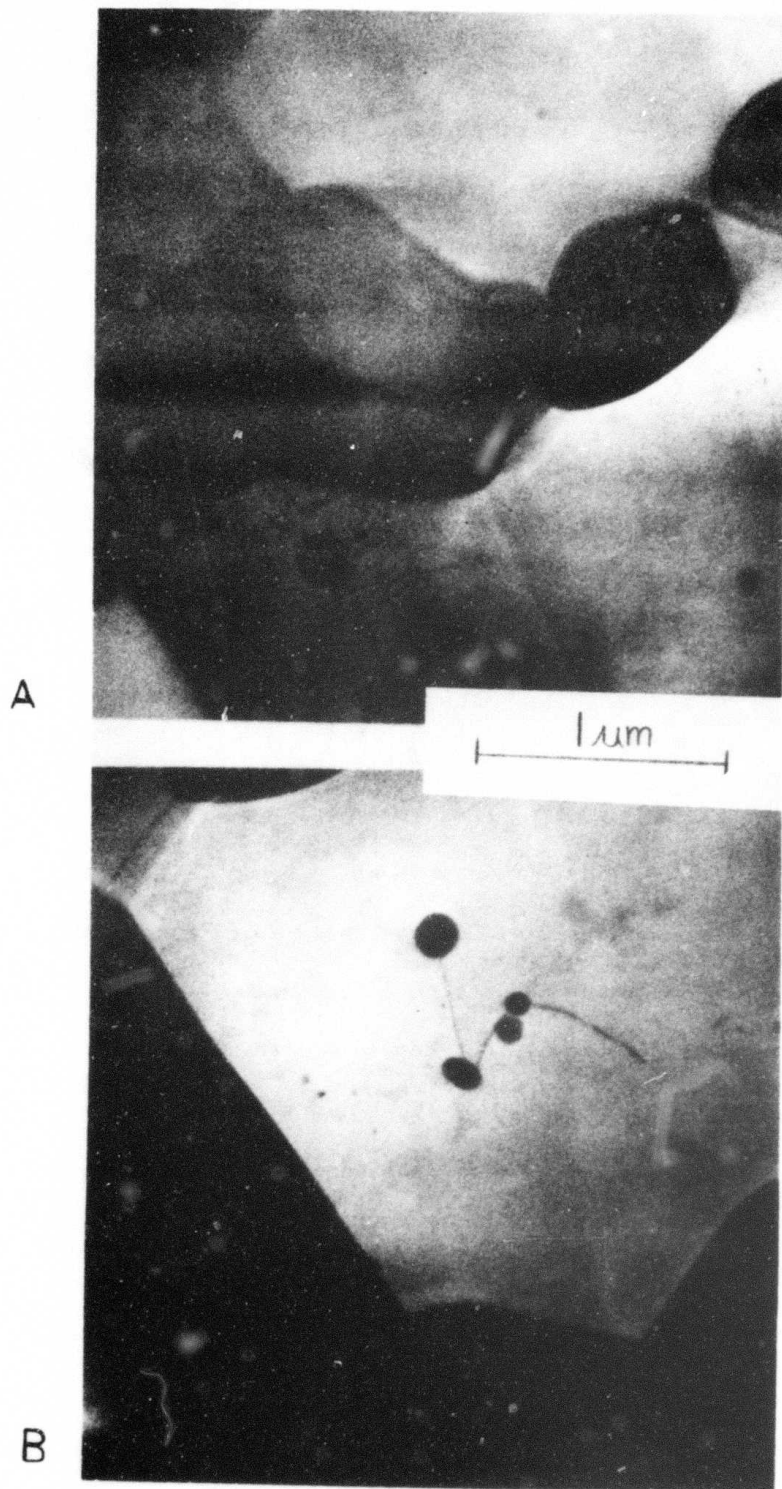


Figure 9. Transmission electron micrographs of spheroidized 1.9% C steel after 100% elongation at 650°C,  $1.7 \times 10^{-4}$ /s. Top, one of the few dislocation arrays observed in this material; bottom, a dislocation pinned by small Fe<sub>3</sub>C particles.

general, there are very few of these pinned dislocation structures.

There was an indication that some regions of the microstructure contained a high dislocation density and were not deforming superplastically. This may have been due to a non-homogeneous distribution of the spheroidized carbides. Figure 10 shows a sample of spheroidized 1.9% C steel deformed 200% at 650°C with a micro-structure similar to the previous one (Figure 8). The grain size has increased to about 1.5 - 2  $\mu\text{m}$  indicating that grain growth is occurring during superplastic deformation. The carbides have also grown to about 1 - 1.5  $\mu\text{m}$  and they appear to have formed a nearly continuous network in the  $\alpha$ -Fe grain boundaries.

(c) As Annealed at 650°C for 15 hours

To investigate the influence of the testing temperature of 650°C on the microstructure we looked at a thin foil prepared from the grip of the sample described in section (b) (Figure 10) and shown in Figure 11. It is evident that most of the microstructure is partially recrystallized and that we get very fine equiaxed grains and a good distribution of carbides (grain size 0.8  $\mu\text{m}$ ). Recrystallization is not complete after 15 hours at 650°C and there are still some regions with the warm rolled structure (Figure 11B). The micrograph shows the structure-free characteristics of these ferrite grains, i.e., there are no dislocations in the recrystallized areas. The carbide distribution shown in the grip region indicates that the network structure of carbides observed in the superplastically deformed material forms during the deformation process. We never saw continuous carbide strings outlining the ferrite grain boundaries in the grip region.

E. Ambient Temperature Properties

To complement the excellent superplastic formability of these high carbon spheroidized steels it is desirable to have good ambient temperature proper-

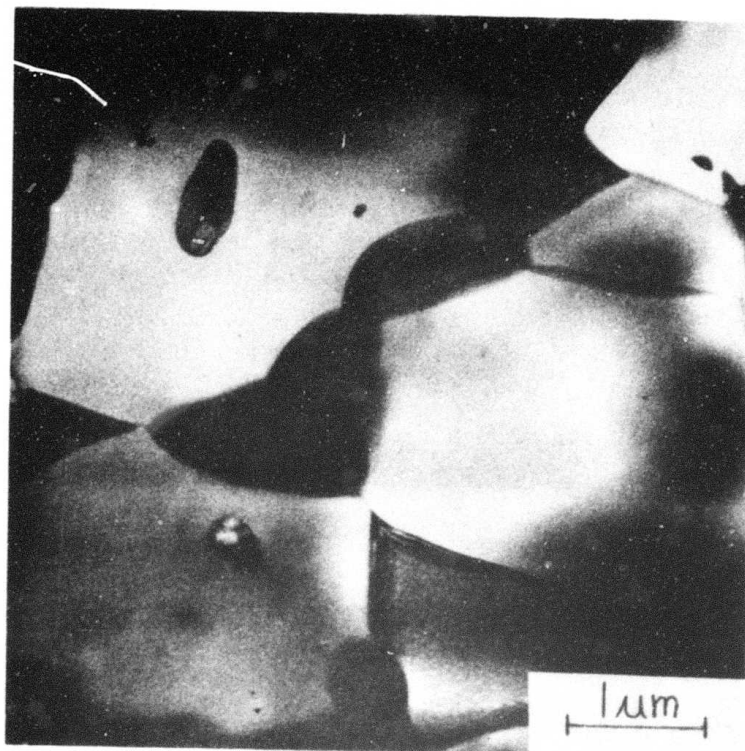


Figure 10. Transmission electron micrograph of spheroidized 1.9%C steel after 200% elongation at 650°C,  $1.7 \times 10^{-4}$ /s. The grain size has grown to about  $2\mu\text{m}$  and the carbides are forming a continuous network in the  $\alpha$ -Fe grain boundaries.



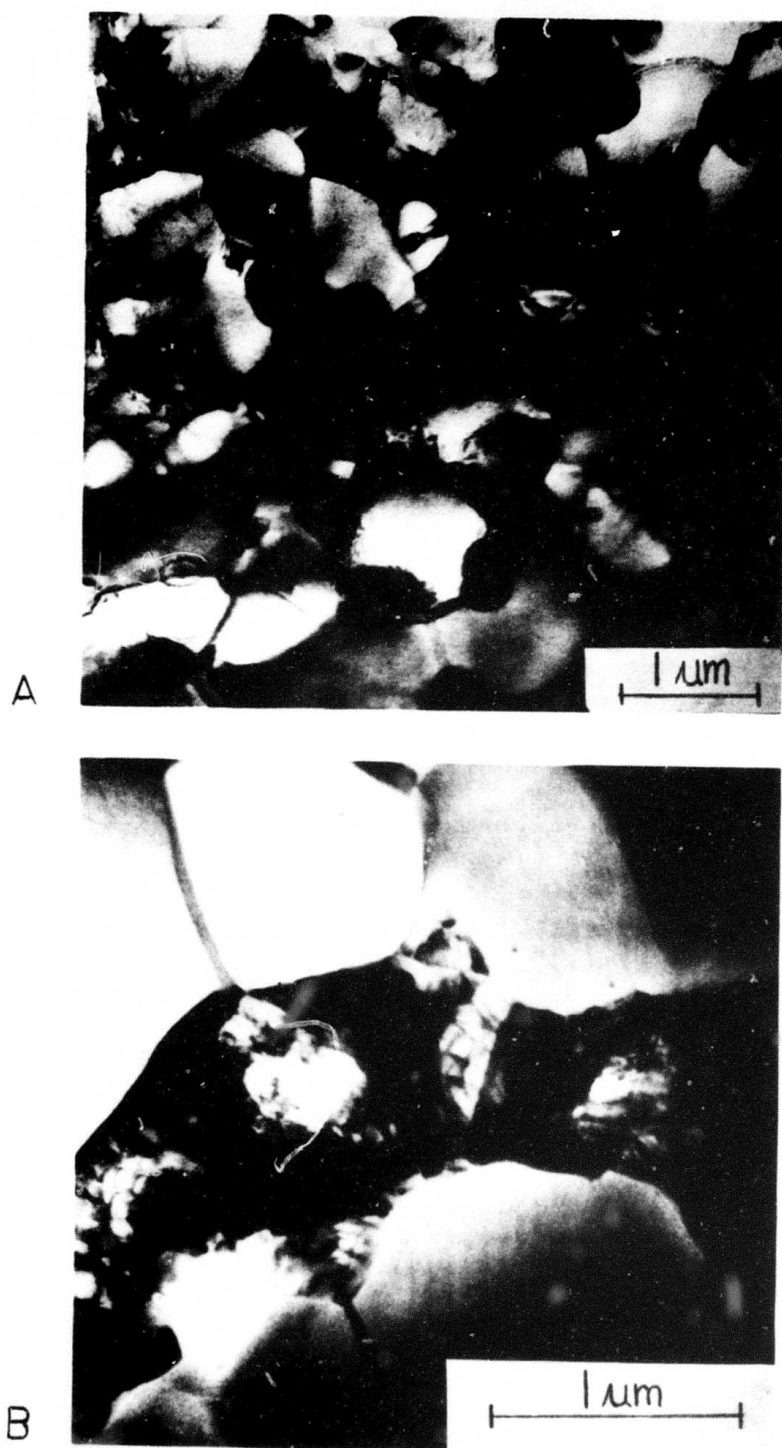


Figure 11. Transmission electron micrograph of spheroidized 1.9%C steel after annealing for 15 hours at 650°C. Top, fairly uniform recrystallized area; bottom, recrystallized areas growing into the remaining warm worked region.

ties. Figure 12 shows the room temperature strength and ductility of spheroidized 1.3%C steel after various heat treatments. Curve (A) is for this material after warm worked such that the finishing temperature was about 560°C. This curve represents a very attractive combination of strength (178 ksi yield) and ductility (4.8%). Warm working this material at a higher temperature, 650°C, lowers both the yield strength (160 ksi) and the ductility (1.3%) as shown by curve (B). This unexpected result may be due to particle coarsening and or to the formation of a continuous cementite network at this high temperature of warm working. Heating the warm rolled product to a temperature low in the austenite plus cementite phase region (760°C) for 10 minutes followed by a slow cool resulted in a further decrease in the yield strength to 119 ksi but an increase in the ductility to 6% as shown by curve (C). Similar treatments on the 1.6 and 1.9%C steels have produced disappointing results in terms of both strength and ductility. Annealing of these two alloys (500°C, 100 Hr) resulted in a product with lower strength and ductility than the as-rolled material. It is clear that further research is required to obtain an attractive combination of ambient temperature properties in these two high carbon steels.

The room temperature tensile stress-strain curves for these spheroidized high carbon steels following superplastic deformation (100% elongation at 650°C,  $1.7 \times 10^{-4}$ /s) are shown in Figure 13. These tests were performed to measure the room temperature properties of these alloys after a simulated superplastic forming operation at elevated temperature. The appearance of a seemingly continuous cementite network during superplastic deformation in these alloys (Figures 8 and 10) has apparently not completely embrittled these materials. Curve (A) is for the 1.9%C steel which reveals a yield strength about 125 ksi with about 2% elongation. Curves (B) and (C) are nearly



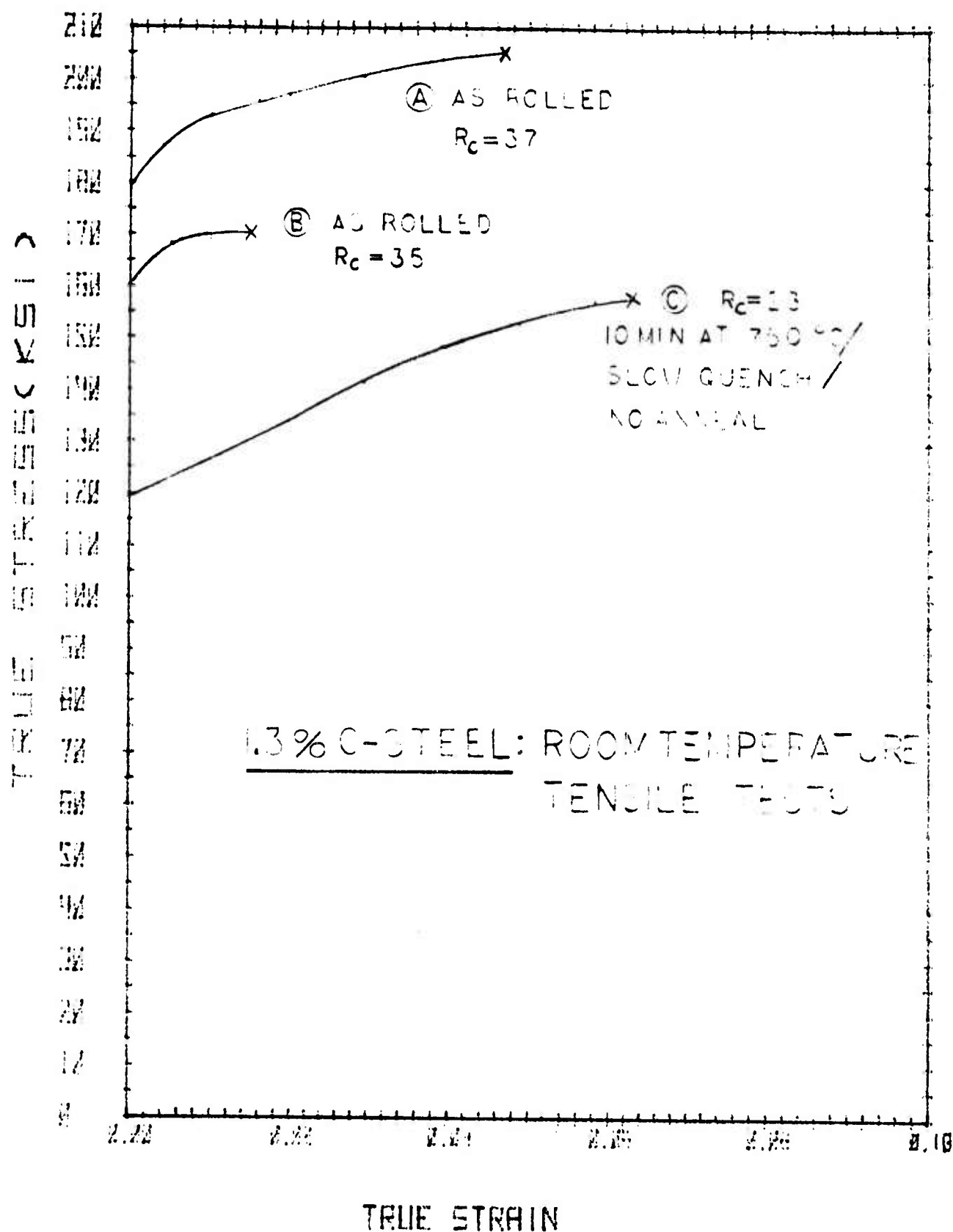


Figure 12. Room temperature tensile stress-strain curves for the spheroidized 1.3%C steel after various heat treatments. Curve (A) warm worked at a finishing temperature of 560°C; curve (B) warm rolled at a finishing temperature of 650°C, curve (C) warm worked followed by heating to 760°C for 10 min, then air cooled.

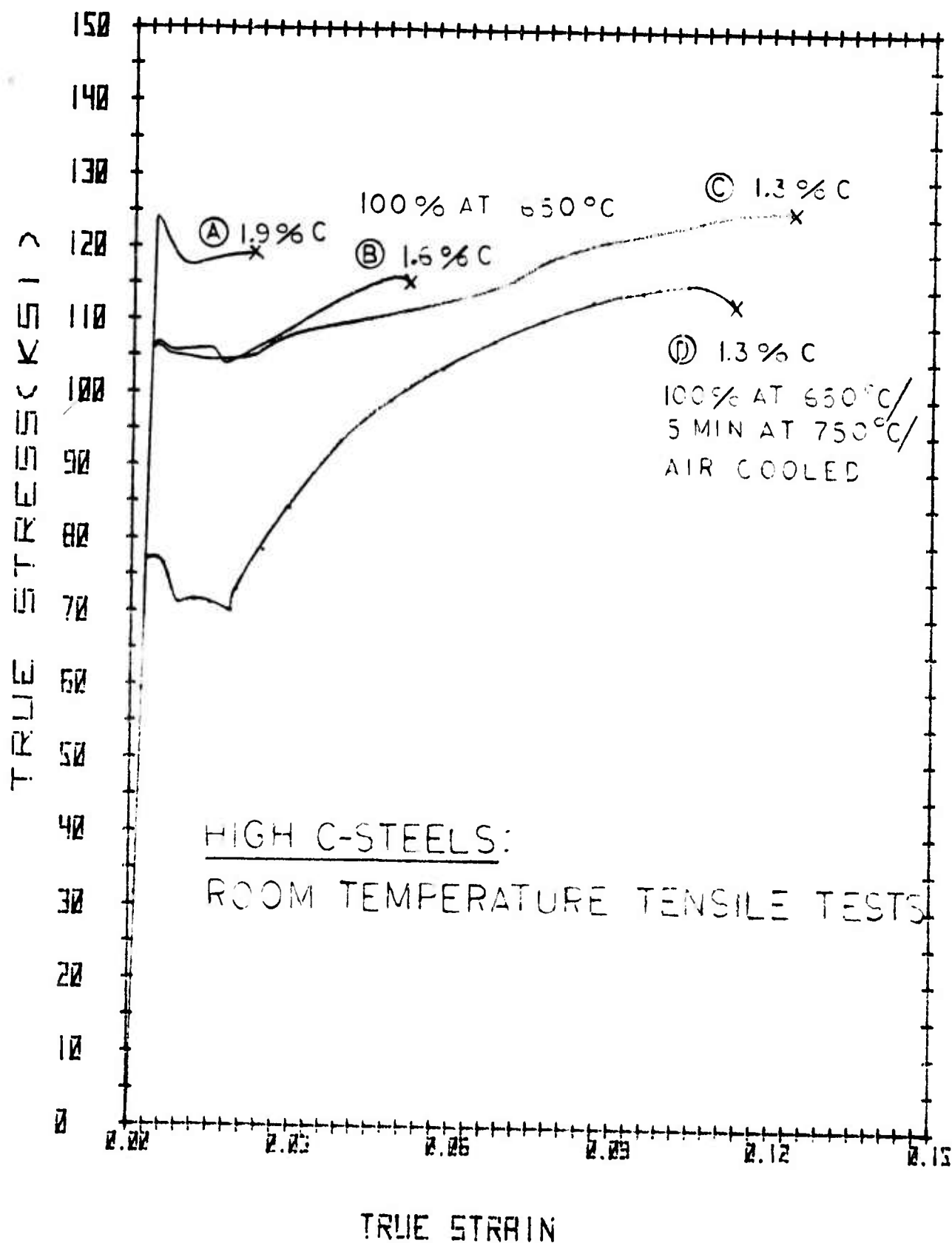


Figure 13. Room temperature tensile stress-strain curves of spheroidized high carbon steels following superplastic deformation (100% elongation at 650°C,  $1.7 \times 10^{-4}$ /s). Curve (A) is for 1.9%C; curve (B) is for 1.6%C; curve (C) is for 1.3%C; curve (D) is for 1.3%C which was heated to 750°C for 5 min and then air cooled after superplastic deformation (100% elongation at 650°C).

identical for the 1.6 and 1.3%C steels, respectively, with yield strengths of about 106 ksi and about 12% elongation which makes these respectable engineering structural materials. Curve (D) is for a sample of 1.3%C steel which was given a special heat treatment after superplastic forming. This sample was heated to 750°C for 5 min then air cooled resulting in a 76 ksi yield strength and about 11% tensile strain. A large yield point phenomenon was observed in this material.

From the results depicted by Figures 12 and 13 it is clear that even at present these high carbon steels have good engineering structural properties. It is also evident that the mechanical properties can be radically altered by various heat-treatments on the as-worked or superplastically formed product. With further research it is felt that a thermal-mechanical processing schedule can be found which will result in the best combination of strength and ductility for each alloy.

## F. REFERENCES

1. P. E. Armstrong, W. V. Green, E. G. Zukas and O. D. Sherby, *Acta Met.*, 21, (1973) 1319-1326.
2. M. J. Harrigan, L. Chamagne, C. Sauve and O. D. Sherby, *Transactions Quarterly, ASM*, 62, (1969) 575.
3. M. J. Harrigan and O. D. Sherby, *Materials Science and Engineering*, 7, (1971) 177.
4. C. M. Young and O. D. Sherby, *Jnl. Iron and Steel Institute*, 211 (1973) 640-647.
5. H. W. Hayden, R. C. Gibson, H. F. Merrick and J. H. Brophy, *Transactions, ASM*, 60, (1967) 3.
6. C. M. Packer and O. D. Sherby, *Trans., ASM*, 60, (1967) 21-28.
7. A. Ball and M. M. Hutchison, *Metal Sci. Journal*, 3, (1969) 1.
8. J. E. Bird, A. K. Mukherjee and J. E. Dorn, Quantitative Relation Between Properties and Microstructure, (1969) Israel Universities Press, 255.
9. C. M. Young, R. A. White and O. D. Sherby, *Scripta Metallurgica*, in press.
10. D. Lee and E. Hart, *Metallurgical Transactions*, 2, (1971) 1245.
11. T. Watanabe and S. Karashima, *Metallurgical Transactions*, 2, (1971) 1359.
12. First Semi-Annual Technical Report, July 1 - Dec. 31, 1974, DAHC 15 73 G15, Center for Materials Research, Stanford University, Stanford, California.

## 2. Breakdown of Lamellar Microstructures During Warm Working

J. C. Shyne and M. Shimizu

One of the most important aspects of the influence of warm working on plain carbon steels is the breakdown of lamellar pearlite to spheroidite. Neither the mechanism for this process nor its kinetics are understood. Therefore one aim of our research is to elucidate the breakdown process of such lamellar microstructures.

Lamellar microstructures are a common feature of many alloys. Steel provides the most common technological example, the eutectoid pearlite consisting of alternating layers of  $\alpha$  - Fe and  $\text{Fe}_3\text{C}$ . Such lamellar microstructures are unstable and tend to change to mixed equiaxed grains or particles of the two phases. In particular, the breakdown of lamellar pearlite to equiaxed spheroidite occurs in steel as a consequence of heat treatment and metal working processes. Pearlitic iron-carbon alloys, however, are experimentally difficult materials because of the brittleness of  $\text{Fe}_3\text{C}$  under most conditions. Lead-tin forms a lamellar eutectic microstructure when solidified slowly. This material, 40 wt. pct. Pb - 60 wt. pct. Sn, is interesting for its own sake and serves as an experimentally convenient model for the more intractable pearlite.

The aim of the research is to obtain meaningful kinetic data for the breakdown of the lamellar Pb-Sn eutectic after cold deformation. The pertinent data are the geometric details of the microstructure changes, the degree of cold work, time and temperature. Cold work is accomplished on the cast microstructures by rolling. Rolling must be performed below room temperature to avoid microstructural breakdown from occurring concurrently with the rolling process. The sublimation temperatures of dry ice,  $-77^\circ\text{C}$ , has proved to be experimentally convenient for rolling.

Subsequent to rolling, specimens are held for various times at various temperatures and the microstructural changes observed after metallographic polishing and etching. To date satisfactory metallographic techniques have been developed using both mechanical polishing and electrolytic polishing, however, it is not clear yet that the temperatures necessary for these metallographic operations are low enough to avoid any microstructural change during the polishing process itself. Some auxiliary experiments have undertaken to utilize differential thermal analysis, DTA, to characterize the effect of temperature especially on the rate of the process of structural breakdown. Specimens cold worked various amounts at  $-77^{\circ}\text{C}$  will be heated slowly from the rolling temperature to a temperature well above room temperature e.g.,  $60^{\circ}\text{C}$ . During heating the DTA apparatus monitors the relative amount of heat released by the endothermic process of structural change. At this point, it appears that DTA may be suitable to this intended purpose; several tricky experimental problems arising from the fact that the DTA data range must extend to  $-77^{\circ}\text{C}$  have been overcome, but no useful DTA results are yet achieved.

The metallographic part of the program has not yet included quantitative kinetic data, however, some very interesting qualitative observations have been made.

1. The cold worked lamellar microstructure breaks down ("recrystallizes") into a microstructure consisting of essentially equal sized, equiaxed grains of the two phases. The grain diameter tends to be somewhat larger than the original lamellar thickness.
2. This process of structural change occurs preferentially at previous colony boundaries where discontinuities in lamellar orientation occur.
3. The process of structural change proceeds by the growth of band of



the equiaxed regions outward from the original lamellar colony boundaries, i.e., the process of structural breakdown is essentially a discontinuous process similar to the growth of recrystallized regions in normal, single phase, recrystallization.

These observations imply that the process of structural breakdown ought to be limited in its rate by the diffusion of Pb and Sn as these elements are transported from the original lamellar configuration to the new, equiaxed configuration.

**V. SUPERPLASTICITY OF Pb-Sn AND Pb-Sn-Au ALLOYS**

**C. R. Barrett**

**Associate Professor of Materials Science  
and Engineering**

**and**

**A. E. Geckinli**

**Research Associate of Materials Science  
and Engineering**

This portion of the investigation has been concerned with two aspects of superplastic flow in Pb-Sn eutectic alloys. First, the influence of a fine precipitate distribution on superplastic flow and fracture is being investigated. The second and related aspect of the study is the possibility of strengthening the normally soft superplastic alloys by a precipitation heat treatment. This would be useful for improving the strength properties of superplastic materials following forming treatments.

To date, the majority of experiments have been carried out on the Pb-Sn-Au system. The alloy composition is the Pb-Sn eutectic composition with about 0.1% Au. Samples are melted, cast, and then cold rolled to produce an equiaxed grain structure, with average grain size of  $3\mu$ . Aging the alloys in the temperature range 120 - 160°C prior to cold rolling causes  $\text{AuSn}_4$  precipitation with an average precipitate spacing of about  $0.1\mu$ . The flow properties of these alloys are being evaluated using stress relaxation techniques, tensile tests, and carrying out dynamic studies in the scanning electron microscope using a special tensile stage. The results obtained thus far are listed below.

Stress relaxation tests have been carried out at room temperature over a range of relaxation rates (strain rates) of  $10^7$ . The data for pure Pb-Sn and Pb-Sn-Au (aged for a variety of times at 120° or 160°C) show similar characteristics. Namely, at low relaxation rates (low stresses) Newtonian viscous deformation is observed (directional diffusion creep) and the flow stress is increased the dominant deformation mode is grain boundary sliding and superplastic flow is observed. At high stresses recovery-work hardening creep associated with the generation and motion of dislocations is observed. At low stresses the Pb-Sn and Pb-Sn-Au data superimpose whereas in the superplastic flow region and recovery work hardening creep region the Pb-Sn-Au samples have a flow stress about twice the Pb-Sn samples at the same strain rate. Although the flow stresses differ, the maximum strain rate sensitivity is the same for the two alloys, being about 0.33-0.4. This strengthening of the Pb-Sn-Au precipitate hardened alloys in the superplastic flow region does not result in any noticeable change in the

mechanism of plastic flow. The scanning electron microscope data suggest that the predominant deformation mode is grain boundary sliding for both alloys. The only grain deformation observed is localized to the region of the grain boundaries and is associated with the preservation of coherence between grains.

The origin of the increase in the flow strength of the Pb-Sn-Au alloys is as yet undefined. Two possibilities are (1) a slight change in diffusivity with addition of Au to the Pb-Sn alloy and (2) an influence of the  $\text{AuSn}_4$  precipitates on the accommodation deformation accompanying grain boundary sliding. The weak stress dependence of the strain rate during superplastic flow means that a small change in diffusion coefficient will be translated into a similar magnitude change in flow stress at constant strain rate. That is, if the diffusion coefficient were to change by a function of three, we could expect to see a two-fold or so change in flow stress. The second possibility listed above relates to the influence of the  $\text{AuSn}_4$  precipitates on the plastic deformation which must accompany grain boundary sliding if grains are to maintain coherency. The accommodation deformation may take place either by diffusional flow or grain boundary sliding. There is considerable data in the literature to suggest that a fine distribution of precipitates or dispersed particles may alter the local flow characteristics for either of these flow conditions. Present work is directed to examining the various possibilities listed above.

One further aspect of the study involves the influence of  $\text{AuSn}_4$  precipitates on the fracture properties of Pb-Sn-Au alloys. It is observed that the total strain to failure is lower in the precipitation hardened alloys (about two or three times less than that observed for Pb-Sn alloys tested under identical conditions). Scanning electron microscope studies to date indicate considerable porosity generation in the Pb-Sn-Au alloys during superplastic flow. This feature probably accounts for the decreased ductility. Work is underway to establish the cause of this porosity and determine what influence it may have on the formability of the Pb-Sn-Au alloys.



VI. SYNTHESIS OF NEW TYPES  
OF CATALYST MATERIALS

J. P. Collman  
Professor of Chemistry

and

M. Boudart  
Professor of Chemical Engineering  
and Chemistry

1. Synthesis and Characterization of Supported Organometallic Rhodium (I) Catalysts

D. N. Marquardt

The PhD dissertation by Donald N. Marquardt serves as the Annual Technical Report for the work on hybrid homogeneous-heterogeneous catalysts supervised by Professor Collman with consultation by Professor Boudart, and is presented separately as an appendix to this Technical Report.

The chelating silated phosphine mentioned in the last Quarterly Report has been prepared and catalysts derived from it have been studied kinetically. This work represents the best comparison to date between homogeneous and heterogeneous catalysts. During the first part of the next year, this work will be extended to chelating arsines and the kinetic results amplified. Arrangements have been made at Yale University with Professor Jack Faller for a collaborative study using X-ray photoelectron spectroscopy (ESCA). Preliminary results are very encouraging and through the use of this technique, we hope to further clarify classic heterogeneous catalysts.



## 2. Structure Insensitive and Structure Sensitive Catalytic Reactions

For catalysis by metals, a traditional distinction has been made between geometric and electronic factors. The geometric factor is related for a given metal to changes in structure, as exhibited by different crystallographic planes or surface atoms with different coordination numbers. The electronic factor is related to changes in electronic structure as expected for different metals or metal-support interactions or very small metallic clusters.

Because of the frequently observed effect of both geometric and electronic factors on the rate of a catalytic reaction, it came as a surprise to discover a number of reactions with turnover numbers almost identical on particles of a metal with varying sizes between 1 and 10 nm. This discovery made recently in several laboratories was unexpected because of the marked change in the relative proportion of surface atoms of different coordination numbers on particles in this size range. A reaction with invariant turnover number in this size range has been termed structure insensitive. Two additional structure insensitive reactions have been studied recently at Stanford: the hydrogenation of ethylene and of cyclohexene on platinum.

For ethylene hydrogenation on supported platinum catalysts, no effect of support was detected except in one instance. A special kind of support effect, namely hydrogen spillover could be ruled out as contributing to the observed rate. Otherwise, hydrogen spillover would have enhanced the rate of reaction in the presence of alumina as a result of hydrogen atoms diffusing away from platinum onto alumina where they might have hydrogenated chemisorbed ethylene. No such effect was detectable. The only support with which platinum was observed to have a substantially higher turnover number than for all other platinum catalysts, was a Y-zeolite with multivalent cations. However, platinum on a Y-zeolite with Na ions, had a turnover number equal to that of all the normal platinum catalysts. It appears that very small

clusters of platinum in the supercages of the zeolites with multivalent cations are transferring some electronic charge to the zeolitic framework with corresponding increase in the turnover number of platinum. Thus the observed effect is attributed to an electronic factor for a reaction which is insensitive to geometric factors.

The occurrence of structure insensitive reactions may be explained by corrosive chemisorption as a result of which the uppermost layer of metal-adsorbate complexes is not in registry with the underlying metallic layers and acts as an array of surface molecules. This explanation seems particularly appropriate in the case of the hydrogen-oxygen reaction on platinum which we have found to be structure sensitive with excess hydrogen but structure insensitive with excess oxygen. In the latter case, corrosive chemisorption of oxygen seems reasonable. Surface reconstruction of platinum following oxygen chemisorption has indeed been evidenced independently at Stanford by means of hydrogen chemisorption and also rates of hydrogenation of ethylene and cyclohexene on oxygen reconstructed platinum surfaces.

The occurrence of structure sensitive reactions may be explained by the higher reactivity of certain sites (corners, ledges, multiplets) and the problem is then to identify the active sites.

An attempt to do this has just been made in the case of the ammonia synthesis on iron. Metallic iron particles spanning the range from 2 to 30 nm were prepared by using magnesium oxide as a support. Over these particles, the ammonia synthesis at atmospheric pressure between 570 and 680K was found to be a structure sensitive reaction with a turnover number on the small particles being an order of magnitude smaller than that on the large particles. The small particles were then treated with ammonia at 680K so as to obtain a high virtual pressure of nitrogen with formation of an iron nitride. The latter was then decomposed in a hydrogen-nitrogen gas

mixture. After this treatment, the turnover number on the small particles was significantly higher than before but this enhancement disappeared after prolonged treatment of the catalyst in hydrogen.

These observations suggest a surface reconstruction of small iron particles. This reconstruction that seems induced by nitrogen was studied by Mössbauer spectroscopy and the selective chemisorption of carbon monoxide. It was found that those treatments of the small iron particles which increased the turnover number in ammonia synthesis, brought about a decrease in the uptake of carbon monoxide by the catalyst as well as a decrease in the anisotropy energy barrier for the magnetization relaxation of metallic iron. From these results, it is concluded that the increase in turnover number is due to the creation of  $C_i$  surface atoms where a  $C_i$  atom denotes one with  $i$  nearest neighbors. This assignment of active sites for nitrogen chemisorption agrees with that of others, based on field emission microscopy.

### 3. The Structure and Bonding of Lithium Clusters

M. Boudart, K. T. Chow, J. B. Diamond, J. G. Fripiat, and K. H. Johnson

#### A. Introduction

Supported metal catalysts in very small particle sizes are often employed in industry because small particles permit a better utilization of the metal. Since many properties (e. g. morphology, miscibility, electronic properties, magnetic properties and some thermodynamic properties) depend on particle size, this may also be the case for the catalytic activity of small metal particles.

In this report, we ask the simplest question for the metal with the smallest number of electrons, namely lithium. The question is: how large must a cluster of lithium be to possess chemical properties approaching those of the bulk metal?

Our calculation was carried out with the Self Consistent Field-X $\alpha$ -Scattered Wave method (1). The method is based, first of all, on the arbitrary division of matter into component clusters of atoms. The cluster, take Li<sub>3</sub> for instance, is partitioned into three regions as shown in Fig. 1: the first region within nonoverlapping spheres surrounding the constituent atoms, the second region between the atomic spheres and an outer sphere surrounding the entire cluster, and the third region outside the cluster.

The one-electron Schrödinger equations for the cluster are described as:

$$[-\nabla_1^2 + V_c(1) + V_{X\alpha}(1)] U_i(1) = \epsilon_i U_i(1) \quad (1)$$

where:  $\nabla_1^2$  is the kinetic energy term,  $V_c(1)$ , determined classically, is the electrostatic potential at position 1 due to the total electronic and nuclear charge,  $V_X(1)$  is Slater's X $\alpha$  statistical approximation (2) to exchange correlation, namely

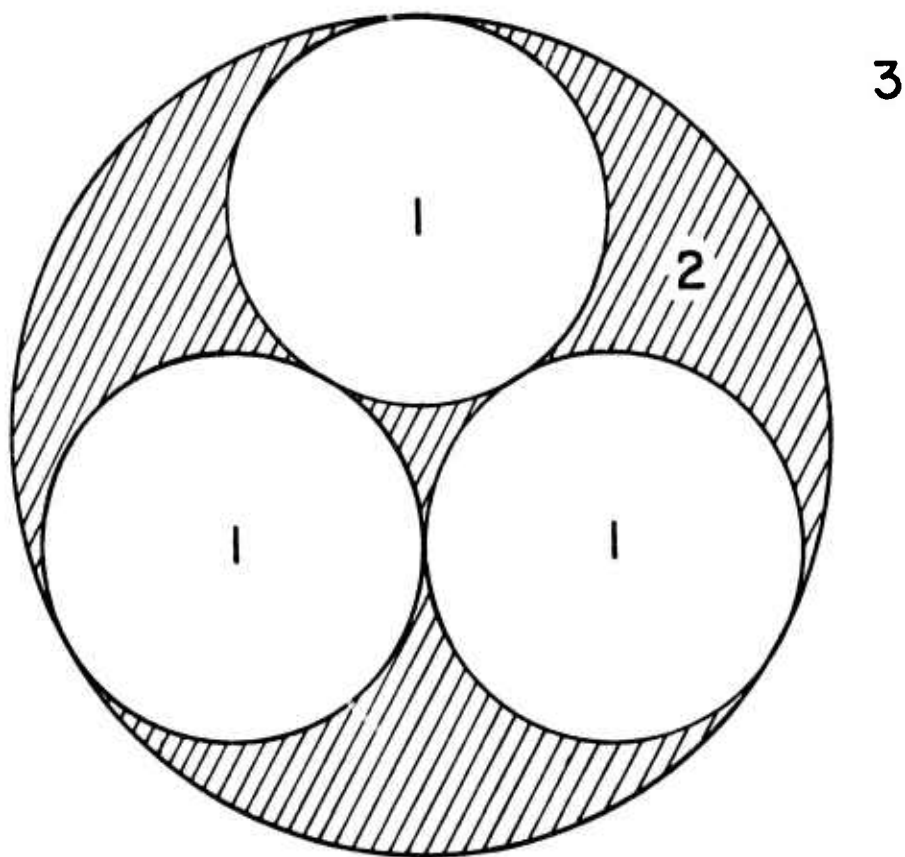


Figure 1. Divided Regions of  $\text{Li}_3$  Cluster

1. atomic
2. interatomic
3. extramolecular

$$\begin{aligned} V_{X\alpha}^{\uparrow}(1) &= -6\alpha \left[ \frac{3}{4\pi} \rho^{\uparrow}(1) \right]^{1/3} \\ V_{X\alpha}^{\downarrow}(1) &= -6\alpha \left[ \frac{3}{4\pi} \rho^{\downarrow}(1) \right]^{1/3} \end{aligned} \quad (2)$$

These potentials are dependent only on the local electronic charge densities  $\rho^{\uparrow}(1)$  and  $\rho^{\downarrow}(1)$  for spin-up and spin-down electrons, respectively, and on the scaling parameter  $\alpha$ . The value of  $\alpha$  is generally chosen to be between 2/3 to 1.

The main objective is to solve the one-electron Schrödinger equations (1) for the spin orbitals  $U_i(1)$  and energy eigenvalues  $\epsilon_i$  of the cluster, subject to the boundary conditions on the clusters. Each spin orbital can be associated with either the spin-up or spin-down Pauli function. Thus the electronic charge density

$$\rho(1) = \sum_i n_i U_i^*(1) U_i(1) \quad (3)$$

can be separated into spin-up  $\rho^{\uparrow}(1)$  and spin-down  $\rho^{\downarrow}(1)$  parts, where  $n_i$  is the occupation number of the  $i$ th spin orbital.

The numerical solutions of equations (1) are found for a polyatomic cluster by first spherically averaging the potential  $V_c(1) + V_{X\alpha}(1)$  inside each of the atomic regions 1 and the extramolecular region 3. The potential is generally assumed to be constant throughout the interatomic region 2, equal to the volume average of  $V_c(1) + V_{X\alpha}(1)$  over this region. This procedure leads to a set of rapidly convergent secular equations which are solved numerically for the molecular-orbital energies and wave functions. The continuity of the wave functions and of their 1st derivatives across each region is taken care of via the scattered-wave formalism (1).

The complete calculation proceeds in the following manner. The eigenfunctions of equations (1) for an initial superposed-atom potential



$V_c(1) + V_{X\alpha}(1)$  are the starting point for a complete SCF- $X\alpha$ -SW calculation. The initial set of spin orbitals  $U_i(1)$  is substituted into expression (3) to obtain the electronic charge density throughout the cluster. This charge density is then substituted into Poisson's equation of classical electrostatics to determine a new Coulomb potential  $V_c(1)$  and into equation (2) to determine a new exchange-correlation potential. As before, these potentials are spherically averaged in regions 1 and 3 and volume averaged in region 2. A weighted average between the new potential and the initial potential serves as input for the first iteration. A new set of spin orbitals is calculated by the scattered-wave method and the entire computational procedure is repeated until self-consistency is attained.

This method permits accurate calculations of electronic structure of polyatomic molecules from first principles (without introducing any experimental parameters) and requires only moderate amounts of computation time compared with the ab initio LCAO-SCF-MO method (3, 4).

The exchange scaling parameter of  $\alpha$  of the lithium atomic sphere was taken from the table given by Schwarz (5). This value ( $\alpha = 0.78147$ ) had been chosen in such a way that the total energy computed for a lithium atom by the  $X\alpha$  method equalled exactly that obtained by a Hartree-Fock calculation. The  $\alpha$  values for the interatomic and extramolecular regions were set equal to that of the atomic region.

Six clusters of lithium, namely  $Li_2$ ,  $Li_3$  (triangular),  $Li_4$  (square),  $Li_8$  (cubic), and  $Li_{13}$  (cubooctahedral  $O_h$  and icosahedral  $I_h$ ) have been studied; their properties were calculated at several internuclear distances. To test the validity of the computational method, the experimental equilibrium interatomic distance of  $Li_2$  was chosen to calculate the corresponding binding energy per atom. The latter was then compared with the experimental value (6). The geometrical parameters employed in our calculations are defined in Fig. 2 and collected in Tables 1 to 5.

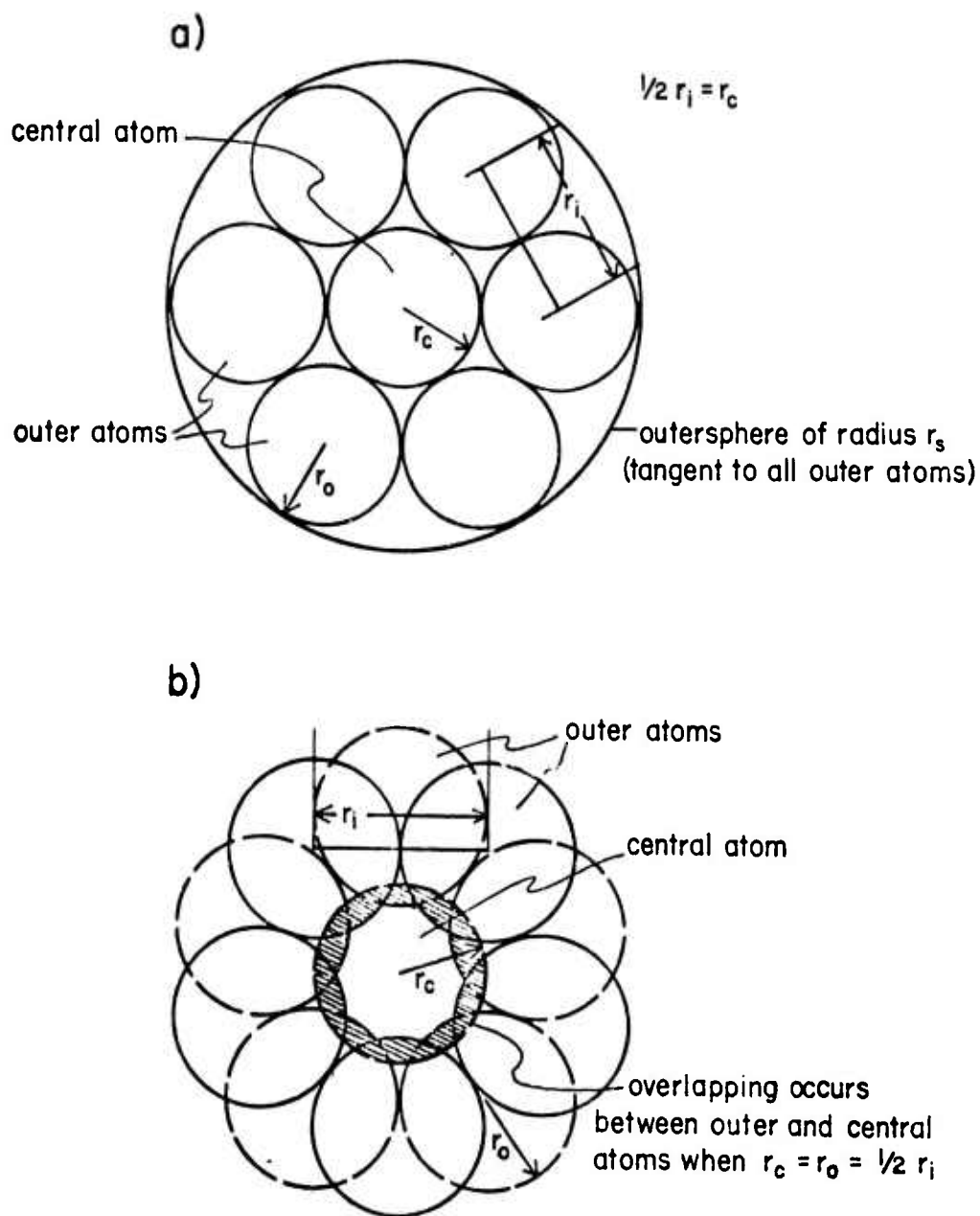


Figure 2. Geometries for different close-packed systems.

- a) General Close-packed geometry
- b) Close-packed geometry for icosahedron

Table 1. Bond length and sphere radii for  $\text{Li}_3$  (triangular) (in Å).

	A	B	C	D
$r_i$	2.67	2.73	2.79	3.03
$r_o$	1.34	1.37	1.40	1.52
$r_s$	2.88	2.94	3.01	3.27

Table 2. Bond length and sphere radii for  $\text{Li}_4$  (square) (in Å).

	A	B
$r_i$	2.89	3.52
$r_o$	1.45	1.76
$r_s$	3.49	4.25

Table 3. Bond length and sphere radii for  $\text{Li}_8$  (cube) (in Å).

	A	B	C	D	E
$r_i$	2.12	2.67	2.96	3.18	3.70
$r_o$	1.06	1.34	1.48	1.59	1.85
$r_s$	2.90	3.66	4.04	4.34	5.05

Table 4. Bond length and sphere radii for the  $\text{Li}_{13}$  (icosahedral) (in Å).

	A	B	C	D	E
$r_{\text{c-o}}$	2.89	2.96	3.05	3.23	3.49
$r_i$	3.04	3.12	3.20	3.39	3.67
$r_o$	1.52	1.56	1.60	1.70	1.84
$r_s$	4.42	4.52	4.65	4.92	5.33

Table 5. Bond length and sphere radii for the  $\text{Li}_{13}$  (cubooctahedral) (in Å).

	A	B	C	D	E
$r_i$	2.67	2.86	3.05	3.33	3.49
$r_o$	1.34	1.43	1.53	1.67	1.75
$r_s$	4.01	4.29	4.57	5.00	5.24

In general, a close-packed geometry requires the radius of the atomic sphere to be equal to half of the internuclear distance between two nearest atoms (Fig. 2a). However, for a close-packed icosahedral structure (Fig. 2b), the central atom must be slightly smaller than the outer atom. In our calculations, the radius of the atomic sphere,  $r_c$ , was chosen to be equal to half of the distance ( $r_i$ ) between two adjacent outer-atoms. Consequently, a very small overlap existed between the central atomic sphere and the outer atomic spheres (overlapping volumetric ratio: 4% for central atomic sphere and 0.3% for each of the outer spheres). Furthermore, the radius of the sphere delimiting the extra-molecular region was chosen for each case in such a way that the sphere was tangent to all outer atomic spheres.

Except for the  $\text{Li}_2$  molecule and  $\text{Li}_8$  cluster, all other clusters were treated as open-shell systems and calculations were carried out in spin-unrestricted form so that the effect of spin polarization was accounted for. Initially frozen core states were relaxed at the end of each complete calculation.  $\text{Li}_2$  and  $\text{Li}_8$  were not treated as open-shell systems because their occupied orbitals are completely filled.

## B. Results and Discussion

### (1) Equilibrium internuclear distance

The results obtained for the five clusters are collected in Tables 6 to 12. Equilibrium internuclear distances  $r_c$  of  $\text{Li}_3$ ,  $\text{Li}_8$ , and  $\text{Li}_{13}$  clusters were determined graphically on a plot of energy versus interatomic distances  $r_i$ . For instance, the curve of total energy  $E_T$  of  $\text{Li}_3$  versus interatomic distance  $r_i$  has a minimum corresponding to the equilibrium state of the system at the equilibrium interatomic distance  $r_c^0 = 2.76 \text{ \AA}$  (Fig. 3). On the other hand, the virial theorem suggests that  $r_c$  for  $\text{Li}_3$  would be

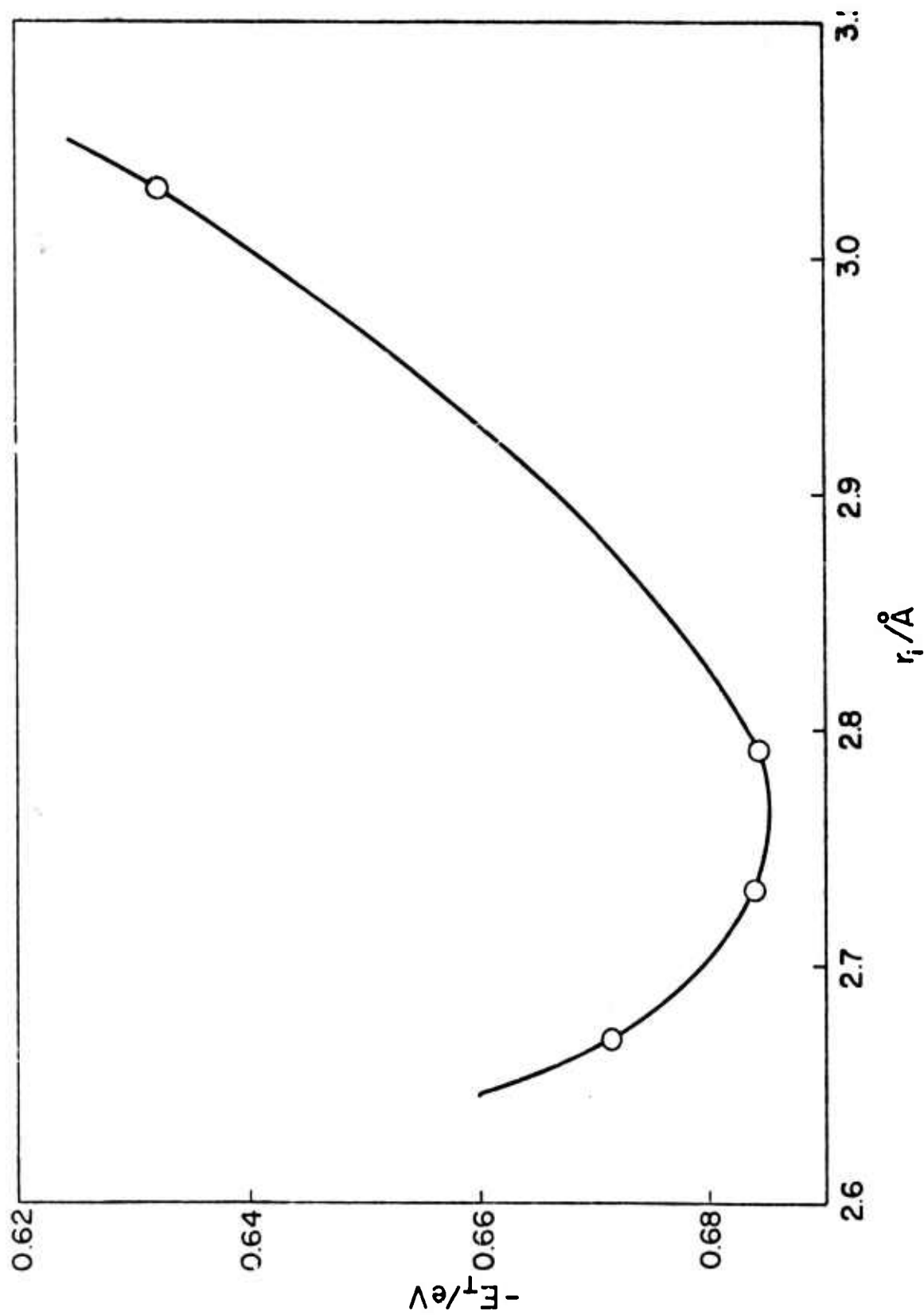


Figure 3. Total Energy  $E_T$  vs Interatomic Distance  $r_i$  for  $\text{Li}_3$  (triangular)  
 $-E_T = (580.0 + \text{value on scale})$ .



Table 6. Electronic properties of Lithium atom and  $\text{Li}_2$  molecule.

A) <u>Lithium atom:</u> (results obtained from Herman Skillman program)		
Total Energy = -202.17 eV		
$\epsilon_{1s} = -52.81 \text{ eV}, \quad \epsilon_{2s} = -2.58 \text{ eV}$		
$\alpha_{\text{Li}} = 0.78147$		
B) <u><math>\text{Li}_2</math> molecule</u>		
Bond length ( $r_i$ )	=	2.67 Å
radius ( $r_o$ )	=	1.34 Å
$r_s$	=	2.67 Å
$\alpha_{\text{Li}}$ (from atomic data)	=	0.78147
Total Energy	=	-405.13 eV
Total Kinetic Energy	=	405.46 eV
Virial ratio	=	1.0008
Total Energy per atom	=	-202.56 eV
Binding Energy per atom	=	0.392 eV
$\epsilon_{\text{core state}}$	=	-52.78 eV
$\epsilon_{\sigma g}$	=	-3.22 eV
Charge densities: $q_{\text{Li}}$	=	2.27
$q_{\text{interatomic}}$	=	1.02
$q_s$	=	0.44

Table 7. Electronic properties of  $\text{Li}_3$  (triangular)

Energy in eV and distance in $\text{\AA}$				
Interatomic Distance $r_i$	2.67	2.73	2.79	3.03
Total Energy	-607.47	-607.48	-607.48	-607.43
Kinetic Energy	608.52	608.06	607.72	606.22
Virial ratio	1.0017	1.0009	1.0003	0.9980
Total Energy/atom	-202.49	-202.49	-202.49	-202.49
Binding Energy/atom	0.341	0.341	0.341	0.313
<u>Orbital Energies</u>				
core state 1	-53.04	-53.07	-53.12	-53.23
$a_1^1$ 1	-4.42	-4.41	-4.39	-4.34
$a_2''$ 1	-2.68	-2.64	-2.61	-2.49
$e_1^1$ 1			-2.50	
$a_1^1$ 1			-1.14	
core state 1	-53.01	-53.04	-53.05	-53.19
$a_1^1$ 1	-3.58	-3.58	-3.59	-3.59
$a_2''$ 1			-1.74	
$e_1^1$ 1			-1.70	
$a_1^1$ 1			-0.50	
<u>Charge densities</u>				
$q_s$	0.587	0.559	0.533	0.444
$q_{\text{Li}}$	2.306	2.318	2.329	2.372
$q_{\text{interatomic}}$	1.492	1.485	1.478	1.440

Table 8. Electronic properties of  $\text{Li}_4$  (square)

Energy in eV and distance in $\text{\AA}$		
Interatomic Distance $r_i$	2.89	3.52
Total Energy	-810.07	-810.33
Kinetic Energy	813.15	810.24
Virial ratio	1.0040	0.9999
Total Energy/atom	-202.52	-202.58
Binding Energy/atom	0.340	0.413
<u>Orbital Energies</u>		
core state 1	-53.07	-53.08
$a_{1g}$ 1	-4.81	-4.39
$e_u$ 1	-3.18	-3.22
core state 1	-52.85	-52.92
$a_{1g}$ 1	-3.50	-3.19
<u>Charge densities</u>		
$q_s$	0.611	0.344
$q_{\text{Li}}$	2.393	2.523
$q_{\text{interatomic}}$	1.819	1.564

Table 9. Electronic properties of  $\text{Li}_8$  (cube)

Energy in eV and distance in Å					
Interatomic Distance $r_i$	2.12	2.67	2.96	3.18	3.70
Total Energy	-1618.27	-1623.60	-1623.60	-1623.51	-1622.60
Kinetic Energy	1662.12	1631.90	1624.37	1620.51	1614.56
Virial ratio	1.0271	1.0054	1.0005	0.9982	0.9950
Total Energy/atom	-202.28	-202.90	-202.95	-202.94	-202.83
Binding Energy/atom	0.113	0.730	0.781	0.769	0.655

Orbital	Orbital Energies in eV (at equilibrium $r_i = 2.96 \text{ Å}$ )
core state (1s)	-52.81
$a_{1g}$	-5.34
$t_{1u}$	-3.90
$e_g$	-2.73
$a_{1g}$	-2.26
$t_{2g}$	-2.23

Table 10. Electronic properties of  $\text{Li}_{13}$  (Icosahedral)

Energy in eV and distance in Å					
Interatomic Distance $r_i$	2.89	2.96	3.05	3.23	3.49
Total Energy	-2639.90	-2640.25	-2640.55	-2640.78	-2640.43
Kinetic Energy	2656.27	2652.46	2648.90	2640.51	2631.65
Virial ratio	1.0062	1.0046	1.0029	0.9999	0.9966
Total Energy/atom	-203.08	-203.10	-203.12	-203.14	-203.12
Binding Energy/atom	0.899	0.925	0.949	0.967	0.940
<u>Orbital Energies</u>					
core state 1 ↑	-52.78	-52.77	-52.75	-52.74	-52.73
core state 2 ↑	-52.55	-52.86	-52.73	-52.78	-52.99
1 a <sub>1g</sub> ↑	-7.02	-6.92	-6.80	-6.55	-6.19
1 t <sub>1u</sub> ↑	-5.46	-5.41	-5.34	-5.19	-4.97
1 H <sub>g</sub> ↑	-3.89	-3.87	-3.86	-3.83	-3.79
2 a <sub>1g</sub> ↑				-3.57	
1 g <sub>u</sub> ↑				-2.66	
2 t <sub>1u</sub> ↑				-2.10	
2 t <sub>2u</sub> ↑				-1.72	
core state 1 ↓	-52.89	-52.89	-52.86	-52.85	-52.85
core state 2 ↓	-52.39	-52.43	-52.49	-52.63	-52.84
1 a <sub>1g</sub> ↓	-6.01	-5.93	-5.84	-5.65	-5.37
1 t <sub>1u</sub> ↓	-4.29	-4.24	-4.19	-4.08	-3.92
1 H <sub>g</sub> ↓				-2.59	
2 a <sub>1g</sub> ↓				-2.58	
1 g <sub>u</sub> ↓				-1.49	
2 t <sub>1u</sub> ↓				-1.37	
2 t <sub>2u</sub> ↓				-0.74	
<u>Charge densities</u>					
q <sub>s</sub>	1.071	1.004	0.928	0.783	0.626
q <sub>c</sub>	3.117	3.119	3.121	3.129	3.142
q <sub>o</sub>	2.601	2.610	2.619	2.636	2.659
q <sub>interatomic</sub>	3.602	3.563	3.524	3.456	3.324

Table 11. Electronic properties of  $\text{Li}_3$  (cubooctahedral)

Energy in eV and distance in Å					
Interatomic Distance $r_i$	2.67	2.86	3.05	3.33	3.49
Total Energy	-2634.99	-2637.24	-2638.40	-2638.97	-2638.78
Kinetic Energy	2676.79	2661.83	2651.18	2637.18	2632.29
Virial ratio	1.0159	1.0093	1.0048	0.9993	0.9975
Total Energy/atom	-202.69	-202.87	-202.95	-202.99	-202.98
Binding Energy/atom	0.530	0.694	0.775	0.830	0.816
<u>Orbital Energies</u>					
core state 1 ↑	-53.52	-53.39	-53.29	-53.33	-53.37
core state 2 ↑	-52.50	-52.56	-52.66	-52.95	-53.08
1 a <sub>1g</sub> ↑	-6.88	-6.67	-6.45	-6.15	-5.98
1 t <sub>1u</sub> ↑	-5.26	-5.15	-5.04	-4.88	-4.77
1 t <sub>2g</sub> ↑	-3.54	-3.52	-3.50	-3.51	-3.51
2 a <sub>1g</sub> ↑				-3.20	
1 e <sub>g</sub> ↑				-2.90	
1 a <sub>2u</sub> ↑				-2.75	
core state 1 ↓	-53.54	-53.41	-53.30	-53.34	-53.38
core state 2 ↓	-52.46	-52.52	-52.63	-52.92	-53.05
1 a <sub>1g</sub> ↓	-6.66	-6.47	-6.26	-5.98	-5.82
1 t <sub>1u</sub> ↓	-5.03	-4.93	-4.82	-4.68	-4.58
1 t <sub>2g</sub> ↓	-3.28	-3.27	-3.26	-3.30	-3.30
2 a <sub>1g</sub> ↓				-3.05	
1 e <sub>g</sub> ↓				-2.71	
1 a <sub>2u</sub> ↓				-2.53	
<u>Charge densities</u>					
q <sub>s</sub>	1.505	1.253	1.060	0.817	0.721
q <sub>c</sub>	2.959	2.959	2.967	2.971	2.978
q <sub>o</sub>	2.511	2.535	2.557	2.576	2.587
q <sub>interatomic</sub>	4.403	4.366	4.290	4.304	4.252



Table 12. Summary of some correlation data for all Lithium clusters considered (Energy in eV and distance in Å)

	Lithium atom	Li <sub>2</sub>	Li <sub>3</sub>	Li <sub>4</sub>	Li <sub>8</sub>	Li <sub>13</sub> O <sub>h</sub>	Li <sub>13</sub> I <sub>h</sub>	Li crystal (B. C. C.)
Interatomic Distance r <sub>e</sub>		2.67	2.79	3.52	2.96	3.23	3.23	3.08 <sup>††</sup> 3.03 <sup>†</sup>
Binding Energy per atom, B		0.392 0.546 <sup>†</sup>	0.341	0.413	0.786	0.830	0.967	1.142 <sup>††</sup> 1.632 <sup>†</sup>
Total Energy per atom, E <sub>T</sub>	-202.7	-202.56	-202.49	-202.58	-202.95	-202.99	-203.14	
Total Energy E <sub>T</sub>		-405.13	-607.48	-810.33	-1623.60	-2638.97	-2640.78	
Kinetic Energy		405.46	607.72	810.24	1624.37	2637.18	2640.51	
Virial ratio (Total Energy/ Kinetic Energy)		1.0008	-1.0003	0.9998	1.0005	0.9993	0.9999	

<sup>†</sup> Experimental Value, ref. 6

<sup>††</sup> Theoretical Values, ref. 11

<sup>#</sup> Experimental Values, ref. 11

about 2.81 Å (Fig. 4). The discrepancy between both values of  $r_e$  is probably due to some round-off error introduced during the calculation. Anyhow, it was felt that  $r_e$  would be somewhere between 2.76 Å and 2.81 Å. If a virial ratio (total energy/kinetic energy) with an accuracy up to  $10^{-3}$  was considered satisfactory for our present purpose, the value 1.0003 (Table 12) would then be acceptable, thus  $r_e$  of  $\text{Li}_3$  was taken to be 2.79 Å from our calculation. Likewise, the value of  $r_e$  for cubic  $\text{Li}_8$  was found to be 2.96 Å. In a similar fashion,  $r_e$  of both  $\text{Li}_{13}(\text{O}_h)$  and  $\text{Li}_{13}(\text{I}_h)$  was estimated to be 3.23 Å (Figs. 5 to 8). To fit the five data points in Fig. 5, the curve was approximated by a parabola:

$$E_T - E_O = \frac{1}{2}k(r_i - r_e)^2$$

where  $E_T$  is the total energy corresponding to the distance  $r_i$ , and  $E_O$  is the minimum total energy corresponding to the equilibrium interatomic distance  $r_e$ . The fit was considered adequate.

## (2) Spin-orbital energy levels of the clusters

The spin-polarized SCF-X $\alpha$ -SW electronic energy levels of  $\text{Li}_3(\text{D}_{3h})$ ,  $\text{Li}_4(\text{D}_{4h})$ ,  $\text{Li}_8(\text{O}_h)$ , and  $\text{Li}_{13}(\text{O}_h$  and  $\text{I}_h)$  clusters are depicted in Figs. 9 through 11. The levels are labeled according to the irreducible representations of their symmetry group. The highest occupied levels in the ground state were found to be  $a_2''$  for  $\text{Li}_3$ ,  $a_{1g}$  for  $\text{Li}_4$ ,  $1 t_{1u}$  for  $\text{Li}_8$ ,  $1 t_{2g}$  for  $\text{Li}_{13}(\text{O}_h)$  and  $1 H_g$  for  $\text{Li}_{13}(\text{I}_h)$ .

The bonding status of each spin orbital was determined through the sign of the coefficient of the expanded spin-orbital in each region. For  $\text{Li}_3$ , the first ( $a_1'$ ) and second ( $a_2''$ ) occupied valence orbitals were found to be completely bonding.

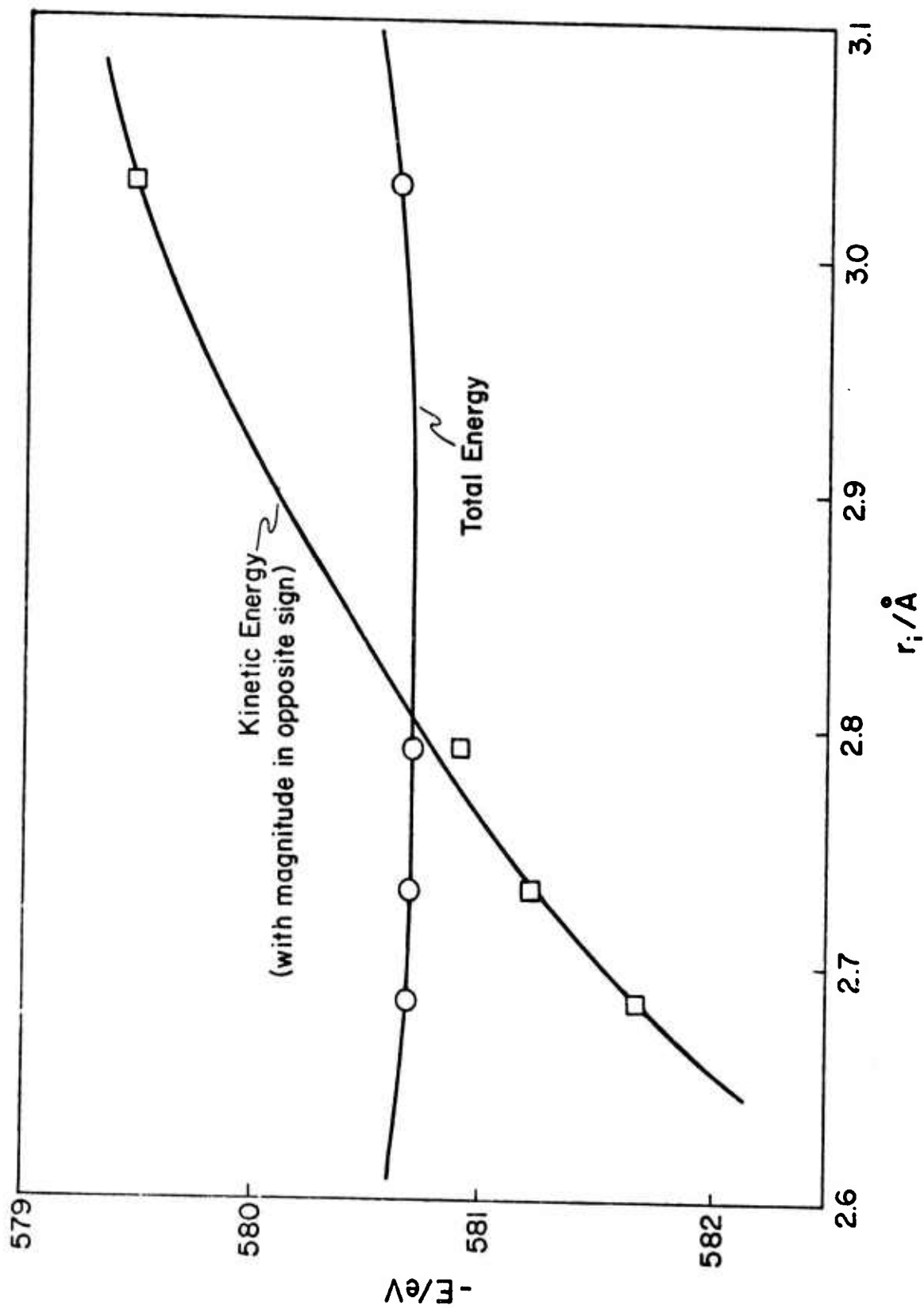


Figure 4. Energy  $E$  vs Interatomic Distance  $r_i$  for  $\text{Li}_3$  (triangular)

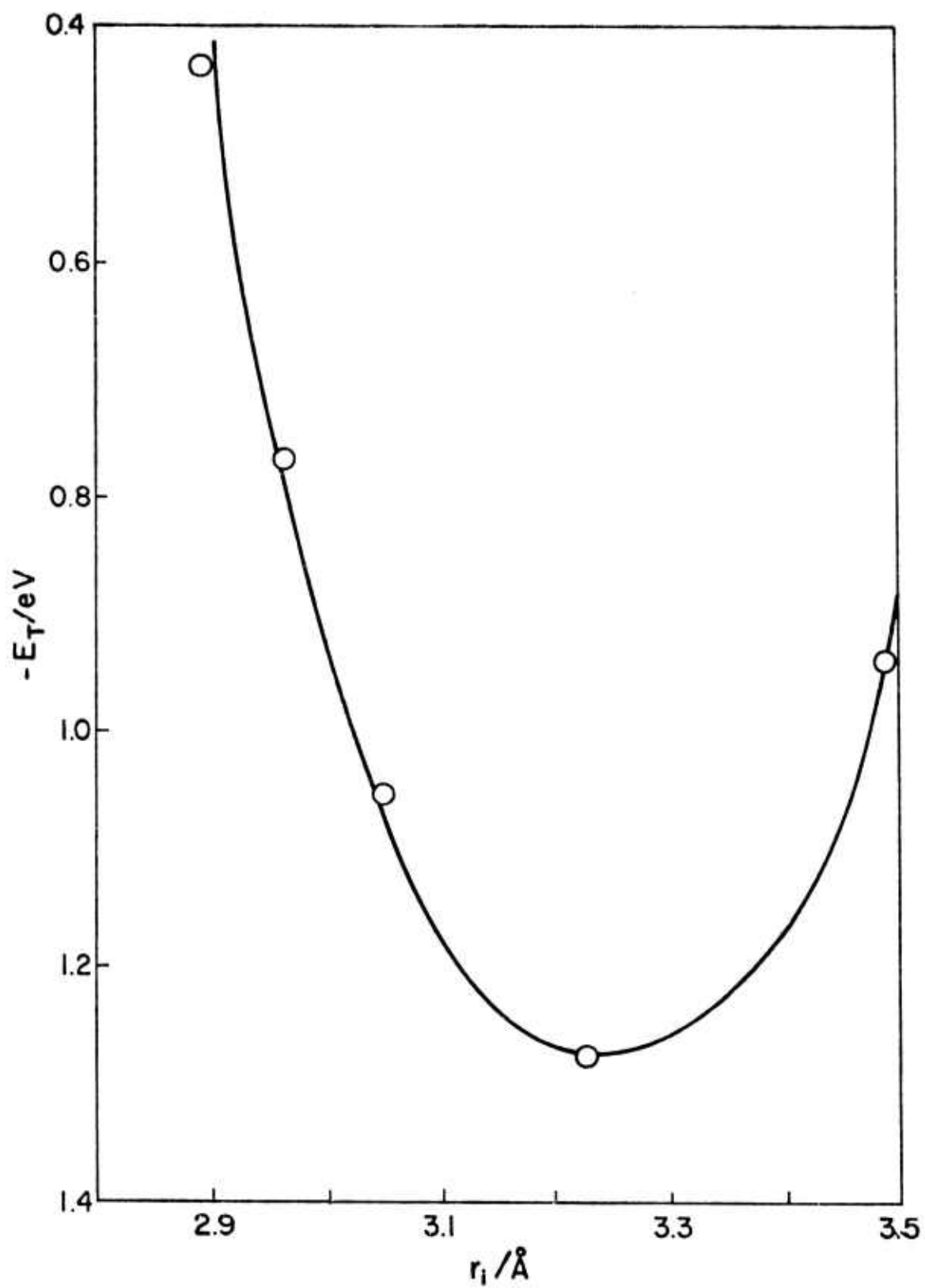


Figure 5. Total Energy  $E_T$  vs Interatomic Distance  $r_i$  for  $I_h Li_{13}$   $-E_T = (2523.0 + \text{value on scale})$ .

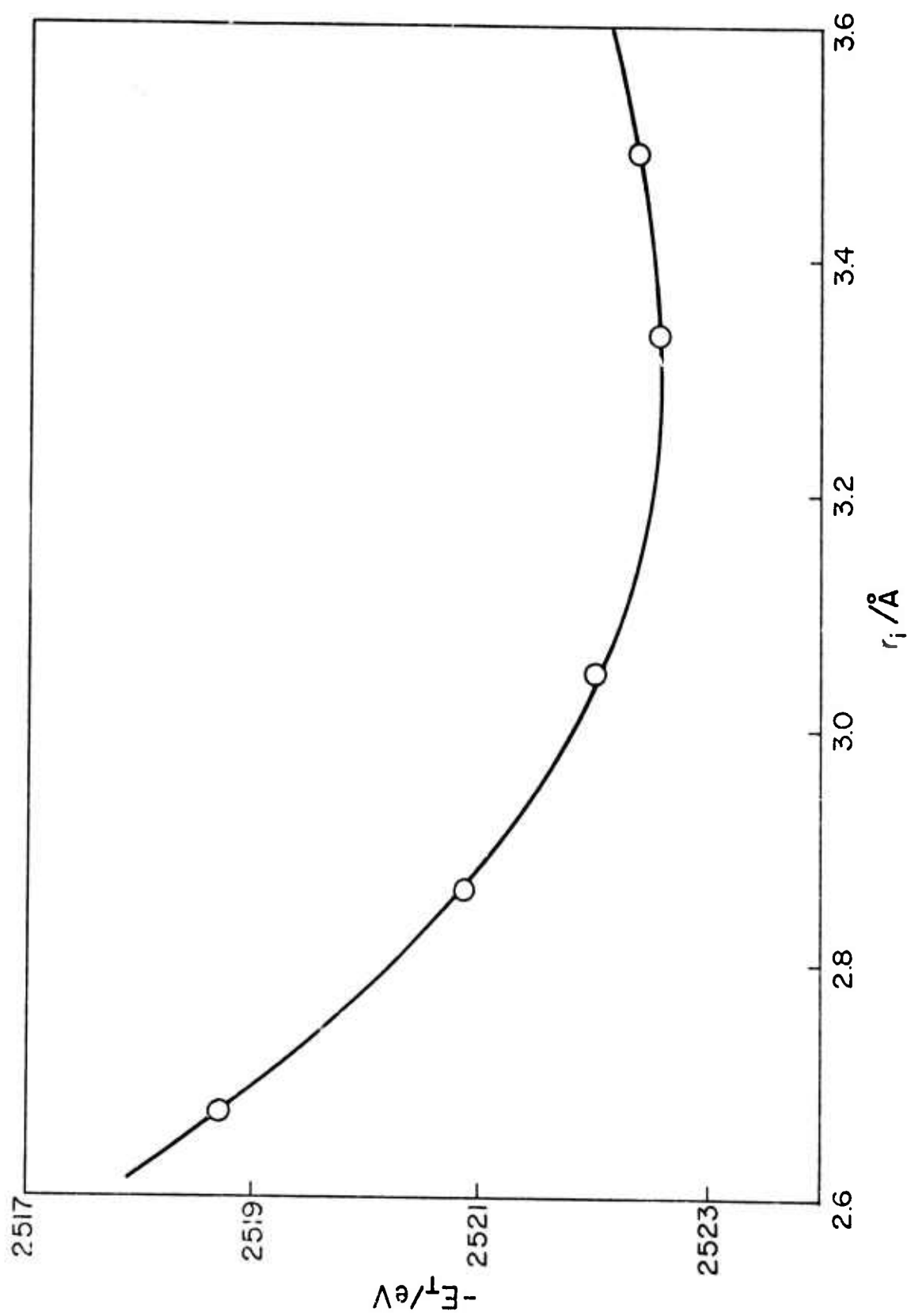


Figure 6. Total Energy  $E_T$  vs Interatomic Distance  $r_i$  for  $O_h Li_{13}$

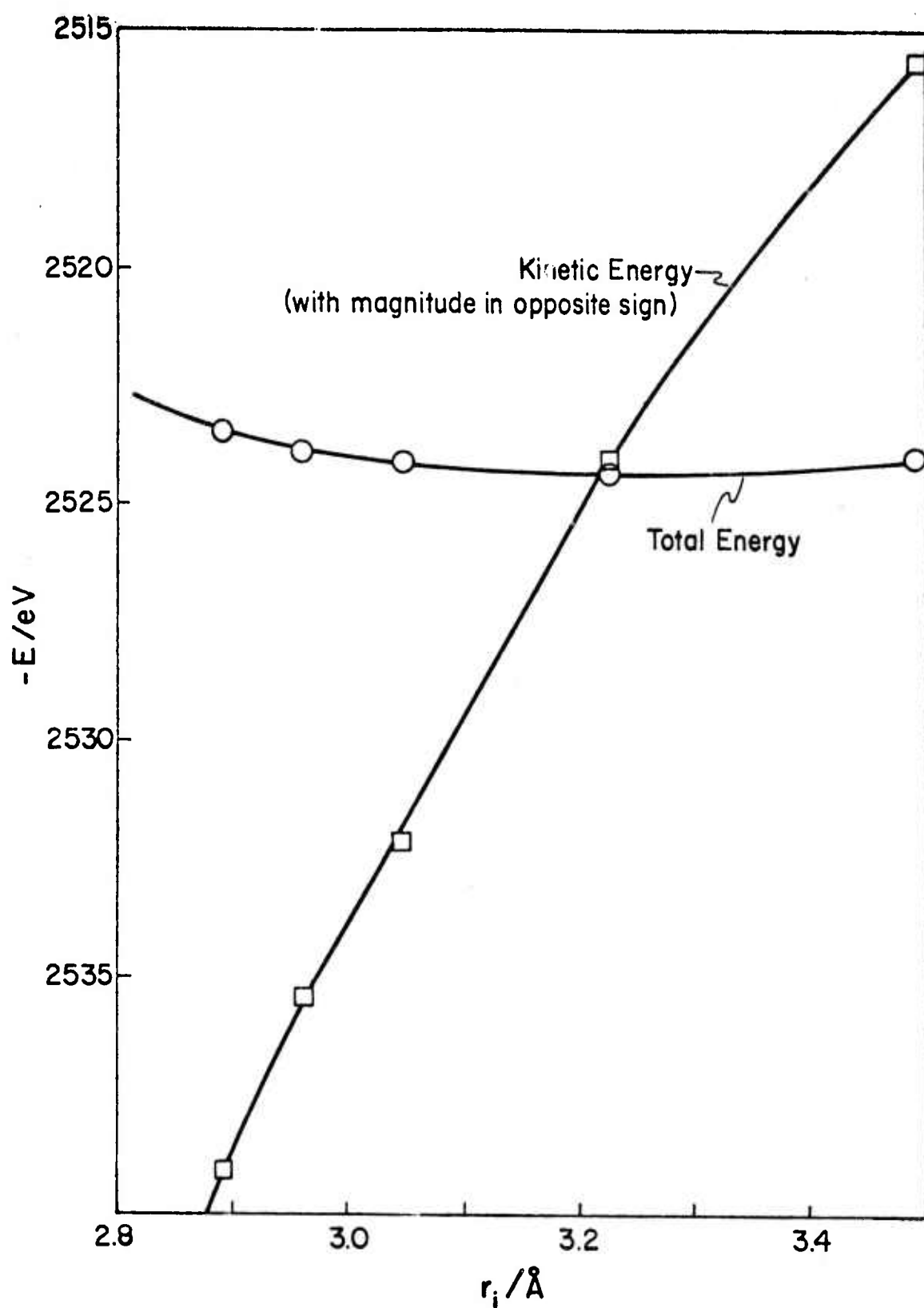


Figure 7. Energy  $E$  vs Interatomic Distance  $r_i$  for  $I_h Li_{13}$



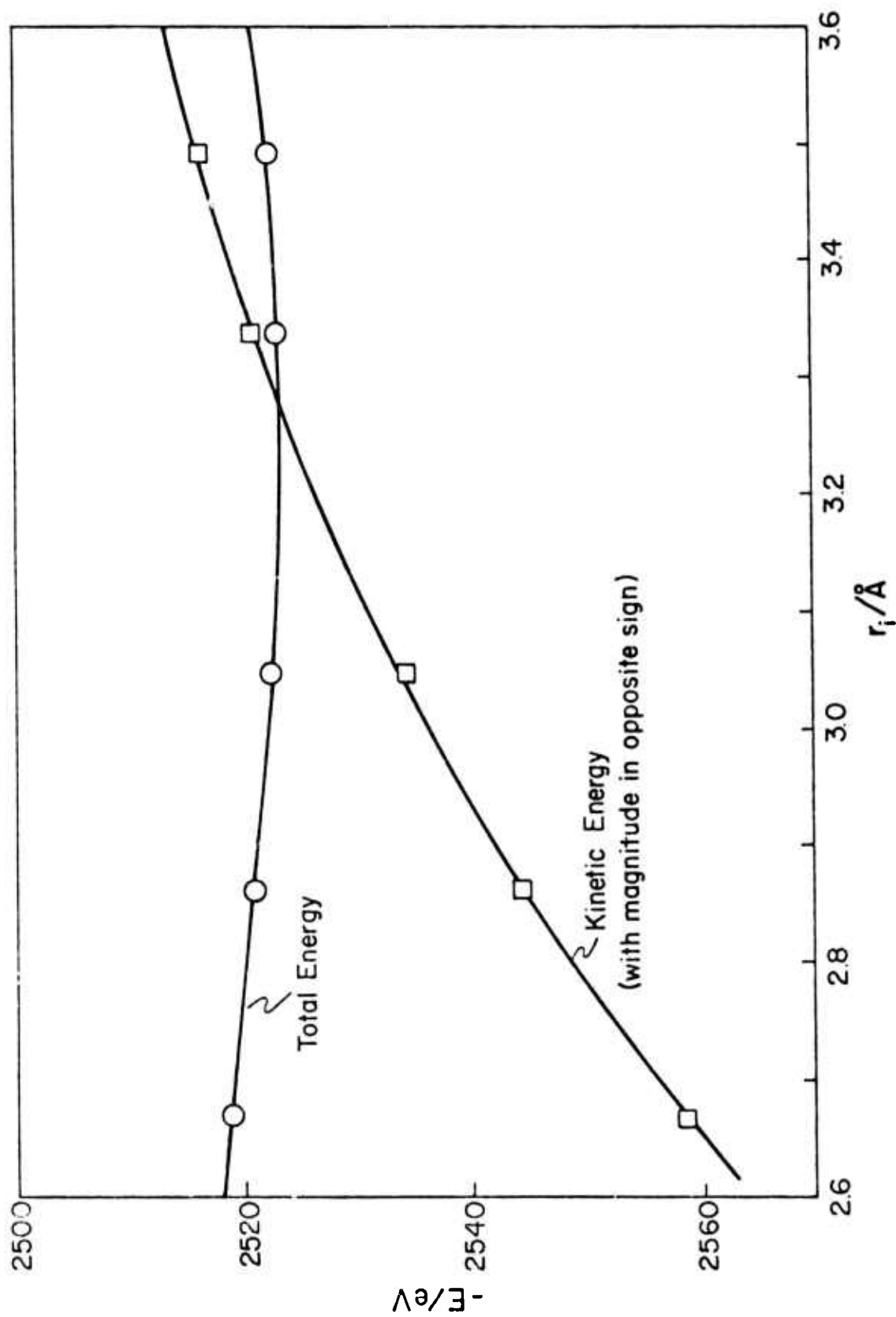


Figure 8. Energy  $E$  vs Interatomic Distance  $r_i$  for  $O_h Li_{13}$

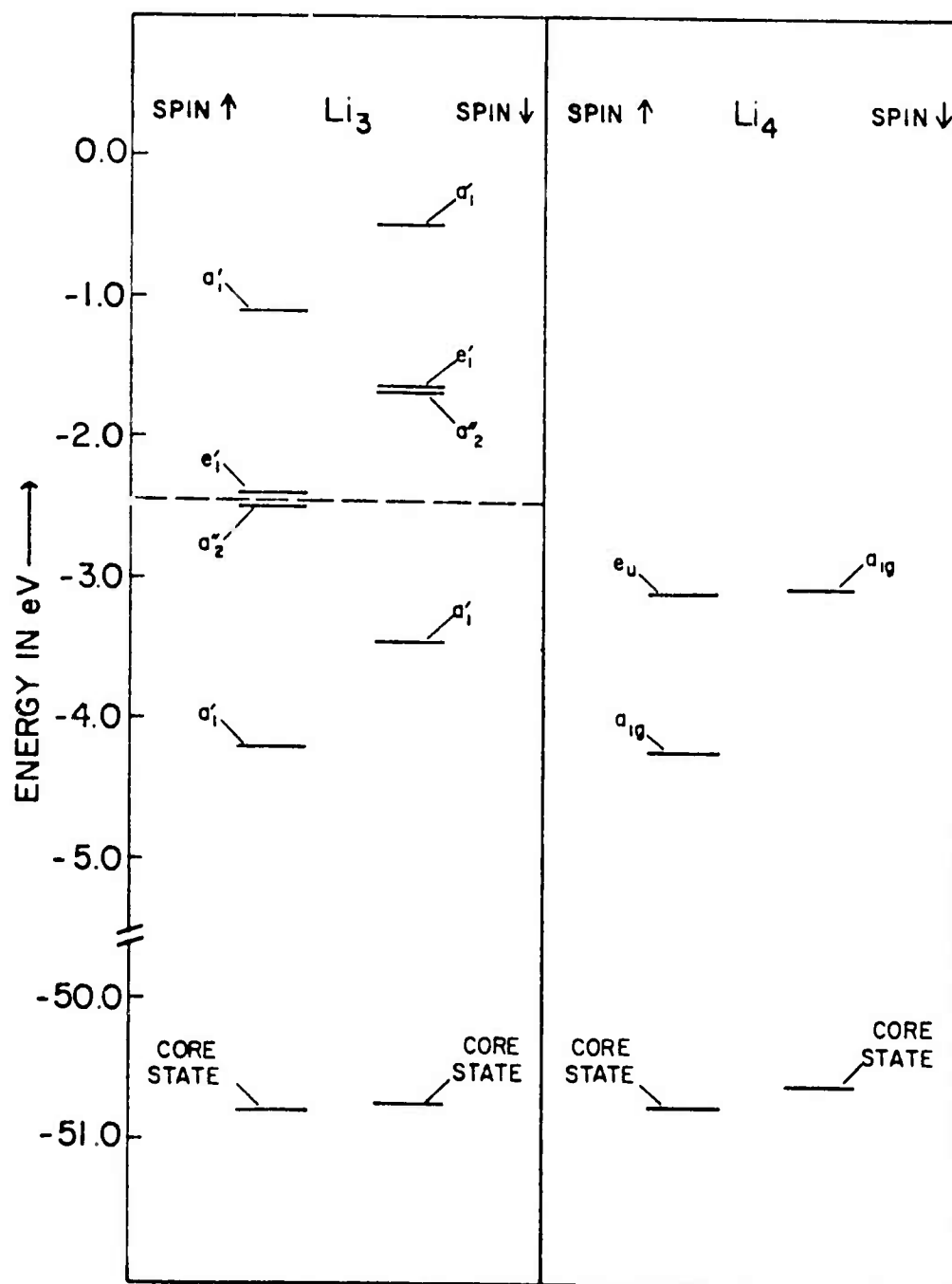


Figure 9. The spin-polarized SCF-X $\alpha$ -SW electronic energy levels of  $\text{Li}_3$  and  $\text{Li}_4$  clusters. The levels are labeled according to the irreducible representations of the triangular- and square-planar ( $D_{3h}$  and  $D_{4h}$ ) symmetry groups for  $\text{Li}_3$  and  $\text{Li}_4$  respectively. The highest occupied levels in the ground state are  $a_1'$  for  $\text{Li}_3$  and  $a_{1g}$  for  $\text{Li}_4$ . Those levels above the dotted line are unoccupied.

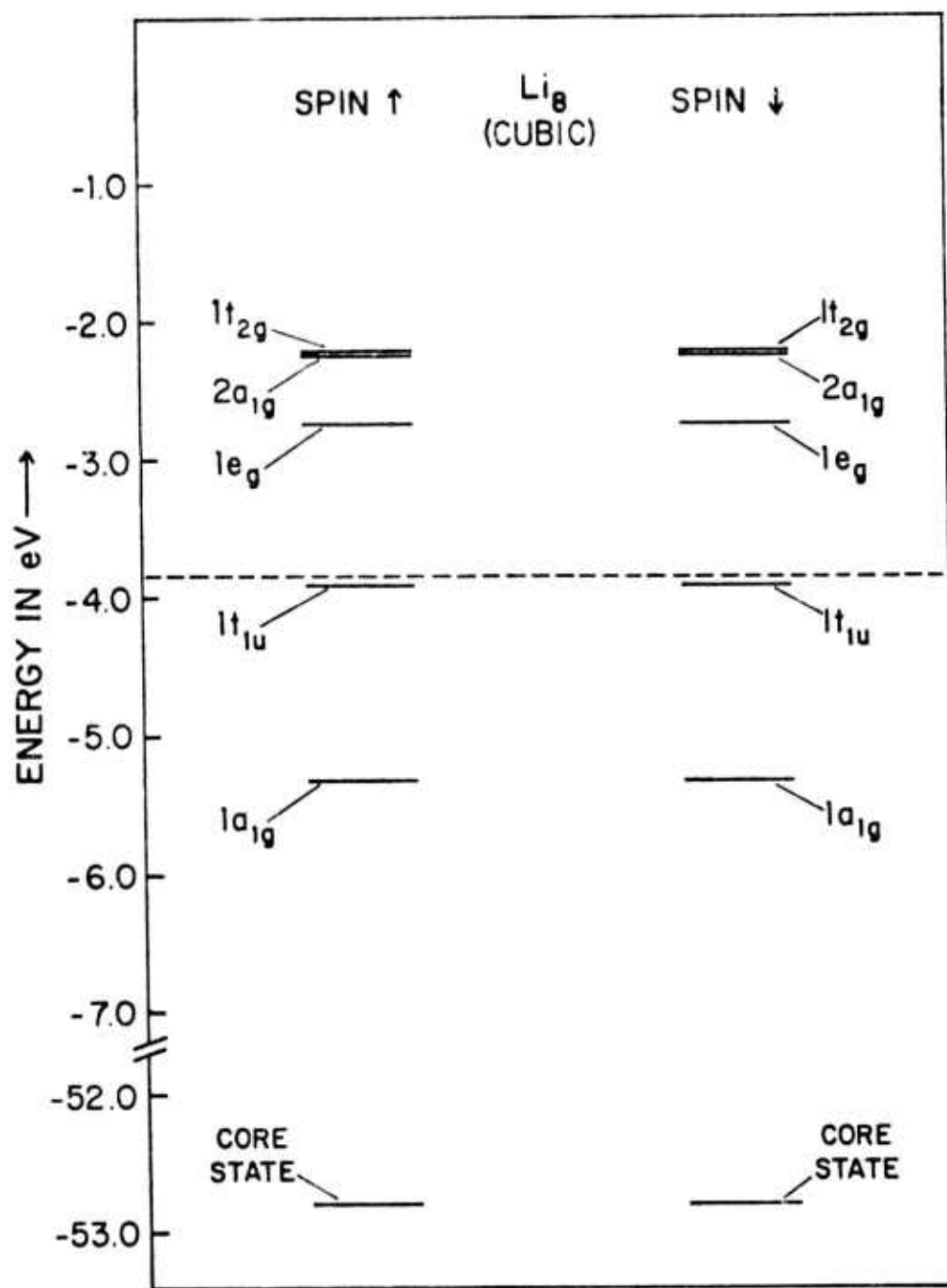


Figure 10. SCF - X $\alpha$ -SW electronic energy levels of a cubic  $\text{Li}_8$  cluster. The levels are labelled according to the irreducible representative of the cubic ( $O_h$ ) symmetry group. The highest occupied levels are  $1t_{1u}\uparrow$  and  $1t_{1u}\downarrow$ . This is a closed-shell system so that the net spin polarization is zero. Levels above the dotted line are unoccupied.

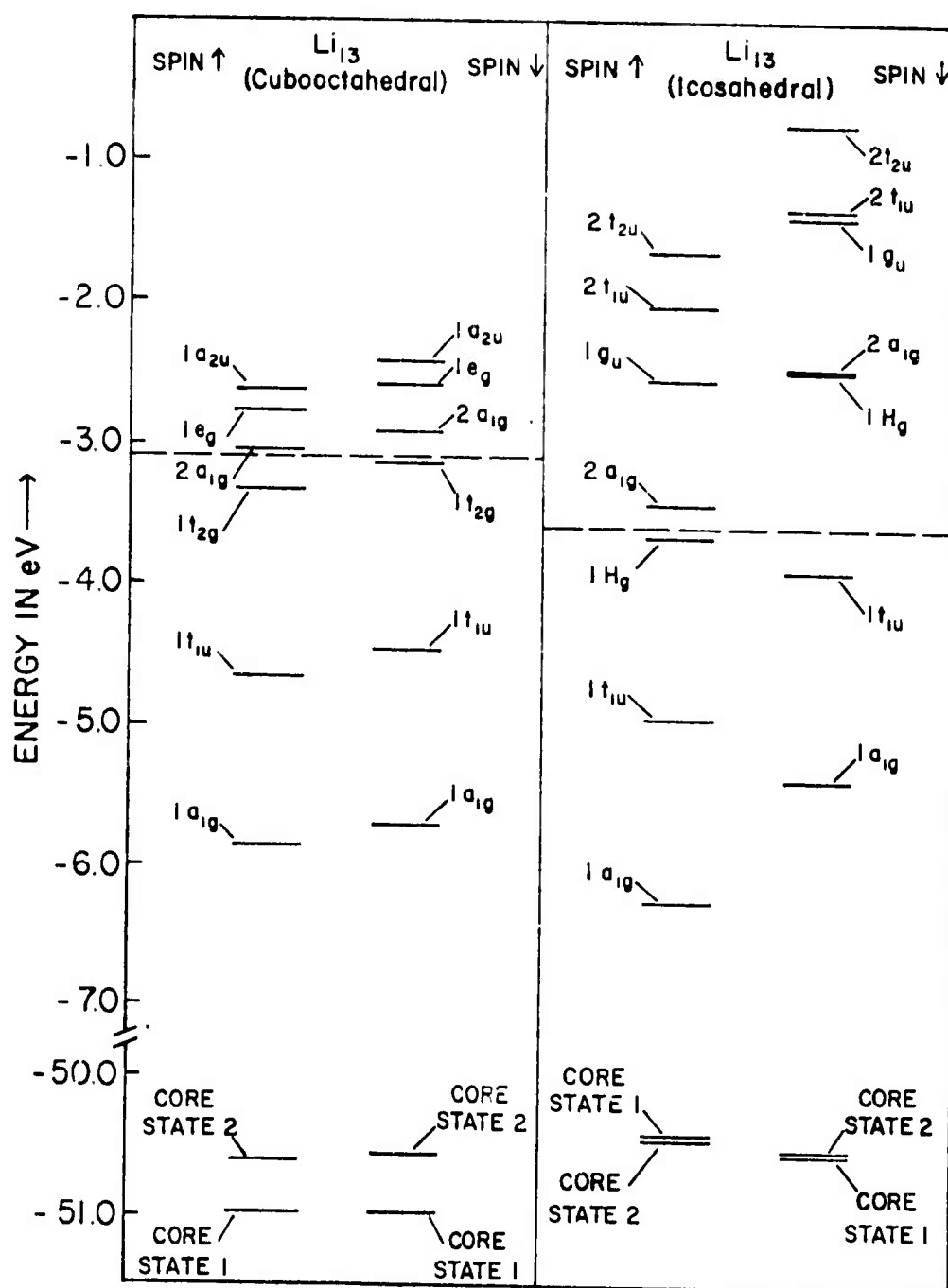


Figure 11. The spin-polarized SCF-Xα-SW electronic energy levels of  $\text{Li}_{13}$  (Icosahedral and Cubooctahedral) Clusters. The levels are labeled according to the irreducible representations of the  $I_h$  and  $O_h$  symmetry groups. The highest occupied levels in the ground state are  $1t_{2g}$  for  $O_h$  and  $1H_g$  for  $I_h$ . Levels that lie above the dotted line are unoccupied.

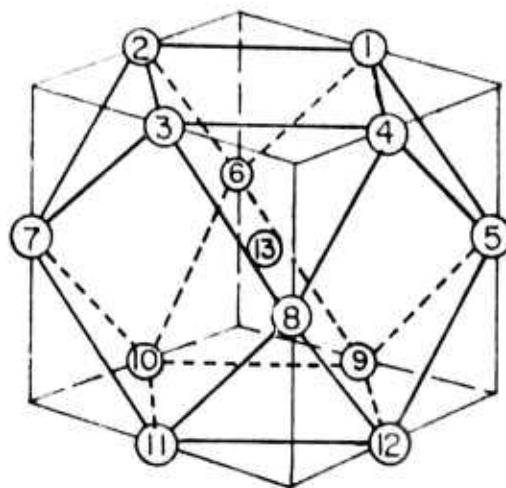
Relevant results in Tables 10 and 11 reveal that three valence molecular orbitals are occupied in the ground state for both the icosahedral and cubooctahedral  $\text{Li}_{13}$  clusters. The first orbital in both geometries was found to be completely bonding and characterized by the symmetry label  $a_g$  (or  $a_{1g}$  for the  $O_h$  group). The second occupied molecular orbital is classified as  $t_{1u}$  for the icosahedron. It assumes a bonding character in both the upper and lower parts of the molecule but an antibonding character existing between the two parts is counterbalanced by the small contribution from  $p_z$  spherical harmonics of the central atom. On the contrary, the highest occupied molecular orbital is described as bonding both in and between the two pentagonal planes but antibonding between atom 1 (or 12) and its corresponding adjacent planes (Fig. 12b). This orbital is characterized by the  $H_g$  irreducible representation. The anti-bonding character is again moderated by the contribution from the central atom though this time it is due to the  $d$  spherical harmonics.

As far as the cubooctahedron is concerned, the second orbital classified as  $t_{1u}$  is found to be bonding in each plane and nonbonding between adjacent planes (Fig. 12a). The latter character is counteracted by the contribution of the  $p$  function of the central atom. The last occupied molecular orbital falls into the  $t_{2g}$  category. This orbital is mostly antibonding except for the bonds between the central atom and the outer atoms.

### (3) Binding energy and other data

The binding energy  $B$  is defined as the amount of energy holding a number of atoms together, divided by the number of atoms. In our calculations, the magnitude of  $B$  was determined by the difference between the total energy of the entire cluster and the sum of the energies of all of its separated atoms. The values of  $B$  for all clusters are shown in Table 12.

a)



b)

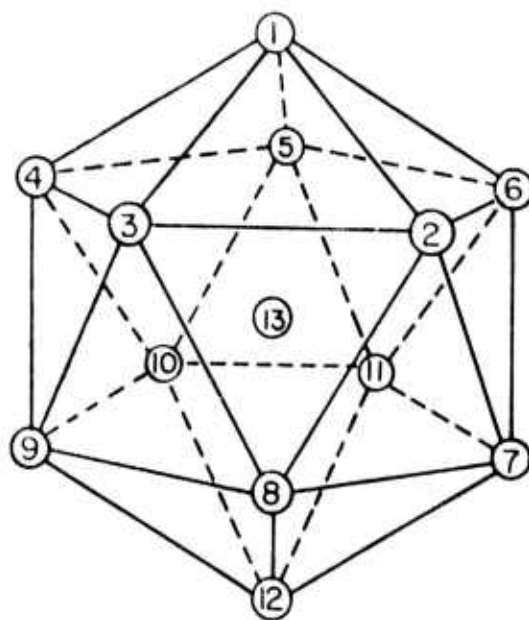


Figure 12. Geometry of a) Cuboctahedron  
b) Icosahedron



To test the validity of the computational method, the experimental value of  $r_e$  (2.67 Å) for  $\text{Li}_2$  was used in calculating its corresponding binding energy. The binding energy per atom B of  $\text{Li}_2$  (0.392 eV) is 72% of the experimental value (0.546 eV) indicating the reliability of the computational method.

The equilibrium interatomic distances of the clusters are collected in Table 12. The large value of  $r_e$  exhibited by  $\text{Li}_4$  might be accounted for by its geometry. For the  $\text{Li}_4$ , two different geometries are possible, namely square and tetrahedron. Clearly the square has only 4 bonds while the tetrahedron has 6 bonds. According to Fukano and Wayman (7), the tetrahedron would be more stable than the square. Calculations are in progress to test this hypothesis.

In addition, we note that the  $\text{Li}_{13}$  clusters also attained on equilibrium interatomic distance (3.23 Å) which is larger than that of the bulk crystal (3.03 Å). Again this might be accounted for by their differences in geometry. First of all, the bulk crystal is known to have a body centre cubic (b.c.c.) structure while both  $\text{Li}_{13}$  clusters ( $I_h$  and  $O_h$ ) have a face centre cubic (f.c.c.) structure. Thus if a lithium cluster does exist in f.c.c. form, the magnitude of  $r_e$  (3.23 Å) for  $\text{Li}_{13}$  clusters may be understood. In fact, a gradual transformation from b.c.c. to f.c.c. structure does exist for lithium crystal at temperatures below  $-200^\circ\text{C}$  (8,9). Moreover, during such a phase transition, both volume expansion (about 2.8%) and atomic radius increase occurred. Thus the resultant f.c.c. crystal possesses a larger lattice constant, and consequently a larger equilibrium interatomic distance than the b.c.c. crystal does. The effective temperature in our calculation is  $0^\circ\text{K}$ . Thus the magnitude of  $r_e$  for our  $\text{Li}_{13}$  clusters would be larger than that for the bulk crystal.

The total energy per atom  $E_T'$  of each cluster is lower than the energy of a single separated lithium atom (Table 12). In other words, all the

clusters are more stable than a separated atom. Moreover, the clusters become more and more stable as they grow in size, except for  $\text{Li}_3$ . Both  $E_T^I$  and  $B$  show that  $\text{Li}_3$  is less stable than  $\text{Li}_2$ . The reason for this is not known.

The icosahedral cluster possesses larger  $B$  and lower  $E_T^I$  values than the cubooctahedral cluster. Thus the former is more stable than the latter. Moreover, the shape of the curves in Figs. 5 and 6 demonstrate that at equilibrium, the icosahedron is more stable than the cubooctahedron. Admittedly the small difference (about 0.1%) between the total energies of these 2 clusters warns us to accept such a conclusion with care. A similar conclusion has been reached by Allpress and Sanders in their theoretical calculations concerning the structure and stability of small clusters of atoms (10).

The binding energy per atom  $B$  is believed to be of a good index of chemical behavior. For the bulk crystal  $B$  was obtained from a Self-Consistent Augmented-Plane-Wave (APW) calculation done by Rudge (11). The APW and our  $X\alpha$ -Scattered Wave methods are basically similar to each other. The principal difference resides in the particular choice of the representation and basis set used in the expansion of the composite wave functions. In other words, when equivalent sets of parameters are chosen, these two methods are expected to yield practically identical results. The set of parameters ( $\alpha = 2/3$ ,  $\alpha/\alpha_E = 3/2$ ,  $\alpha_E$  is an arbitrary factor multiplying Slater's exchange in the total energy expression) chosen by Rudge was more or less equivalent to ours. Hence, we believe that Rudge's results can be used to compare our results to those obtained for bulk lithium. The comparison between  $B$  of the icosahedron and that obtained by Rudge for the bulk crystal showed that the 13-atom cluster (about  $10 \text{ \AA}$ ) has attained about 85% of the bulk crystal value. This result is of great importance for it reveals that a cluster of size about  $10 \text{ \AA}$  might behave

chemically in a way very similar to that of the bulk crystal. Even the simple cubic  $\text{Li}_8$  cluster has a binding energy per atom equal to approximately 68% of the theoretical value for bulk crystalline lithium (see Table 12). These results may help to understand why, in the absence of support interactions, clusters of platinum small enough to be in the supercages of a Y zeolite, behave catalytically like larger crystallites of platinum for the hydrogenation of ethylene (12).

It has originally been shown in Ref. 1 that the SCF- $X\alpha$ -SW method facilitates the computation of molecular-orbital wave-functions and densities, thus permitting the visual display (via computer-generated contour maps) of electronic charge distributions and chemical bonds. This facility is particularly valuable for analyzing the fundamental nature of interfacial (e.g. adsorbate-substrate) chemical bonds. In Fig. 13, for example, we display a contour map of the valence electronic charge distribution for a  $\text{Li}_8$  cluster, computed at the equilibrium internuclear distance shown in Table 12 and plotted in the plane of the cube face. It is especially interesting to note the significant amount of charge density located between the nuclei and directed toward the center of the cube face (indicated in Fig. 13 by the contours labeled 10). The pile-up of charge in the cube face is important, not only because it relates to the bonding and stability of the  $\text{Li}_8$  cluster, but also because it may be relevant to the type of charge overlap which is essential to the reactive chemisorption or absorption of hydrogen by small lithium particles.

At the time of writing of this manuscript, calculations are in progress on Ni, Cu, Pt, and Pd aggregates. Preliminary results for small Cu and Ni clusters indicate the importance of 3d-4s hybridization and spin polarization in determining the most stable electron configuration and geometry of the system (12). Calculations are also in progress on models for chemisorption and absorption of hydrogen by these metal aggregates. For

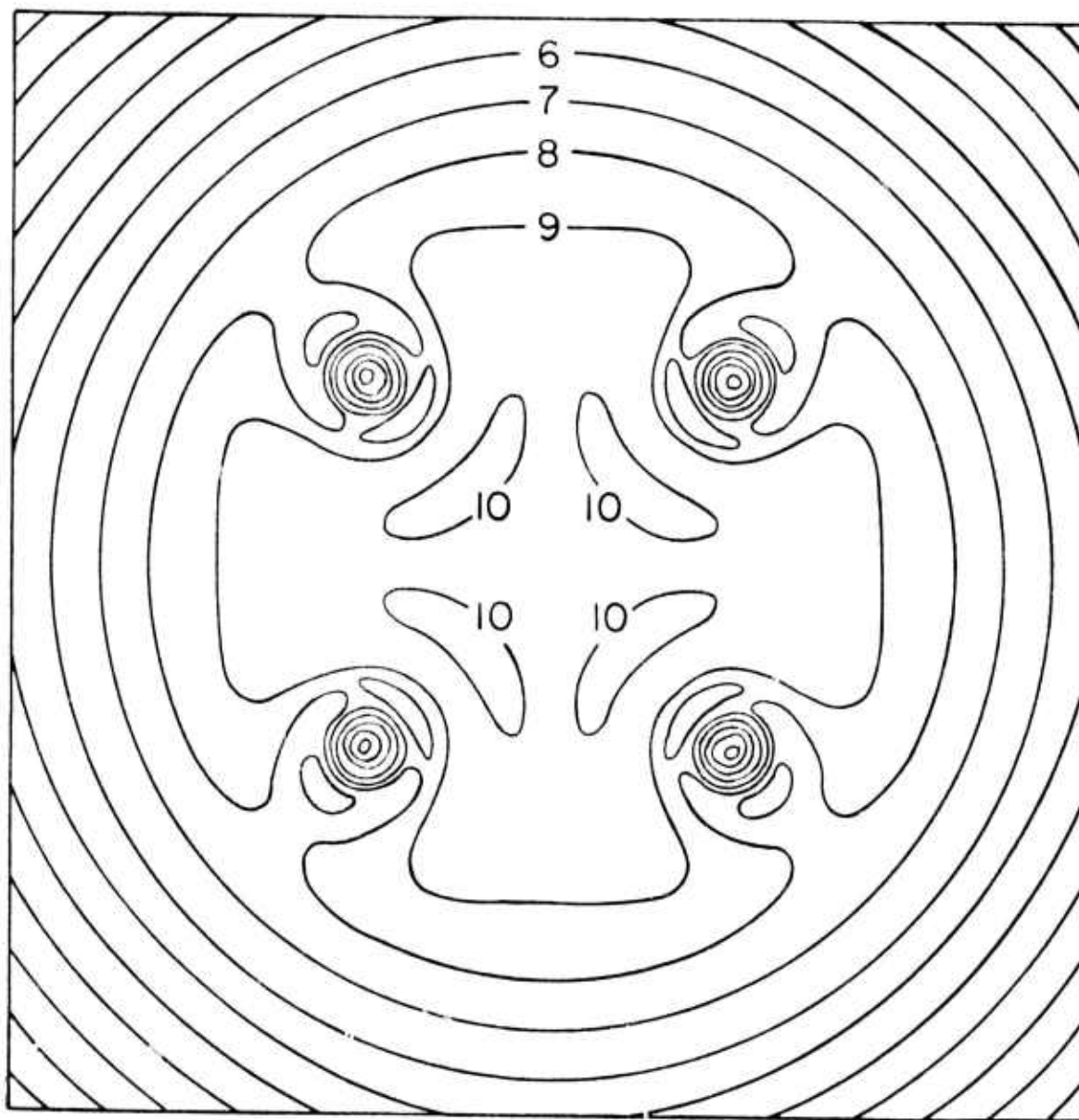


Figure 13. Contour map of valence electronic charge density of  $\text{Li}_8$  in the plane of a cube face, calculated by the SCF-X $\alpha$ -SW method. Density of contour nearest each  $\text{Li}_3$  nucleus is  $0.092 \text{ e/a}_0^3$ ; density of contour 10 is  $0.012 \text{ e/a}_0^3$ ; density of contour 8 is  $0.03 \text{ e/a}_0^3$ .

example, in modeling the absorption of hydrogen atoms by palladium particles, SCF-X $\alpha$  Scattered-Wave calculations are initially being carried out for single H atoms in small Pd clusters (e.g. Pd<sub>4</sub>, Pd<sub>8</sub>, Pd<sub>13</sub>, etc.) as functions of the position of the H atom and of the cluster size and geometry.

In addition to investigating the electronic structures of unsupported metal clusters as described above, we are also attempting to establish the effects, if any, of supporting materials such as silica and alumina on the structures, bonding, and stabilities of the clusters. For example, in considering a Ni cluster supported in silica, it is possible to determine whether the surrounding matrix functions in a largely inert fashion or whether there are specific metal-support bonding interactions that can enhance catalytic activity and specificity. This can be implemented by directly including silicate complexes as components of the Ni cluster and then comparing the electronic structure and chemisorption capacity of this composite system with the corresponding results calculated for a pure Ni aggregate.

Small alloyed metal particles in the form of supported "bimetallic clusters" are becoming increasingly important in heterogeneous catalysis (14). With the SCF-X $\alpha$  Scattered-Wave method, it is straightforward to model the effects of alloying on the electronic structures and magnetic properties (e.g., charge transfer and spin polarization) of metal aggregates, by systematically substituting "impurity" atoms in the aggregate (e.g., Ni in Cu<sub>8</sub> or Cu<sub>13</sub>) and then carrying out the electronic structure calculations to self-consistency.

This work was supported by ARPA Grant No DAH C15-73-G15, NSF Grant GK 17451X, the Center for Materials Research at Stanford University and the Center for Materials Science and Engineering at the Massachusetts Institute of Technology. One of us (JBD) acknowledges an IBM postdoctoral Fellowship.

### C. References

1. Johnson, K. H., Adv. Quantum Chem. 7, 143 (1973).
2. Slater, J. C., Adv. Quantum Chem. 6, 1 (1972).
3. Slater, J. C. and Johnson, K. H., Phy. Rev. B, 5, 844 (1972).
4. Pople, J. A. and Beveridge, D. L., Approximate Molecular Orbital Theory, pp. 41-56, McGraw Hill (1970).
5. Schwarz, K., Phy. Rev. B, 5, 2466 (1972).
6. Das, G. and Wahl, A., J. Chem. Phys. 44, 87 (1966).
7. Fukano, Y. and Wayman, C., J. Applied Phys. 40, 1656 (1969).
8. Barrett, C. S. and Trautz, O. R., Am. Instit. Min. Met. Eng. Metals 15, 2346 (1948).
9. Barrett, C. S., Phys. Rev. (2) 72, 245 (1947).
10. Allpress, J. and Sanders, J., Aust. J. Phys. 23, 23 (1970).
11. Rudge, W., Phy. Rev. 181, 1024, 1033 (1969).
12. Dalla Betta, R. A. and Boudart, M., Proceedings of the Fifth Intern. Congress Catalysis, J. W. Hightower, Ed., North Holland Publ. Co., Amsterdam 1973, p. 1329.
13. Johnson, K. H., Diamond, J. B., Messmer, R. P., and Knudson, S. K. (unpublished).
14. Sinfelt, J. H., J. Catal. 29, 308 (1973).



**VII. DEVELOPMENT OF ELEVATED TEMPERATURES  
ELECTROCRYSTALLIZATION TECHNIQUES**

**I. V. Zubeck**

**Research Metallurgist, Center  
for Materials Research**

**P. A. Pettit**

**Chemical Technician, Center  
for Materials Research**

**U. Cohen**

**Research Assistant, Department of  
Materials Science and Engineering**

**R. C. DeMattei**

**Research Associate, Center  
for Materials Research**

**R. S. Feigelson**

**Director, Crystal Technology  
Center for Materials Research**

**and**

**R. A. Huggins**

**Professor of Materials Science  
and Engineering**

## A. Introduction

The electrochemical synthesis program was initiated to develop the facilities, techniques and understanding necessary for the preparation of a variety of materials by controlled electrolysis of molten salt systems at elevated temperatures. The potential advantages of the electrocrystallization technique are numerous. A broad range of unusual materials may be synthesized in this way. The relatively low temperature at which this type of synthesis can be accomplished (generally 500 - 100°C) can also be advantageous, especially in the case of materials with very high melting points, materials which do not melt congruently, and those in which the vapor pressure of one of the components is high.

The technique can be operated isothermally with the deposition parameters controlled electrically. This provides the opportunity for great precision and reproducibility in both measurements and the control of process parameters, and represents a substantial advantage over normal high temperature crystal growth, where thermal parameters are dominant. In addition, one has the possibility of producing both uniform and reproducible stoichiometry.

A very large fraction of the work done in this area to date has centered about the exploratory use of this method for the synthesis of various compounds, primarily of the transition elements. Essentially, no previous effort has gone into the development of sufficiently sophisticated understanding and technology for the control of the growth morphology necessary for the production of useful bulk samples, including single crystals, of a wide range of materials. In order to do this, however, it is necessary to understand how to produce and maintain the pertinent thermodynamic and kinetic conditions at the growth interface during the electrocrystallization process. It is in this direction that the major emphasis of this program is oriented.

In addition, attention is being given to the development of the electrochemical conditions necessary for the production of a group of specific materials of special interest. These include intermetallic

niobium compounds with high superconductive transition temperatures, several high melting point boride compounds with either unusual hardness or good electron emissivities, and other materials of interest because of their potential technological use as optical materials or as mixed conductors in new types of battery systems.

The body of this section consists of the individual research reports of the investigators currently working in the areas of boride synthesis, niobium intermetallic synthesis, and continuous growth techniques.

## B. Investigation of the $\text{LaB}_6$ System

I. V. Zubeck and P. A. Pettit

### 1. Introduction

Activities of the past twelve months have led to significant advances in the understanding of electrolytic crystal growth, and of the  $\text{LaB}_6$  system in particular. The  $\text{MB}_6$  system (where M is a lanthanide or an alkaline earth metal, and B = Boron) was chosen as a pilot system for development of electrolytic crystal growth techniques. The hexaborides have a cubic tunnel structure in which the central ion is free to move (Fig. 1) and can be present over a wide stoichiometry range. This also makes them of interest as potential electrode materials for solid state batteries. The  $\text{MB}_6$  can be a metal or a semiconductor, depending on the valence of the central ion. The compounds possess a hardness approaching that of diamond and melting points in excess of  $2000^\circ\text{C}$ .  $\text{LaB}_6$  is currently being used as an electron emitter material in electron microscope filaments.

To the present,  $\text{LaB}_6$  for industrial use has been obtainable only by high temperature methods which make it difficult to control the morphology and physical properties. In 1929, Andrieux<sup>(1)</sup> obtained powdery deposits of  $\text{LaB}_6$  by electrolytic decomposition of molten salts at  $800^\circ\text{C}$ . The present work constitutes a reinvestigation and extension of the original work of Andrieux. Cubic crystallites of millimeter dimensions can now be routinely obtained, and the stoichiometry of the compound can be controlled by adjusting the composition of the molten salt bath. In recent months, we have documented what appear to be the controlling variables in  $\text{LaB}_6$  deposition from molten salts. We are currently engaged in refining the control of these variables to produce large single crystals.

### 2. Research Results

Activities of the first six months were concerned with a study of morphology and control of the stoichiometry of  $\text{LaB}_6$  from Andrieux-type melts. Bath failure at high operating current densities was observed. Deposition of  $\text{LaB}_6$  from a fluoride solvent was attempted.

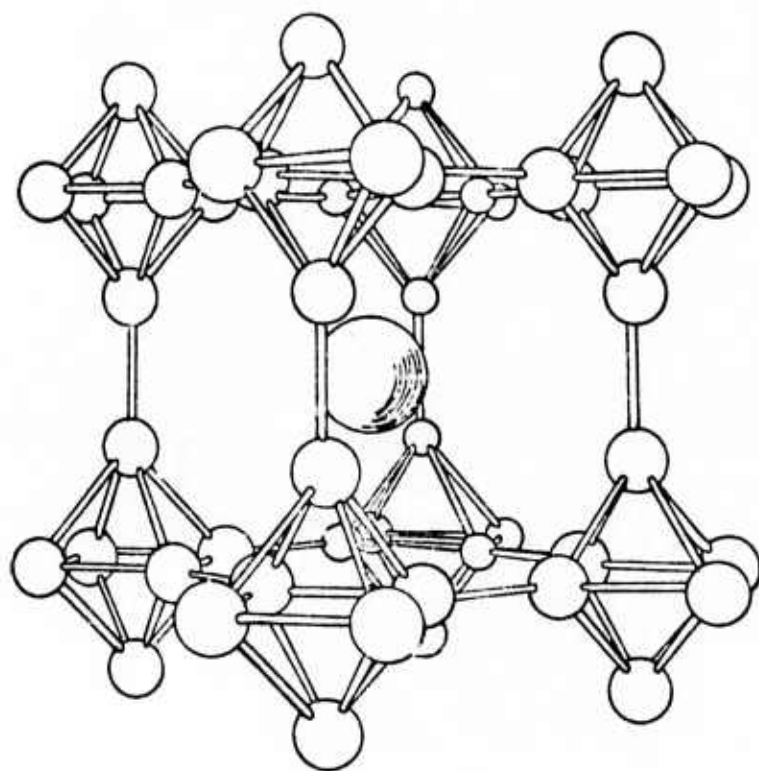


Figure 1. The cubic metal hexaboride structure. The simple three-dimensional framework of interlocked  $B_6$  octahedra is shown in perspective.

In the second half of the year, the effects of constant voltage vs. constant current mode operation on deposit morphology were investigated along with a study of secondary nucleation effects. The study of electrodeposition from molten salts can be treated as a form of solution crystal growth, even though the operating characteristics of electrolytic cells differ significantly from traditional crystallization processes.

#### A. Theory

In the electrolysis of molten salts, the passage of current through a molten salt electrolyte can be used to deposit material at electrodes. The passage of current is the result of an oxidation - reduction reaction in which electrochemically active species are reduced at the cathode and oxidized at the anode. When voltage is applied to inert (non-dissolving) electrodes of an electrolytic cell, the current behavior is as shown:

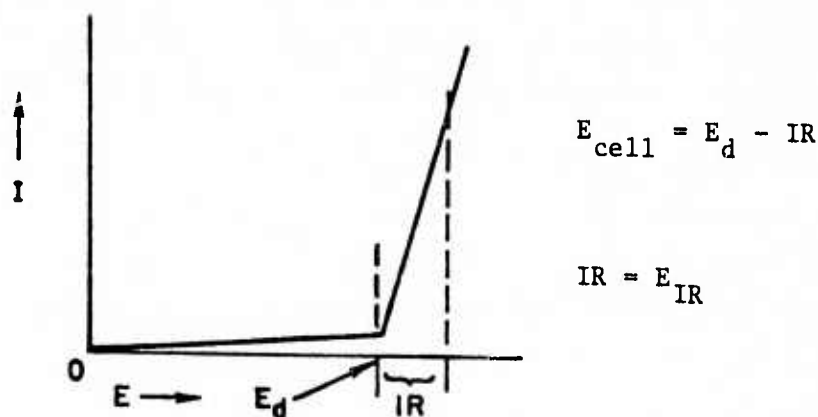


Figure 2



The applied voltage to a cell can be written as  $E_{\text{cell}} = (E_{\text{cathode}} - E_{\text{anode}}) - IR$ . The quantity  $(E_{\text{cathode}} - E_{\text{anode}})$  equals  $E_d$ , the deposition potential (the voltage required to drive the oxidation - reduction reaction) and is an equilibrium potential. As the voltage is increased above  $E_d$  and deposition begins (the cell begins to draw current) the additional voltage drop  $E_{IR} = IR$  is combined with  $E_d$  to give  $E_{\text{cell}}$ .

#### B. Experimental Apparatus

The experimental apparatus, Figure 3, for molten salt electrolysis consists essentially of a crucible containing molten salts, an anode, a cathode, a power supply and an ammeter and voltmeter. A thermocouple is placed in the vicinity of the crucible. The electrolytic cell is operated at  $500^\circ - 1000^\circ\text{C}$  under a helium atmosphere inside a vacuum tight inconel vessel, which is embedded in a furnace. The system is sealed with a flange containing quick connect fittings through which electrodes, a He inlet (which also serves as bubbler-stirrer), and a thermocouple may be raised and lowered. The flange is also equipped with a source of illuminated and viewing port which allow the operator to see inside as he adjusts the position of the electrodes. A cathode tower allows changing of the cathode during a run without having to cool down the furnace or allowing the entry of air into the system. Cooling coils on the flange and upper section of the inconel vessel protect the fittings. Electrolysis is usually carried out in Ni crucibles with gold wire or foil electrodes coupled to Ni rods.

#### C. Experimental Procedure

The composition of the basic Andrieux bath, which deposits stoichiometric material ( $\text{La}_{1.0}\text{B}_6$ ) is seen in Table I. The decomposition potential  $E_d$  (deposition potential for  $\text{LaB}_6$ ) for the above bath at  $800^\circ\text{C}$  using inert Au electrodes is  $-1.85\text{ V}$ . Current flowing in the cell is regulated by adjusting the cell voltage in the region of the IR drop of the cell.  $\text{LaB}_6$  deposition is generally carried out in the range  $-1.86$  to  $-2.0\text{ V}$ . The cell reaction is the following:

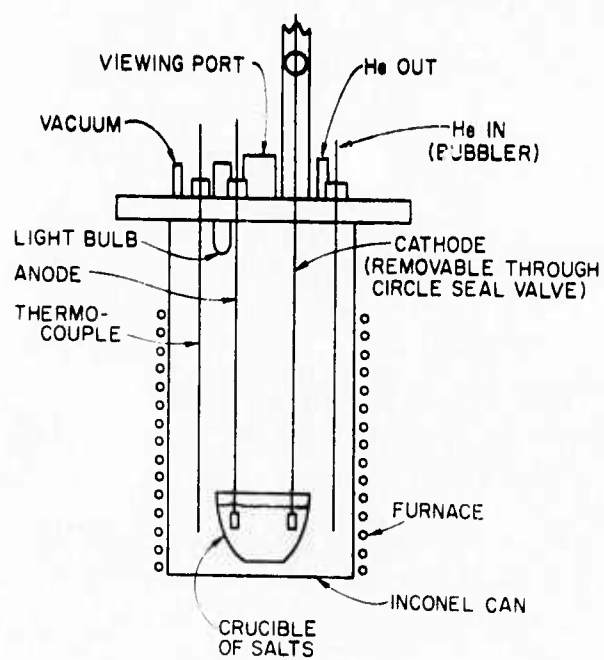
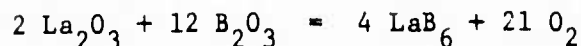
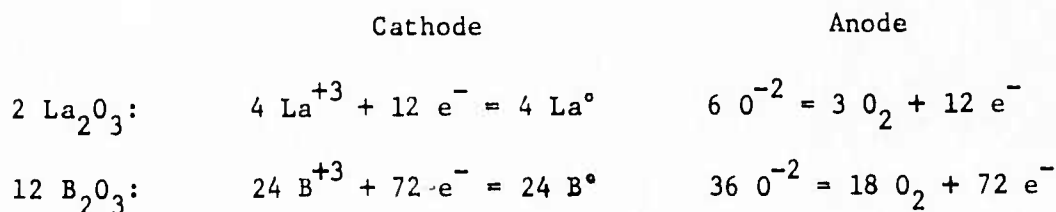


Figure 3. Schematic of Electrolysis Apparatus

Total reaction:



Corresponding half reactions:



### 1. Stoichiometry

The effects of bath composition on the stoichiometry of the deposited material was investigated. Baths containing 0.1, 0.5, 1.0, 2.2, and 4.0 mole %  $\text{La}_2\text{O}_3$  were electrolyzed. Due to their excessively high melting points, baths containing more than 4.0 mole %  $\text{La}_2\text{O}_3$  were not investigated. The melting point, deposition potential, and a current - voltage plot were recorded for each bath. Quantitative analysis was performed on the samples using an electron microprobe, and x-ray techniques were used to check for changes in lattice parameter with composition.

Electron microprobe analysis of samples grown from baths containing varying amounts of  $\text{La}_2\text{O}_3$  gave the results shown in Table II. Due to the low atomic number of boron, the accuracy of the determination is highly dependent upon the type of standard used, the orientation of the sample with respect to the detector, etc. Samples grown from the 1.0 - 4.0 mole %  $\text{La}_2\text{O}_3$  baths were magenta colored metallic cubes. The material grown from the 0.5 %  $\text{La}_2\text{O}_3$  bath was still cubic, though of a deeper blue metallic luster. The material grown from the 0.1 %  $\text{La}_2\text{O}_3$  bath was a mixture of cubic and rectangular crystals of a deep violet color. Voltage versus current data showed the effects of  $\text{La}_2\text{O}_3$  content and operating temperature on the decomposition potential of the bath to be negligible. Analysis of x-ray data showed no change in lattice parameter with stoichiometry.

## 2. Morphology

A series of experiments was run to study the effects of current density (deposition rate) on crystal morphology. Cathodes, 0.020 in in diameter, were inserted into the melt to point of contact, and the electrolysis voltage was set at values corresponding to initial currents of 1.0, 2.0, 3.0, 4.0, 5.5, 10.0, and 13.0 mA. Electrolysis was allowed to proceed as the current was monitored, until the current versus time reached a steady-state value (almost immediately for the low current sample, 20 - 30 minutes for the 7.0 and 10.0 mA samples).

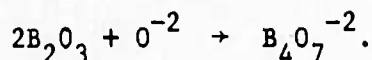
Moderate and low initial currents yielded cubic  $\text{LaB}_6$  crystals at the cathode. Higher currents produced distorted cubes with one prominent corner, while the highest initial currents produced dendrites of roughly triangular cross section.

Cubic material was obtained at and below initial currents of 1.0 to 3.0 mA (current densities 30 to 90  $\text{mA}/\text{cm}^2$ ), which remained essentially constant during the run. The material obtained at an initial current of 4.0 mA (current density 100  $\text{mA}/\text{cm}^2$ ) was in the form of distorted cubes in which one corner was more acute than cubic (tending toward dendritic behavior). Starting with an initial current of 5.5 mA or greater (current densities  $> 150 \text{ mA}/\text{cm}^2$ ) the current did not remain constant, but increased rapidly during a run, the amount of the increase being greater, the greater the initial current. Under these conditions, dendrites of roughly triangular cross section, whose length/width ratio increased with initial current, were grown. Powdery finger-like dendrites obtained at an initial current of 13 mA indicated that the useful range of operation had been extended.

## 3. Bath Failure due to High Currents

While studying crystallite morphology, it was noticed that baths subjected repeatedly to high current densities failed. After several repeated runs of dendrite generation (0.020 in Au wire cathode to point of contact,  $\sim 10 \text{ mA}$ ,  $> 150 \text{ mA}/\text{cm}^2$ ) no cathode deposit could be produced. The condition could not be reversed.

Senderoff and Mellors<sup>(2)</sup>, in electrodepositing  $\text{ZrB}_2$  from a bath composed of  $\text{LiF}$ ,  $\text{NaF}$ ,  $\text{KF}$ , and  $\text{ZrF}_2 + \text{B}_2\text{O}_3$ , also reported bath failure, which they correlated with the O/B ratio of their melts. Their analyses showed that when the O/B ratio of the bath exceeded 1.75, the bath failed, depositing only powder of  $\text{ZrB}_2$  and  $\text{ZrO}_2$ . In selected cases, when enough  $\text{B}_2\text{O}_3$  was added to an electrolysis bath to reduce the O/B ratio to 1.5, the cathode product would again be coherent  $\text{ZrB}_2$ . They believed the mechanism to be as follows: as the system is electrolyzed and boron is removed from the melt, the O/B ratio increases above 1.5 (that of  $\text{B}_2\text{O}_3$ ) and the following reaction occurs:



$\text{B}_2\text{O}_3$  can act as a getter for  $\text{O}^{-2}$  ions and several complex ions containing boron and oxygen are known. K. E. Johnson<sup>(3)</sup> prepared a series of electrode potentials (vs.  $\text{Cl}_2$  and  $\text{F}_2$  reference electrodes) for the reduction of  $\text{B}_2\text{O}_3$ ,  $\text{B}_2\text{O}_4^{-2}$ ,  $\text{B}_4\text{O}_7^{-2}$ , and  $\text{B}_2\text{O}_5^{-4}$ . In the presence of  $\text{O}_2$ ,  $\text{B}_2\text{O}_3$  is easily reduced at a cathode to one of the above complex oxyanions.

In the present experimental system, a Au anode of small surface area resulted in the dissolution of the anode produce ( $\text{O}_2$ ) in the bath. The excess  $\text{O}_2$  might then combine with  $\text{B}_2\text{O}_3$ , forming one of the complex ions. The passage of current without deposition of a cathode product indicates the operation of a cyclic oxidation - reduction process involving  $\text{B}_2\text{O}_3$  and its complex oxyanions. The presence of oxide compounds,  $\text{La}_2\text{O}_3$  and  $\text{Li}_2\text{O}$ , in the bath compounded the problem.

The current densities which produced bath failure were too high to be useful for good crystal growth. The Andrieux bath could be electrolyzed to depletion at moderate current densities. It was, therefore, decided that excessively high current densities should be avoided, and that further investigation of bath failure at high currents was beyond the current scope of interest.

#### 4. Constant Voltage vs. Constant Current Operation

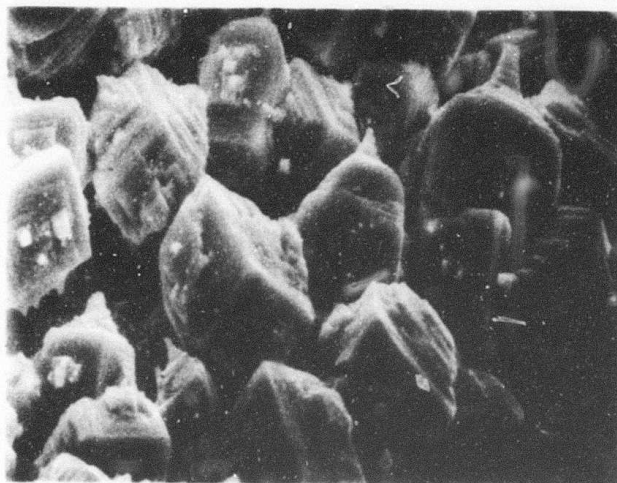
The effect of maintainin, constant voltage versus constant current on both cell operation and resulting quality of electrochemical depositions of  $\text{LaB}_6$  was investigated. All samples produced were studied with the aid of a scanning electron microscope. Using a constant voltage power supply, samples were run at selected voltages for time periods in the range of 15 min. to 4 hr., while monitoring variations as a function of current and time. In a second series of constant voltage mode experiments, the voltage setting was increased in small increments over a period of five days according to a prearranged schedule, while monitoring the current and voltage as a function of time along with the current efficiency.

The above experiments were repeated using a constant current power supply. Samples were run at selected constant currents for 15 min., 1 hr., and 4.0 hr. Samples were then grown in small increments over a period of days.

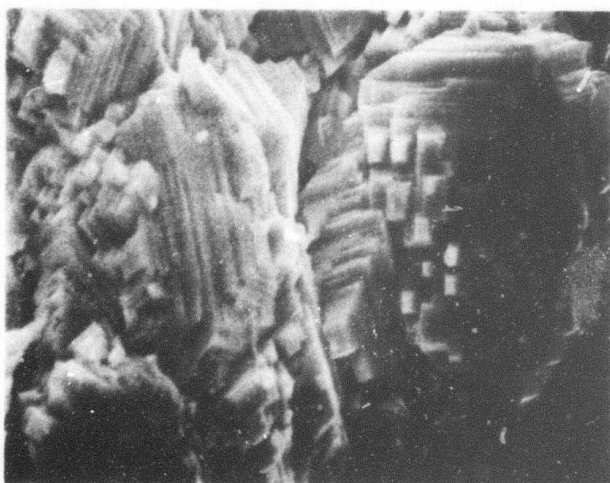
Table III contains a summary of voltage-time data for samples run under constant voltage conditions. The deposits which resulted, consisted of clusters of cubic crystals, with the crystal size increasing with voltage. At moderate deposition voltages, terraces are formed on the cube faces. The terraces (evidence of an unstable growth interface) became more pronounced with increasing voltage, Figure 4 a,b.

Increasing the cell voltage in small increments manually over a period of days proved an unsatisfactory technique. The cell current, sensitive to perturbations in voltage, often rose rapidly to inappropriately high levels and had to be decreased manually by lowering the applied cell voltage. Other samples were maintained at a constant voltage for a long period of time (several days) after an initial increase in voltage. The applied cell voltage was never lowered in these experiments.

Those crystals not subjected to a decrease in operating voltage had sharp corners and smooth faces, and also yielded the highest current efficiency (100%), Figure 5 a,b. Two samples which had experienced



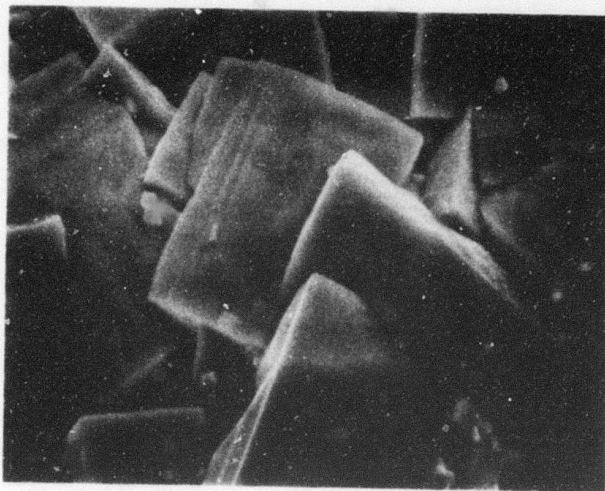
a) Applied voltage: 1.95 volts  
Time: 15 minutes



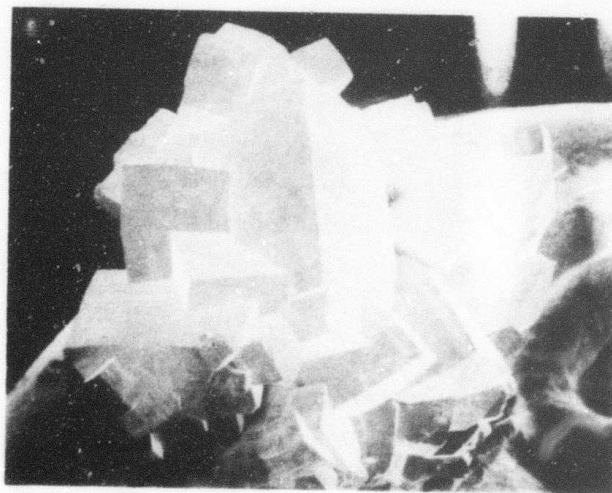
b) Applied voltage: 1.90 volts  
Time: 30 minutes

Figure 4. Examples of terraces formed on growing cube faces. 2000X.





a) Applied voltage: 1.95 volts  
Time: 30 minutes  
2000X



b) Applied voltage: 1.85 to 1.93 volts  
Time: 355 hours  
20X

Figure 5. Examples of crystals grown with applied voltages which were not allowed to decrease.

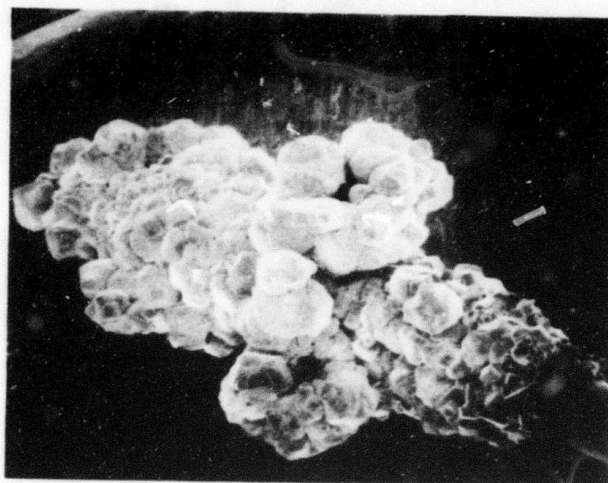
decreases in voltage during deposition had degraded surfaces showing rounded edges composed of numerous growth or solution steps, Figure 6 a,b. Samples grown in this manner had low current efficiencies (66% and 20%). The deposit undergoing the greatest number of voltage decreases showed the more serious surface degradation and had the lower current efficiency.

Table III also contains the current time data obtained from constant current experiments. The deposits again consisted of clusters of cubic crystals whose dimensions increased with current and time as described. No deposit at all was obtained at or below 0.5 mA. Such small currents lie within the domain of the residual current of the cell and require a voltage below  $E_d$ . Currents greater than or equal to 1.0 mA required voltages greater than  $E_d$  (at least initially). In all cases, the cell voltage decreased with time and the crystalline product was, with one exception, heavily etched, with rounded corners and cubic pits (Figure 7 a,b). In one case, the cell voltage decreased to below  $E_d$  and the cell ceased to deposit  $\text{LaB}_6$ .

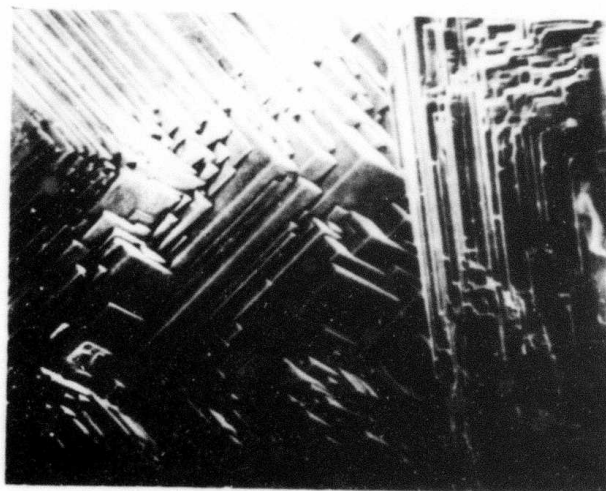
Operating in constant current mode, the current was increased from 0.5 mA to 9.0 mA in small increments over a period of five days. The cell voltage never rose above ~1.79 V, and x-ray analysis showed the cathode product to be  $\text{LaBO}_3$ . The behavior of the electrolysis cell as well as the condition of the cathode product show the necessity of operating in a constant voltage mode if good crystal growth is to be obtained.

As deposition proceeds, the surface area of the cathode increases, reducing the overall resistance of the cell. In constant current mode, decreasing  $R$  caused a decrease in  $E_{\text{cell}}$  through  $E_{\text{cell}} = E_d - IR$ . The use of a small cathode (as here) magnified the effect. Deposition caused a large percentage increase in cathode surface area and a correspondingly large decrease in  $R$ .

To summarize, when  $E_{\text{cell}}$  was allowed to decrease, the individual crystallites making up the cathode product always showed rounded corners, cubic pits, etc. In those cases in which material was grown at constant



25X



500X

Figure 6. Morphology of crystallites grown under conditions where incremental decreases in voltage of between 0.01 - 0.03 V were experienced.



a) Current: 1 ma  
Time: 4 hours



b) Current: 1 ma  
Time: 1 hour

Figure 7. Examples of crystals grown in constant current mode. 2000X.

or increasing voltages, the deposited material showed sharp corners and edges, and smooth surfaces. Inappropriately high voltages (deposition rates) resulted in crystallites with cubic morphology, but containing numerous terraces or dendrites.

Morphological stability in the electrochemical crystal growth process depends on the deposition rate, in much the same way that it does in standard solution or flux crystal growth. In the former process the deposition rate can be controlled by changes in current induced by variations in  $E_{IR}$ . In the case of solution growth, the driving force for crystallization is the supersaturation of the solution and the deposition rate can be varied by adjusting evaporation rates or solution temperature. Growth of good single crystals by solution techniques is achieved by use of a constant or smoothly increasing (as surface area increases) deposition rate, the ideal case being a constant deposition rate per unit area (current density in electrochemical crystal growth).

Application of the fundamental theories of nucleation and growth as they pertain to solution growth, while taking into account the operating characteristics of electrolytic cells, should allow single crystals of appreciable size to be obtained by electrolytic decomposition of molten salts.

##### 5. Primary and Secondary Nucleation

The cathode product obtained in the constant voltage mode at moderate current densities consisted of clusters of cubic crystallites. It was unclear whether these were cubes of identical dimensions deposited in concentric layers (secondary nucleation) surrounding the cathode, or whether the crystallites originally nucleated simply continued to grow larger with time, crowding out smaller ones as they grew. A sample was mounted and cross sectioned. The deposit shown in Figure 8 exhibits both types of behavior. Some of the original crystallites nucleated on the Au wire substrate (primary nucleation) were found to have grown to the deposit surface. In addition, some secondary nucleation had taken place on the surfaces of already existing crystallites. Deposits

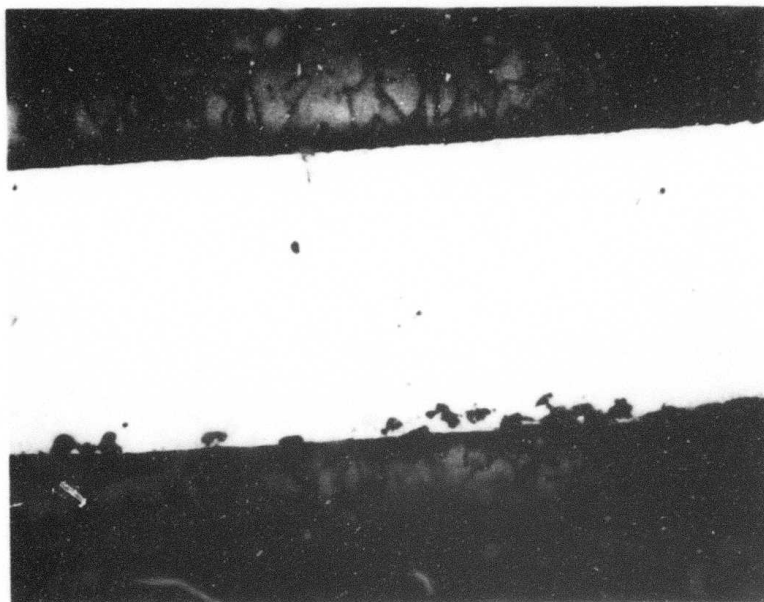


Figure 8. Cross section of a  $\text{LaB}_6$  deposit on a 0.020 inch diameter gold wire.

obtained by increasing the voltage (in constant voltage mode) in small increments, showed a minimum amount of secondary nucleation. This suggests that regulation of the deposition rate can minimize secondary nucleation.

### 3. Continuing Research and Future Plans

The results of the constant voltage vs. constant current mode runs strongly suggested that electrolytic crystal growth can be satisfactorily treated as a form of solution growth. That is, the deposition rate must be closely regulated and increased as the crystallites increase in size. A constant local growth rate should be maintained. To this end, a ramp generator is being built, which will increase applied cell voltage in small increments over a preset period of time. This instrument will be used to determine growth rates appropriate to given initial conditions and should minimize secondary nucleation while promoting the growth of larger crystals. This instrument will also be used for nucleation studies. An additional aid to control deposition rates will be the installation of better temperature regulators for the growth furnaces.

The objectives for the coming year include understanding of nucleation characteristics and refinement of the control of growth parameters, taking into account the operating characteristics of electrolytic cells, in order to grow larger single crystals.



### References

- (1) L. Andrieux, Ann. de. Chim. 12, 424, (1929).
- (2) G. W. Mellors, S. Senderoff, J. Electrochem. Soc. 118, 220 (1971).
- (3) K. E. Johnson, Proceedings of the Third International Symposium on High Temperature Technology, Pacific Grove, California, September, 1971, Butterworths, London.

TABLE I

COMPOSITION OF THE MOLTEN SALT BATH FOR  $\text{LaB}_6$  DEPOSITION

	Mole %	Moles/100 gm charge	gms/100 gm charge
$\text{La}_2\text{O}_3$	2.2	.046	15.2
$\text{B}_2\text{O}_3$	33.4	.698	48.6
$\text{Li}_2\text{O}$	31.2	.650	19.5
$\text{LiF}$	33.1	.690	18.1
			97.4 gm

TABLE II

Mole % $\text{La}_2\text{O}_3$	Deposition Temperature	-Probe Analysis	
		No. 1	No. 2
0.1 %	~700°C		$\text{La}_{.672}\text{B}_6$
0.5 %	700°C	$\text{La}_{.858}\text{B}_6$	
1.0 %	700°C	$\text{La}_{.864}\text{B}_6$	$\text{La}_{.822}\text{B}_6$
2.2 %	700°C	$\text{La}_{.867}\text{B}_6$	$\text{La}_{.834}\text{B}_6$
4.0 %	700°C	$\text{La}_{.867}\text{B}_6$	$\text{La}_{.834}\text{B}_6$
8.0 %	800°C		
16.0	> 1000°C		

TABLE III

## CONSTANT VOLTAGE SAMPLES

Constant Voltage	Time	Sample Number	Deposit Morphology and Maximum Crystallite Size
1.60	15 min	13 - 1	Cubic Deposit (2.5-3 $\mu$ )
1.80	15 min	13 - 2	Cubic Deposit (5 $\mu$ )
	1 hr	13 - 9	Isolated tubes (15 $\mu$ ); terraces
	2 hr	13 - 12	Isolated cubes (10 $\mu$ ); degraded, cubic pits
1.85	15 min	13 - 3	Cubic Deposit (8-12 $\mu$ ), cubic pits
	1 hr	13 - 11	Cubes, terraces (120 $\mu$ )
1.90	15 min	13 - 4	Cubes, terraces, (10 $\mu$ )
	30 min	13 - 7	Cubes, terraces, (12 $\mu$ )
	1 hr	13 - 8	Cubes, terraces, (15 $\mu$ )
1.95	15 min	13 - 5	Cubes, large terraces, (10 $\mu$ )
	30 min	13 - 10	Cubes, well formed inter- secting cubes, (20-25 $\mu$ )
2.0	15 min	13 - 6	Cubes, terraces, (15-25 $\mu$ )

# CONSTANT CURRENT SAMPLES

Constant Current	Time	Sample Number	Deposit Morphology and Maximum Crystallite Size
.10 mA	15 min	15 - 7	Etched Au No Deposit
	1 hr	15 - 13	Etched Au No Deposit
	4 hr	14 - 1	Etched Au No Deposit
.25 mA	15 min	15 - 6	Etched Au No Deposit
	1 hr	15 - 12	Etched Au No Deposit
	4 hr	14 - 3	Etched Au No Deposit
.50 mA	15 min	15 - 4	Etched Au No Deposit
	1 hr	15 - 11	Etched Au No Deposit
	4 hr	14 - 4	Etched Au No Deposit
1.0 mA	15 min	15 - 1	Small cubes (2.5 $\mu$ ) with cubic pits larger cubes (5.0 $\mu$ ) with cubic pits Badly etched material
	1 hr	15 - 10	
	4 hr	14 - 2	
2.0 mA	15 min	15 - 3	Cubic deposit (14 $\mu$ ) with cubic pits Cubic deposit (4 $\mu$ ) isolated cubes with pits Isolated cubes (5 $\mu$ ) rounded edges and cubic pits (same as below (8 - 10 $\mu$ ))
	1 hr	15 - 9	
	4 hr	15 - 14	
4.0 mA	15 min	15 - 2	Heavily nucleated cubic deposit (10 - 15 $\mu$ ) etched cubic pits Heavily nucleated cubic deposit (10 - 15 $\mu$ ) etched cubic pits Heavy nucleation cubic stacked protrusions, no pits (20 - 25 $\mu$ )
	1 hr	15 - 8 <sup>1</sup>	
	4 hr	15 - 15 <sup>2</sup>	

<sup>1</sup> Sample #8, V decreased steadily, 1 hr

<sup>2</sup> Sample #14, V decreased, but held steady for 2 of 4 hr

### C. Electrodeposition of Niobium Alloys Superconductors from Molten Fluorides

U. Cohen

#### Introduction

The niobium intermetallic compounds  $Nb_3X$ , where X is Al, Sn, Ge, Si, or Ga, are among the best known superconductors. They exhibit the A-15 (or  $\beta$ -tungsten) structure and are extremely brittle. Conventional preparation by arc melting, sintering, etc. results in non-homogeneous and non-machinable products. Vapor deposition is the best method of preparation to date, but this technique suffers from many disadvantages. It is possible to coat thin films on premade simple shapes, but the uniformity of the coatings and the stoichiometry is not easily controlled. Also, the films are usually thin and can not carry a very high superconducting current.

The interface mechanisms during vapor deposition are considerably different from those during electrodeposition. In vapor deposition, molecular species, sometimes, of appreciable size, arrive at the substrate surface, and since the interface rearrangement kinetics are rather slow, defect incorporation is a strong possibility. In electrodeposition, the interface mechanism is atomistic, the exchange flux density is greater, and surface rearrangement is much easier and faster.

The electrodeposition technique offers the potential for the uniform coating of complex articles, the preparation of heavier films, and easy control of composition and structure, hence greater reproducibility.

The fluoride melts were chosen since they have been proved to yield superior coatings of niobium and other refractory metals.<sup>(1-7)</sup> The excellent bonding of the coatings is probably due to the fluxing effect of

fluoride solutions, exposing clean metallic surfaces.

The objectives of this project are:

- (a) Electrochemical investigation of the fluoride solutions of Al, Sn, Ge, Si, and Ga.
- (b) Electrochemical investigation of niobium fluoride solutions.
- (c) Electrochemical investigation of the mixed fluoride solutions of Nb-Al, Nb-Sn, Nb-Ge, Nb-Si, and Nb-Ga.
- (d) Investigation of the feasibility of the electrodeposition of the superconducting phases  $Nb_3Al$ ,  $Nb_3Sn$ ,  $Nb_3Ge$ ,  $Nb_3Si$ , and  $Nb_3Ga$ .
- (e) If successful in any of (d), morphology control and experimental parameters to improve superconducting properties will be investigated.

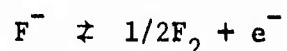
For co-deposition to occur, the two electroactive species must have electrode potentials which are not widely separated. In accordance with the Nernst equation, operating electrode potentials can be brought closer by variation of the relative concentrations of the species. A practical limit on this correction is of the order of 100 - 300 mV. A difference of more than 300 - 500 mV between the standard electrode potentials of the two species makes them unsuitable as a co-deposition couple.

Other problems of co-deposition are the relative kinetics of charge transfer of the two species, and the relative kinetics of charge transfer and coupled chemical reactions, adsorption, and catalysis. Thus, for instance, two electroactive species may match with regard to their electrode potentials, but differ greatly in their charge transfer rates, and, therefore, not be suitable as a codeposition couple. Similar problems may arise when the total reaction is controlled by either adsorption or interfacial transport processes.



### F<sup>-</sup>/F<sub>2</sub>, Au/ as a Quasi-Reference Electrode

The electrochemical investigation of the fluoride solutions requires the use of a suitable reference electrode. It was found that a gold wire can be used as an anode and simultaneously as a quasi-reference electrode. Fluorine is liberated upon the gold by the reaction



It was found that the weight loss of the Au electrode was less than 1% for anode current densities below 50 - 100 mA/cm<sup>2</sup>. Assuming that the only anode reaction is the one described and that  $p_{F_2} \approx 1$  atm, this electrode operates under standard conditions, and thus it can be used to measure decomposition potentials.

Note that for the fluorine bubbles to escape from the melt, which is under about 1 atm of pressure, the bubbles must have a pressure of slightly above 1 atm. This reference electrode was somewhat erratic and less reproducible in fluorides than in oxides. The main advantage of its use was the simplicity and ease of getting approximate results quickly. The main difficulties and disadvantages in using this electrode are:

(a) F<sub>2</sub> attacks the Ni crucible to form NiF<sub>2</sub>, which dissolves in the melt and contaminates the electrodeposits.

(b) The fluorine electrode can not readily be compartmented, since F<sub>2</sub> attacks any diaphragm which is not made of gold. This further complicates the I-V curves if the electroactive species is capable of more than one valency. Reoxidation of the species is possible at the anode. This is also a reason for lower decomposition potentials recorded for the alkali-fluorides, as the fluorine reacts directly with the alkali metal.<sup>9</sup>

(c) Sometimes anode passivation occurs for unknown reasons. This usually occurs when using high current densities. The anode surface is covered with a dark layer, probably insoluble gold fluoride.

(d) The temperature range for the use of Au as an anode is below 900°C. Otherwise rapid dissolution of the gold takes place.

(e) Inaccuracy in the determination of the decomposition potential due to extrapolation to zero current of non-linear curves of a "catalytic" type, is estimated at 50 - 100 mV.

In order to obtain absolute values, a new compartmented reference electrode  $\text{Ni/NiF}_2$  is being now designed, similar to the one developed by Jenkins and Mamantov.<sup>(19)</sup> However, their boron nitride sheath is to be replaced by a sintered nickel cup, with micron-scale porosity. This should eliminate the junction potential they reported, which prevented them from investigating temperature dependencies, as their electrode resistance did not vary linearly with temperature. A differential voltmeter is used to measure potentials with accuracy of up to  $\pm 10 \mu\text{V}$ . A new potentiostat-Galvanostat and a Universal Programmer will soon be put to use in cyclic voltammetry and chronopotentiometry measurements.

#### Materials and Experimental Procedures

All materials used in this work are of 99.9% purity or better, and are kept in a vacuum dessicator. Water is an important contaminant in fluoride baths, and the very hygroscopic KF is dried in a vacuum oven at 200°C for 48 hours. Ultimate drying was achieved by adding  $\text{KHF}_2$  to the salt mix, and heating above the decomposition temperature of  $\text{KHF}_2$ .

The equilibrium reaction



is shifted to the right under vacuum. Continuous production of HF via decomposition at a slow rate of heating also helps to maintain the shift of the reaction to the right. The salt mixture containing  $\text{KHF}_2$  is held at  $200^\circ\text{C}$  under vacuum over night, then heated at a rate of  $30 - 50^\circ\text{C}$  per hour under vacuum to  $750 - 800^\circ\text{C}$ . During that time, the excess HF and the  $\text{H}_2\text{O}$  vapors are collected in a liquid nitrogen trap. At  $750 - 800^\circ\text{C}$ , helium is admitted, and at  $850^\circ\text{C}$ , helium bubbled through the melt to drive out the rest of the dissolved HF. A very clear solution is an indication of a very dry melt. Also, when cooled, the frozen slug comes out of the Ni crucible easily if the solution is pure and dry. This technique seems to be superior to HF bubbling.

No specific analysis for impurities in the melts has been undertaken to date. Satisfactory purity, however, can be judged by melt appearance and clarity. Nevertheless, some metallic contamination from the chamber and the crucible can always be detected in the electrodeposits. Methods to avoid these are now being sought.

Grade A helium gas is used over the fluoride bath, after being purified on a Linde 13X molecular sieve in a liquid nitrogen trap, and by passing over Ti chips at  $700^\circ\text{C}$ .

A typical experimental procedure involves weighing and mixing the dry chemicals in a Ni crucible, melting and HF treating as described above. The chamber is then cooled and opened, and the crucible rapidly transferred to a vacuum dessicator. The chamber is then cleaned, and the crucible placed

back in it, and kept at 200°C under vacuum overnight. Helium is admitted and the system heated to the desired temperature. The electrodes are typically dipped into the melt to ~1 cm. depth for obtaining electrical measurements or electrolysis.

The cathode can be removed and a new cathode introduced with no need to cool down the system, unless chemical modification of the bath is required.

Typical operating parameters are:

Current density: a few mA/cm<sup>2</sup> to several A/cm<sup>2</sup>

Voltage: 0 - 4 volts

Temperature: 500 - 900°C

Solvent: KF - LiF eutectic

Cathodes: Plates and wires of Au, Nb, Ni, Pt, and Mo

Anodes: Plates and wires of Au, Nb, Al, and Ge

Period of Electrodeposition: Few minutes to several days

Analyses of deposition compositions have been obtained utilizing X-ray diffraction, X-ray fluorescence, Metallography, Electron Microprobe, and Scanning Electron Microscope techniques. Rough estimates were also made of bonding quality and morphology.

## Results and Discussion

### 1. KF Decomposition Potentials

The purpose of decomposition potential measurements of the solvent and pure KF was to evaluate the range of potentials useable for the electrodeposition from this solvent without decomposing the solvent.

An I-V curve of the solvent KF - LiF (50%, 50%, mp 492°C) is shown in Figure 1, and that of KF only, in Figure 2.

The values of the decomposition potential found for KF from these curves, are lower by about 1.0 - 1.2 volts than the theoretical values of Hamer and Malmberg.<sup>(8)</sup> These lower experimental values for alkali fluorides are explained by Delimarskii<sup>(9)</sup> as being due to insufficient separation of the electrodes, leading to a reaction between the fluorine and the alkali metal. Another reason is metal solution in the melt and resultant cathode depolarization. For comparison with other experimental and theoretical values, see Table I.

The temperature dependence of the KF decomposition potential in the eutectic KF - LiF is shown in Figure 3.

It should be noted that the present values are between the theoretical value and previously reported experimental values. The effect of eutectic complexing on the decomposition potential is small. For pure KF at 867°C, the decomposition potential was found to be -3.427V and for the eutectic at this temperature, the value is -3.405V, from Figure 3.

## 2. Niobium Fluoride Decomposition Potentials

I-V curves for  $K_2NbF_7$  in the KF - LiF eutectic solvent were taken as a function of temperature and concentration. Two steps are observed before the solvent decomposition at -3.92V, Figure 4. At 563°C and a scan rate of 33.3 mV/sec. the first wave initiates at -1.93V, and the second at -3.18V (after a correction for the IR drop of 0.20V).

Thermodynamic data and previous experimental data for the niobium fluorides are extremely scarce. Senderoff and Mellors investigated the

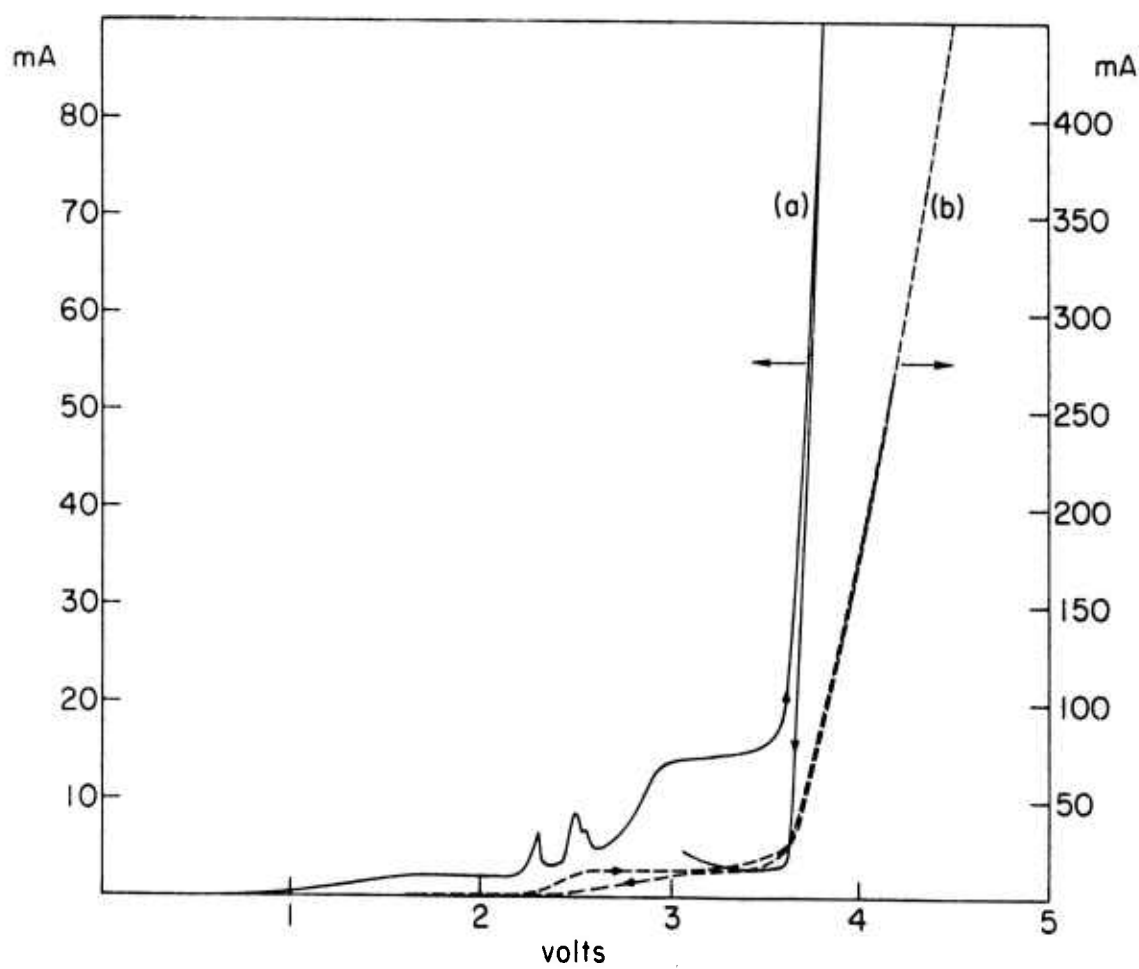


Figure 1. I-V curves of KF-LiF eutectic.  $t = 570^{\circ}\text{C}$ ;  
 $v = 33.3 \text{ mV/sec.}$ ; Au - quasi reference anode.

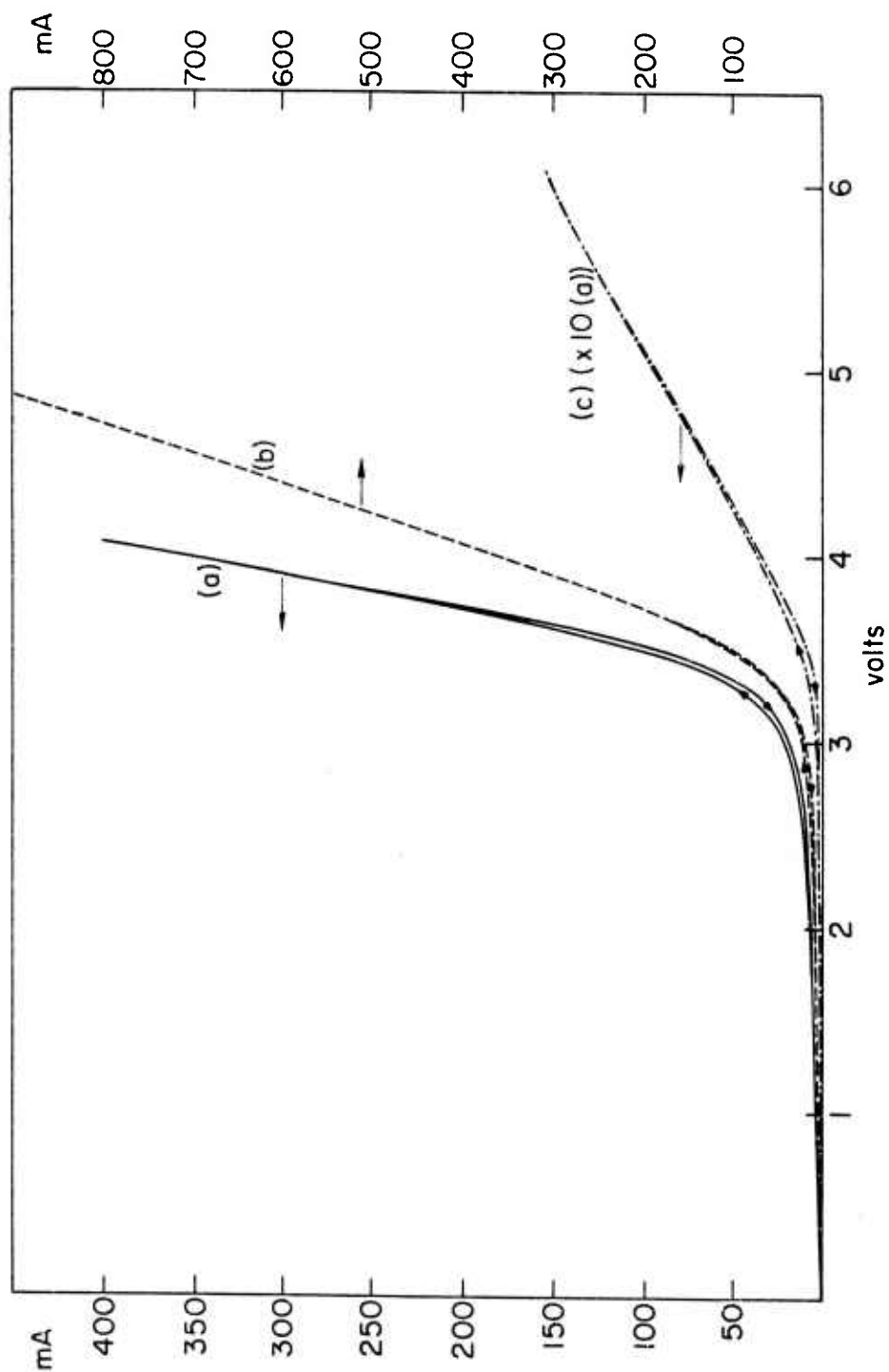


Figure 2. I-V curves of KF only.  $t = 867^{\circ}\text{C}$ ; (a)  $v = 83 \text{ mV/sec.}$ ; (b)  $v = 166 \text{ mV/sec.}$ ; (c)  $v = 830 \text{ mV/sec.}$ ; Au anode.



TABLE I

## KF Decomposition Potentials (in Volts)

Salt	Temperature °C	Theoretical Value after [8] (pure salts)	Present Work	Other Experimental Values	Reference
KF	600	4.01			
	700	4.80		3.29	13
	800	4.67			
	900	4.53	3.43 (at 867°C)	2.89 (at mp 857°C)	4
	1000	4.35		2.59	13
KF	600		3.75		
in KF-LiF eutectic	700		3.60		
	800		3.49		
	900		3.38		

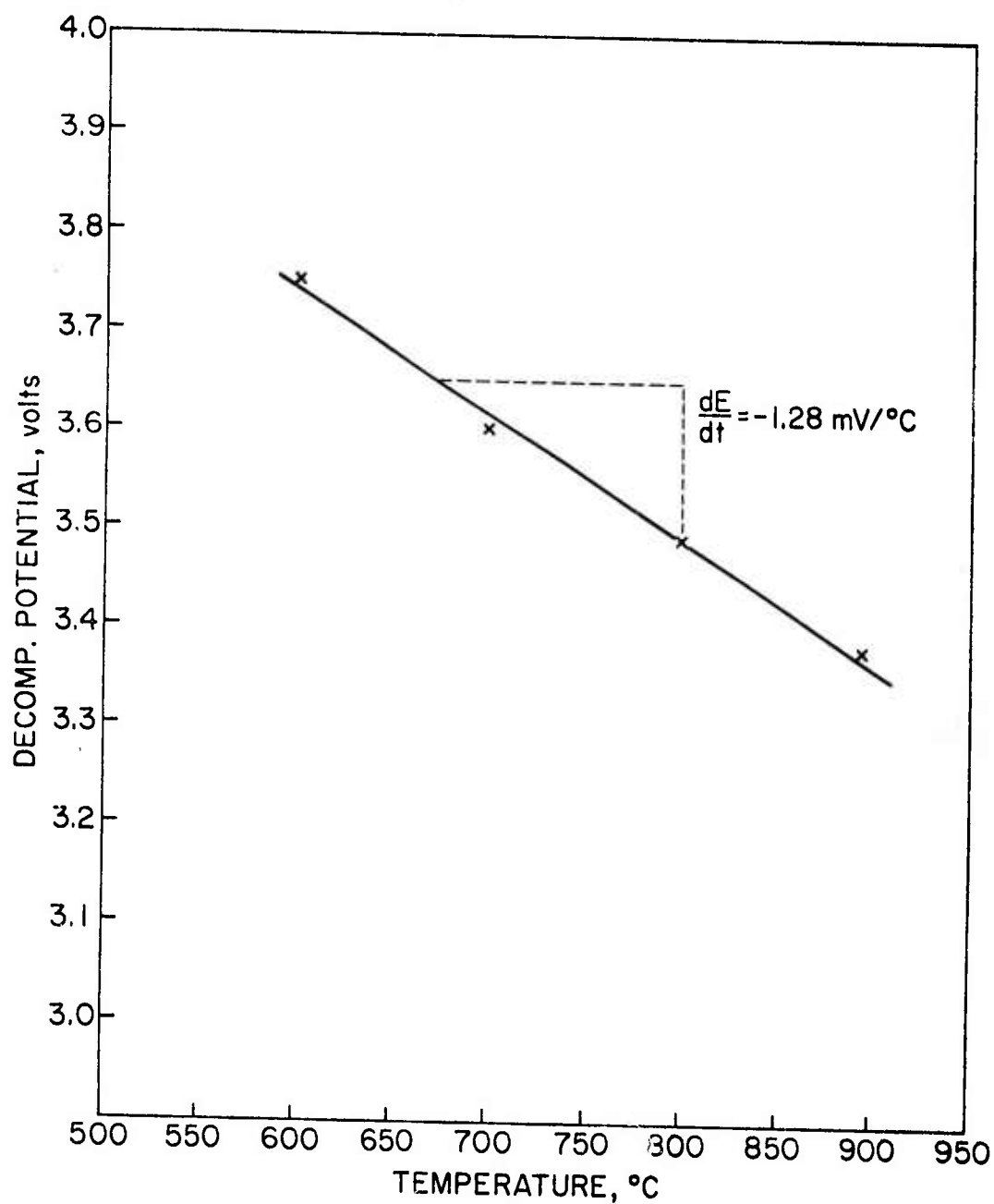


Figure 3. Decomposition potential of KF in LiF-KF eutectic vs. temperature. Au anode;  $dE/dt = 1.28 \text{ mV/}^\circ\text{C}$ .

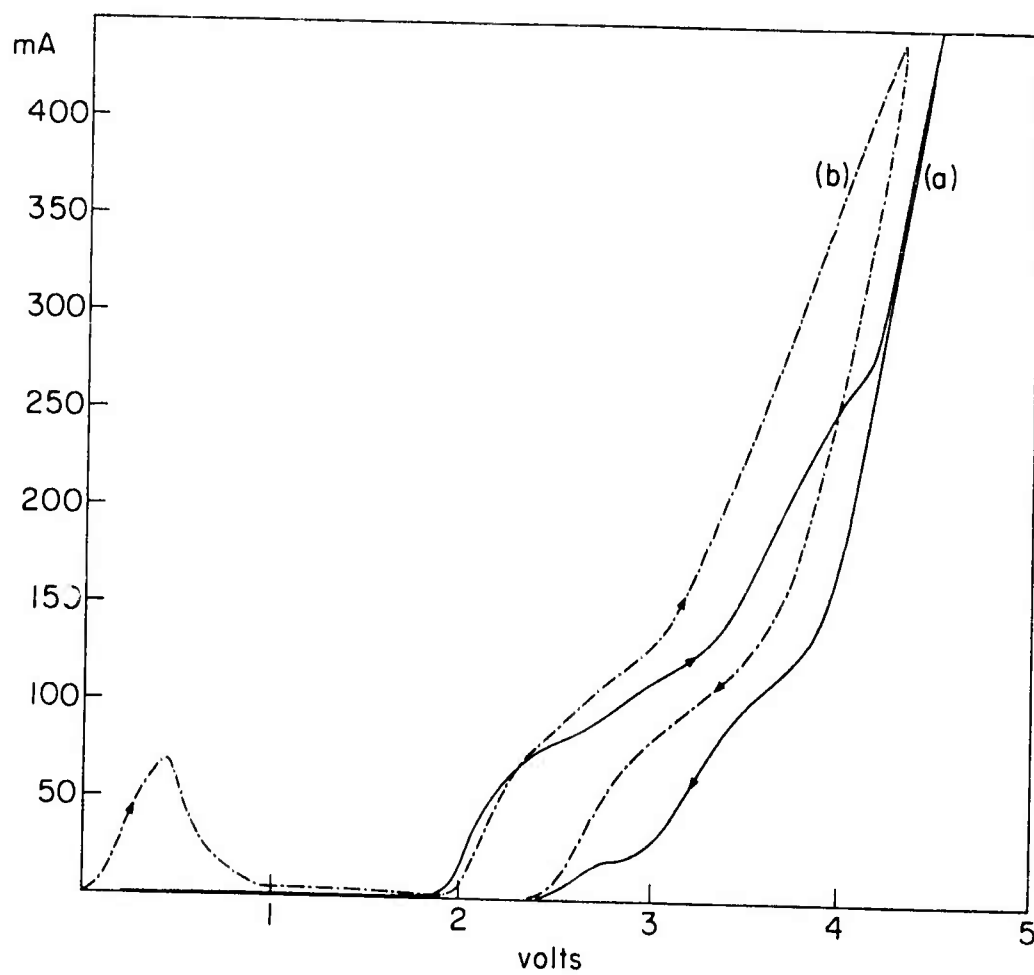


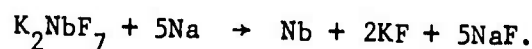
Figure 4. I-V curves of 0.2 mol % of  $K_2NbF_7$  in KF-LiF eutectic. Au anode;  $t = 563^\circ C$ ; (a)  $v = 33.3$  mV/sec.; (b)  $v = 83$  mV/sec.

system of  $K_2NbF_7$  in the LiF - KF - NaF eutectic by chronopotentiometry. They report anodic oxidation of  $Nb^{+5}$  to  $Nb^{+6}$  on inert electrodes such as graphite.<sup>(10)</sup> This reaction has  $E_{1/4} = 0.25V$  with respect to a  $Ni^{+2}/Ni$  reference electrode. They also reported<sup>(4)</sup> three steps in the reduction of the pentavalent niobium at 750°C with all decomposition potentials referred to the reference electrode  $Ni^{+2}/Ni$ : a reversible step  $Nb^{+5} + e^- \rightleftharpoons Nb^{+4}$  at -0.11V, a reversible step  $Nb^{+4} + 3e^- \rightleftharpoons Nb^{+1}$  at -0.76V, and an irreversible step  $Nb^{+1} + 1e^- \rightarrow Nb$  at -1.01V.

Figure 5 shows an I-V curve for a solution of 0.02 mol % of  $K_2NbF_7$  at 670°C. The first wave is observed at -1.77V and the second at -2.82V (after correction for IR drop of 0.10V, since  $R \approx 1.50 \Omega$ ). It should be noted that both waves proved to yield Nb metal as the cathode deposit. The absolute value for the decomposition potential, calculated from reference 4 by the addition of -1.01V and the  $NiF_2$  decomposition potential taken to be -2.72V at 750°C after Hamer and Malmberg<sup>8</sup>, yields a value of -3.73V for the  $NbF_5$  decomposition potential. This is about 0.91V more cathodic than the measured value of -2.82V.

It may be pointed out that Delimarskii and Grigorenko<sup>(11)</sup> reported the decomposition potential of  $NiF_2$  in NaF at 1000°C as -1.58V, whereas the theoretical value<sup>(6)</sup> for pure  $NiF_2$  at this temperature is -2.575V. However, the value of reference 8 is believed to be the true one, as other independent investigators reported a similar value.<sup>(12,13)</sup>

Kolchin and Vol'dman<sup>(14)</sup> report thermodynamic data for the reaction



As the free energy of the formation of NaF is known<sup>(8,15)</sup> it is possible to calculate the free energy change of the reaction

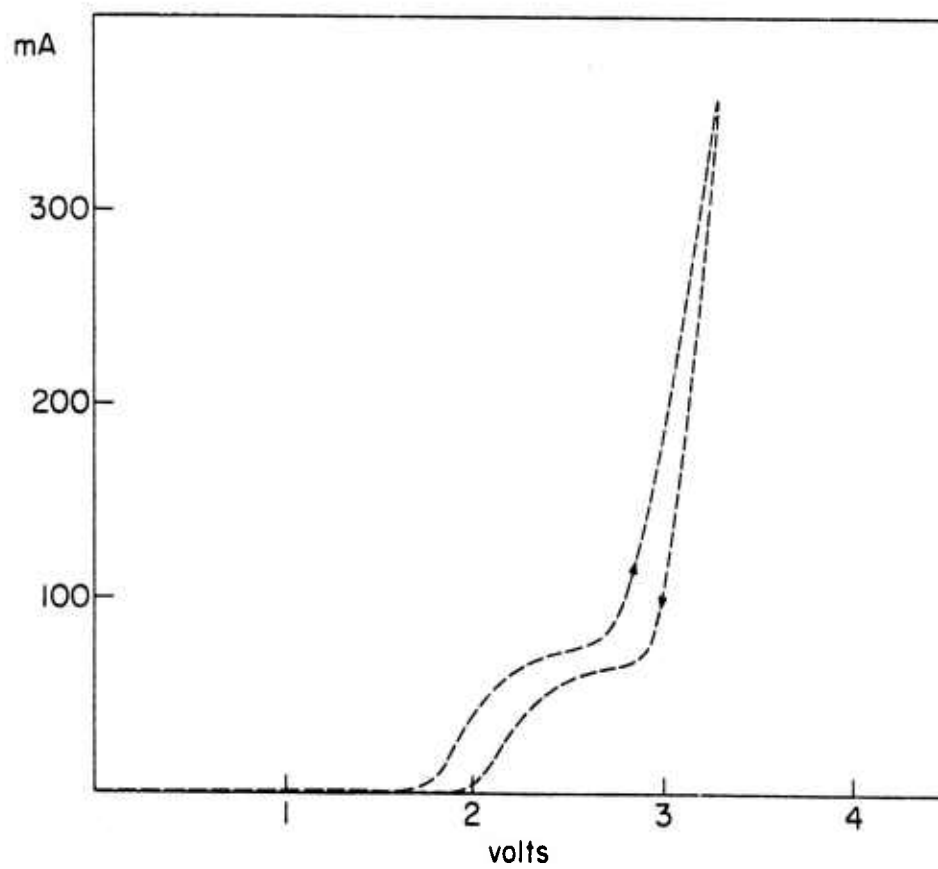
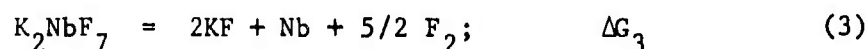


Figure 5. I-V curve of 0.02 mcl % of  $K_2NbF_7$  in KF-LiF eutectic. Au anode;  $t = 670^\circ\text{C}$ ;  $v = 33.3 \text{ mV/sec}$ .



which is the actual decomposition reaction in the fluoride solvent.

The reaction (3) may be considered as a linear combination of the following two reactions:



$$\Delta G_3 = \Delta G_2 - 5 \Delta G_1$$

According to reference 14, between 371 and 983°K:

$$\Delta G_2^\circ (T) = -258,150 + 19.42T$$

$$\text{and } \Delta G_1^\circ (T) \text{ is taken after Wicks and Block.}^{(15)}$$

To calculate the standard decomposition potential, use is made of the fundamental relationship

$$E^\circ = - \frac{\Delta G^\circ}{zF}$$

where  $z$  is the number of electrons transferred per atom,  $F$  is the Faraday constant, and  $\Delta G^\circ$  is expressed in Joules/mole.

Table II lists the theoretical values calculated by this way, and the experimental results for 670°C (943°K), and 563°C (836°K). In the experimental results, two major corrections should be made: a correction for the IR drop of the circuitry and bath ( $R \approx 1.5 \Omega$ ), and a correction for the concentration effect, according to the Nernst equation

$$\Delta E_{\text{conc.}} = \frac{-RT}{zF} \ln a_{\text{Nb}} + 5$$

TABLE II  
Decomposition potential of  $\text{NbF}_5$  in Alkali-Fluoride melts

Temperature	Concentration mole %	I-V Measured $E_{\text{decomp}}$	Correction for $\Delta E_{\text{conc.}}$	Correction for $\Delta E_{\text{IR}}$ ( $R = 1.5 \Omega$ )	Experimental $E^{\circ}_{\text{decomp}}$	Calculated $E^{\circ}_{\text{decomp}}$
670°C (943°K)	0.02%	-2.92 V	+ 0.148 V	+ 0.100 V	-2.67 V	-2.871 V
563°C (836°K)	0.2%	-3.31 V	+ 0.090 V	+ 0.195 V	-3.02 V	-2.851 V



where  $a_{\text{Nb}^{+5}}$  is taken to be equal to the concentration of  $\text{Nb}^{+5}$ .

The accuracy of the I-V technique, utilizing the gold quasi-reference electrode, was evaluated at 100 - 200 mV.

The effects of concentration and temperature were more extensively investigated at the first decomposition wave, which is considered to be more important from a practical point of view when co-deposition with other metals is desired. It was found that a concentration change by a factor of 10 results in a change in decomposition potential less than the experimental error. The temperature dependence, however, was well established. The dependency is linear, as can be seen in Figure 7, which was drawn on the basis of the data of the I-V curves such as Figure 6 for solutions of 0.2% and 80% of concentration.

The slope of the linear graphs of  $E_{\text{decomp}}$  vs.  $T$  becomes less negative with the decrease in concentration. A plot of  $E_{\text{decomp}}$  vs. the log of the mole fraction of  $\text{K}_2\text{NbF}_7$  in the solvent is shown in Figure 8 for 800°C. The slope is found to be 0.0432V, in excellent agreement with the predicted value of 0.0431V. The dependence of the I-V curves on the rate of voltage scanning can be seen in Figure 9, for the 80% concentration. The original peaks in the first curve, taken at scanning rate of 8.34 mV/sec have not been identified. They may be due to impurities, or intermediate valence reactions. It should be noted, however, that in all experiments, the first I-V curve has peaks which disappear in successive curves, tending to indicate the presence of impurities.

### 3. Aluminum Fluoride Decomposition Potential

An I-V curve for a 1.5 Mole % of  $\text{AlF}_3$  in the alkali fluoride was taken

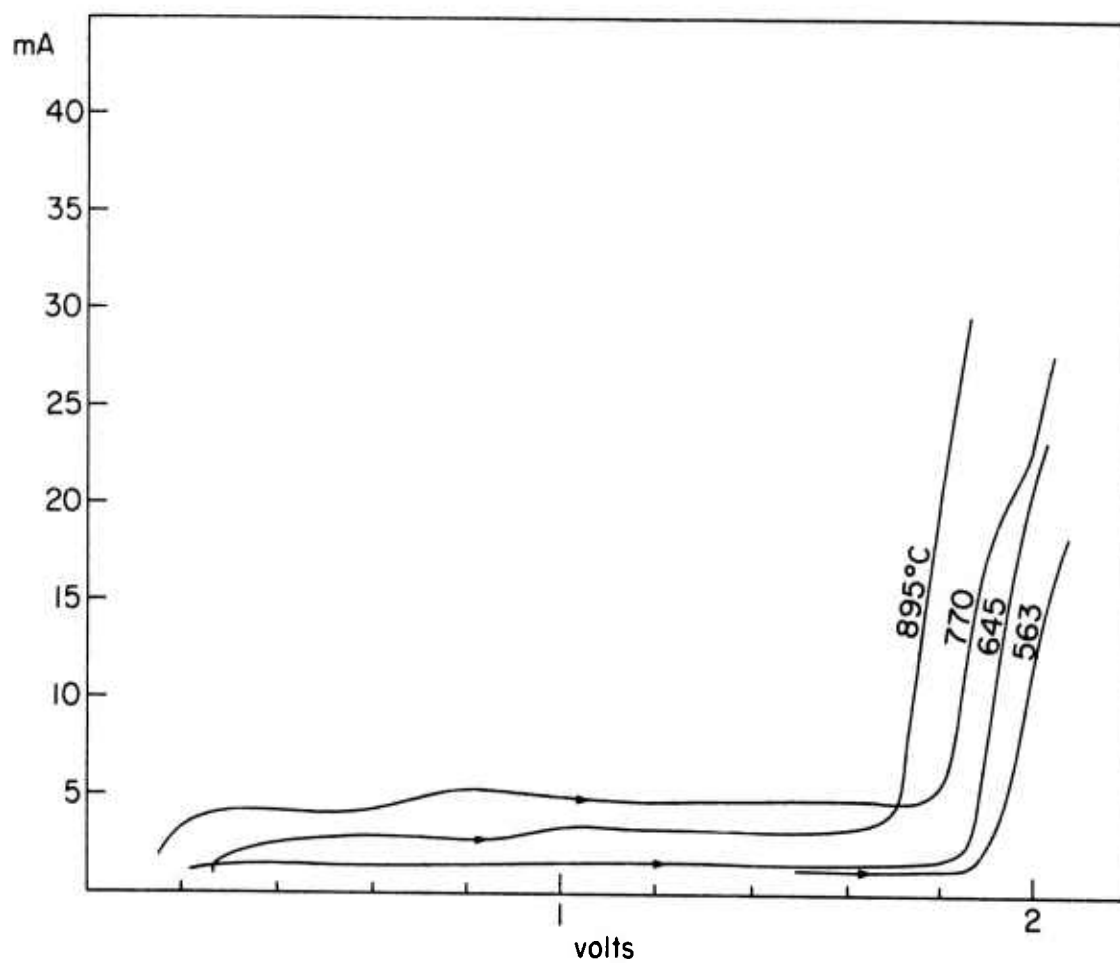


Figure 6. First wave of 0.2 mol %  $K_2NbF_7$  in KF-LiF eutectic at different temperatures.  $v = 3.33$  mV/sec.

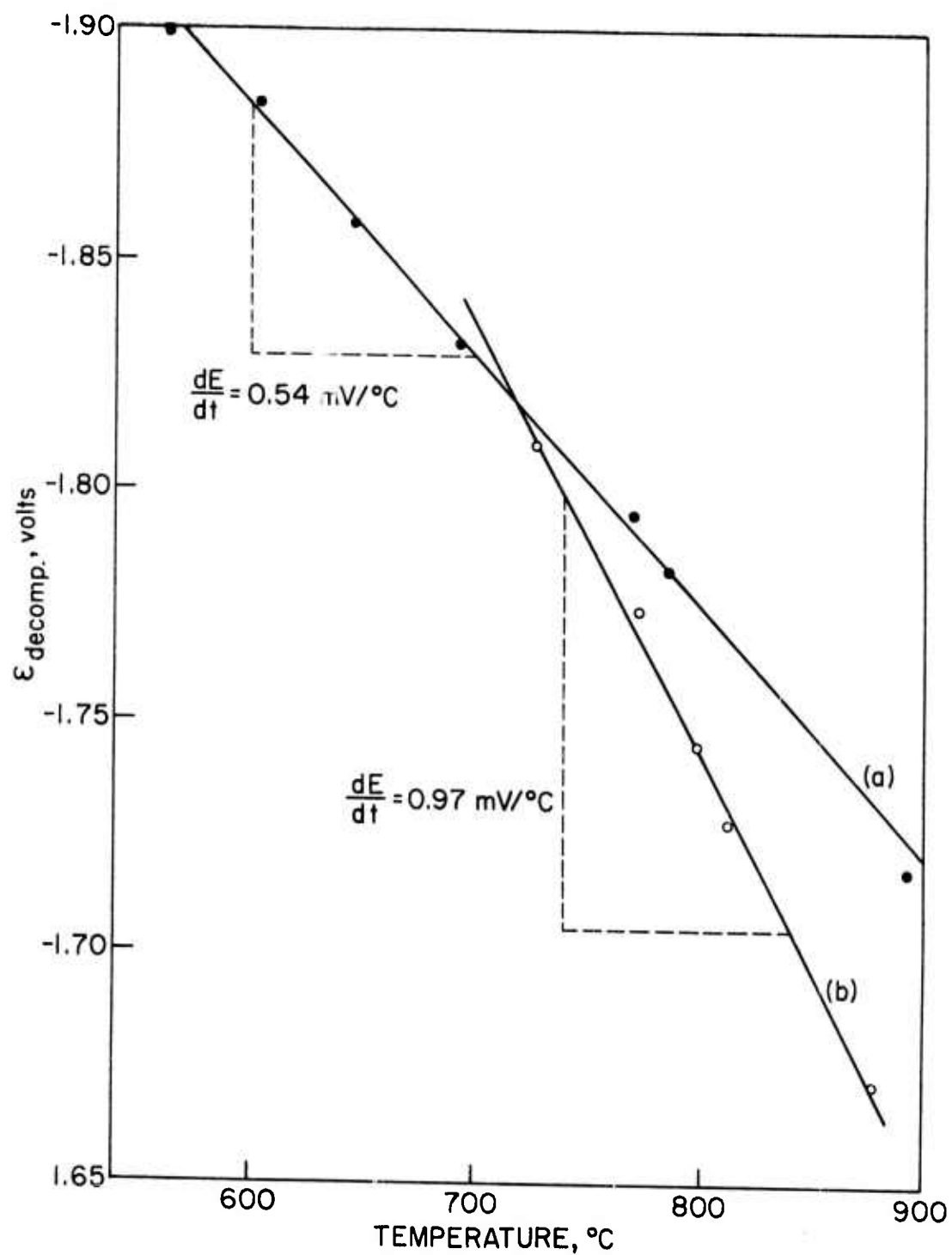


Figure 7. First wave potential of  $\text{K}_2\text{NbF}_7$  in KF-LiF eutectic vs. temperature. (a) 0.2 mol %;  $dE/dt = 0.54 \text{ mV/}^\circ\text{C}$ . (b) 80 mol %;  $dE/dt = 0.97 \text{ mV/}^\circ\text{C}$ .

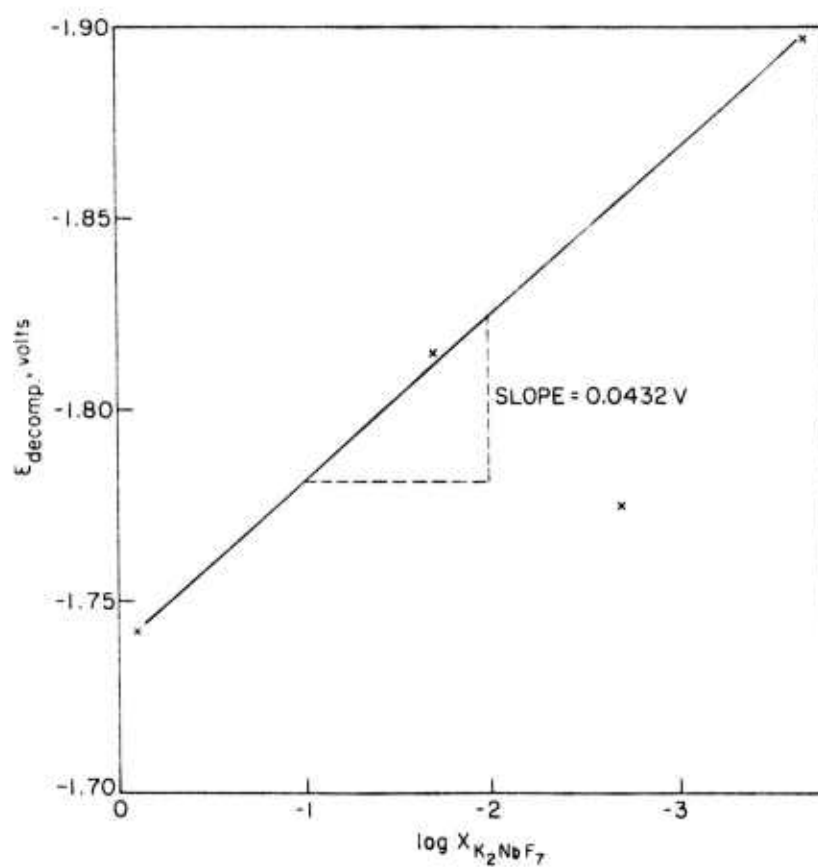


Figure 8. First wave potential of  $\text{K}_2\text{NbF}_7$  vs. log of mole fraction of  $\text{K}_2\text{NbF}_7$  in KF-LiF eutectic.  $t = 800^\circ\text{C}$ ; slope = 0.0432 V.

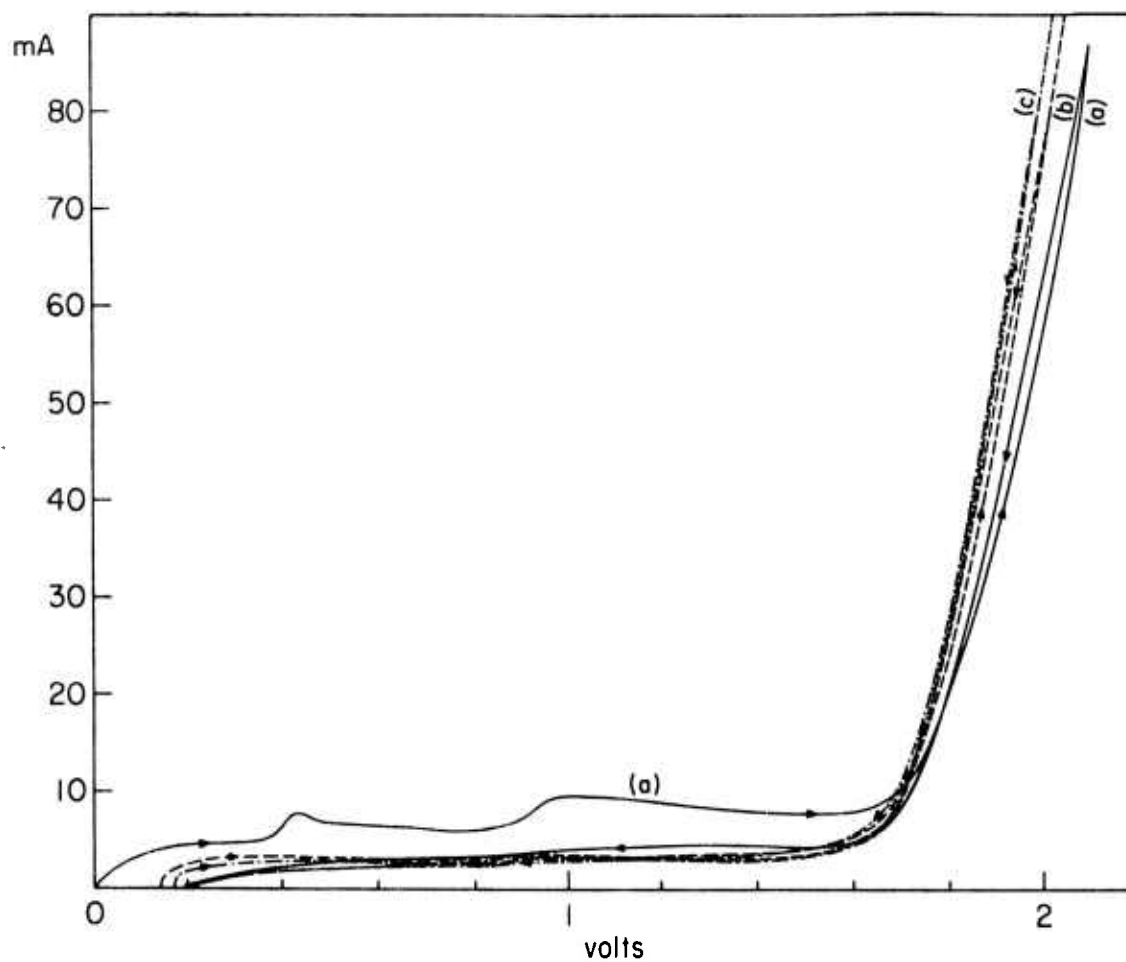


Figure 9. The effect of scanning rate on the first wave of 80 mol %  $K_2NbF_7$  in KF-LiF eutectic.  $t = 812^\circ C$ ; Au anode; (a)  $v = 8.34$  mV/sec.; (b)  $v = 3.33$  mV/sec; (c)  $v = 1.66$  mV/sec.

with a Nb anode and cathode. The result obtained is shown in Figure 10. The bump on the curve increased with successive runs and developed into two peaks. Since the original bath did not contain any Nb, these bumps are believed to be due to the Nb deposition after anodic dissolution. This system is rather ill-defined, since the Nb concentration is not fixed. However, this experiment clearly indicates that Nb is much more noble than Al in the fluoride melts.

A better-defined system was achieved using the gold quasi-reference electrode. The I-V curves obtained are shown in Figure 11.

Low temperatures were chosen, since at temperatures higher than 660°C, aluminum melts, floats on the melt surface and shorts the electrodes. Also, as it floats, the effective cathode surface area increases rapidly.

Two waves are observed before the solvent decomposition. The first wave at about -2.03V and the second at about -3.26V. Different I-V curves were observed for the solution at a lower temperature (520°C), as seen in Figure 12. These results are non-conclusive, but they clearly demonstrate that Al deposits at a more cathodic potential than Nb. As an estimate of how much the Nb and Al decomposition potentials differ, the  $E^\circ$  value for pure  $\text{AlF}_3$  at 560°C taken from Hamer and Malmberg<sup>8</sup> is -3.825V, while for  $\text{NbF}_5$ , as previously noted, the value is -3.02V. Actually, Nb deposits in the first wave, at about -1.90V. This large difference in the deposition potentials of the two metals, renders them a non-compatible couple for codeposition. It is possible that the two waves in the I-V curves of  $\text{AlF}_3$  before the solvent decomposition wave belong to intermediate valencies, such as  $\text{Al}^{+3} + 2e^- \rightarrow \text{Al}^+$ , and the actual decomposition wave of  $\text{AlF}_3$  is masked by the solvent decomposition. One should remember that the solvent decomposition

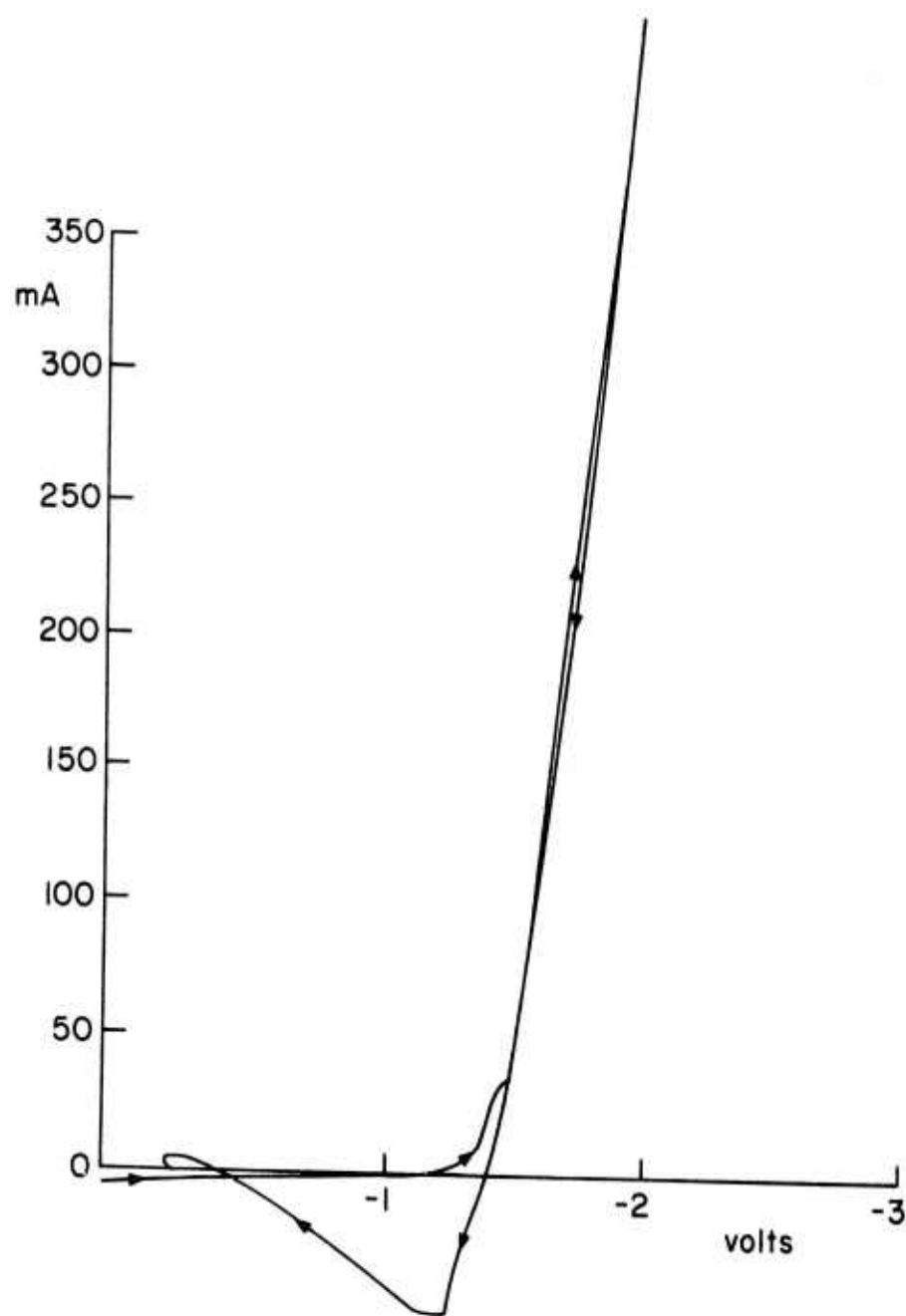


Figure 10. Al deposition from 1.5 mol % of  $\text{AlF}_3$  in KF-LiF eutectic, using Nb anode.  
 $t = 550^\circ\text{C}$ ;  $v = 16.6 \text{ mV/sec}$ .



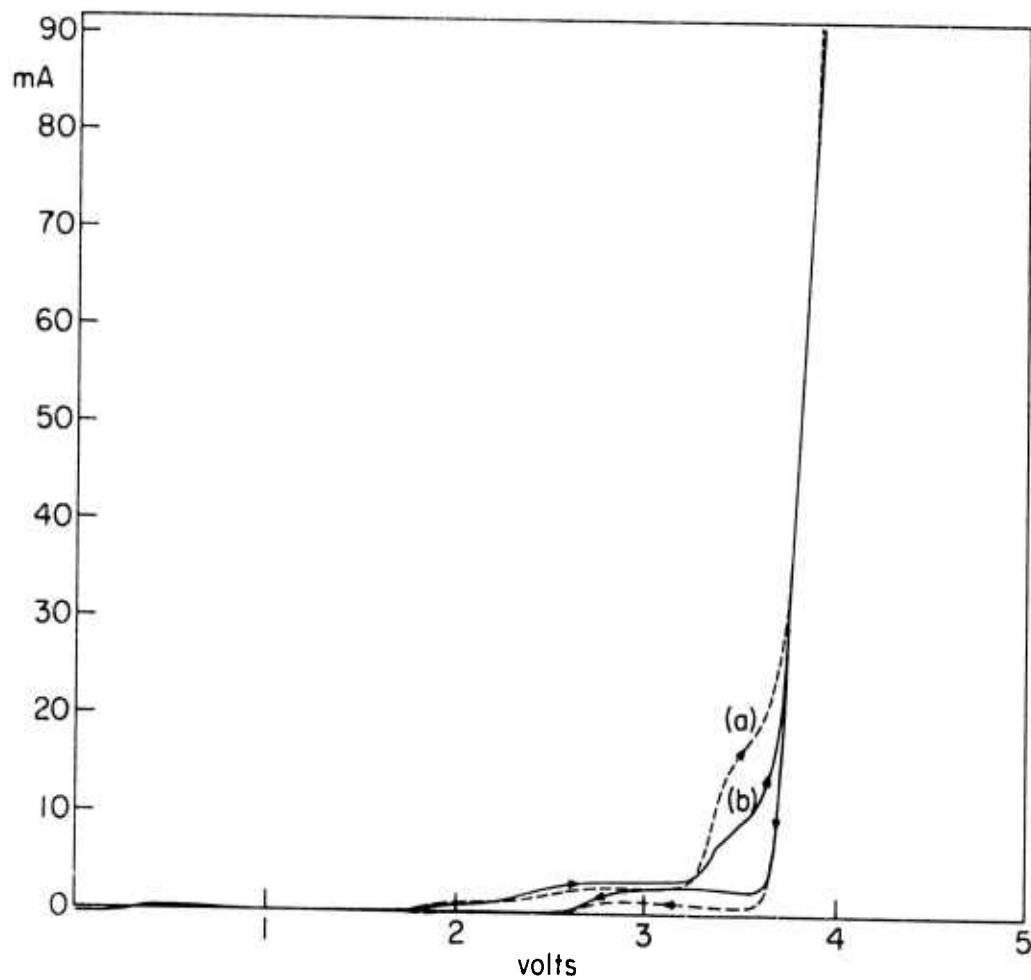


Figure 11. I-V curves of 1.5 mol %  $\text{AlF}_3$  in KF-LiF eutectic.  $t = 565^\circ\text{C}$ ; Au anode; (a)  $v = 83 \text{ mV/sec.}$ ; (b)  $v = 8.34 \text{ mV/sec.}$

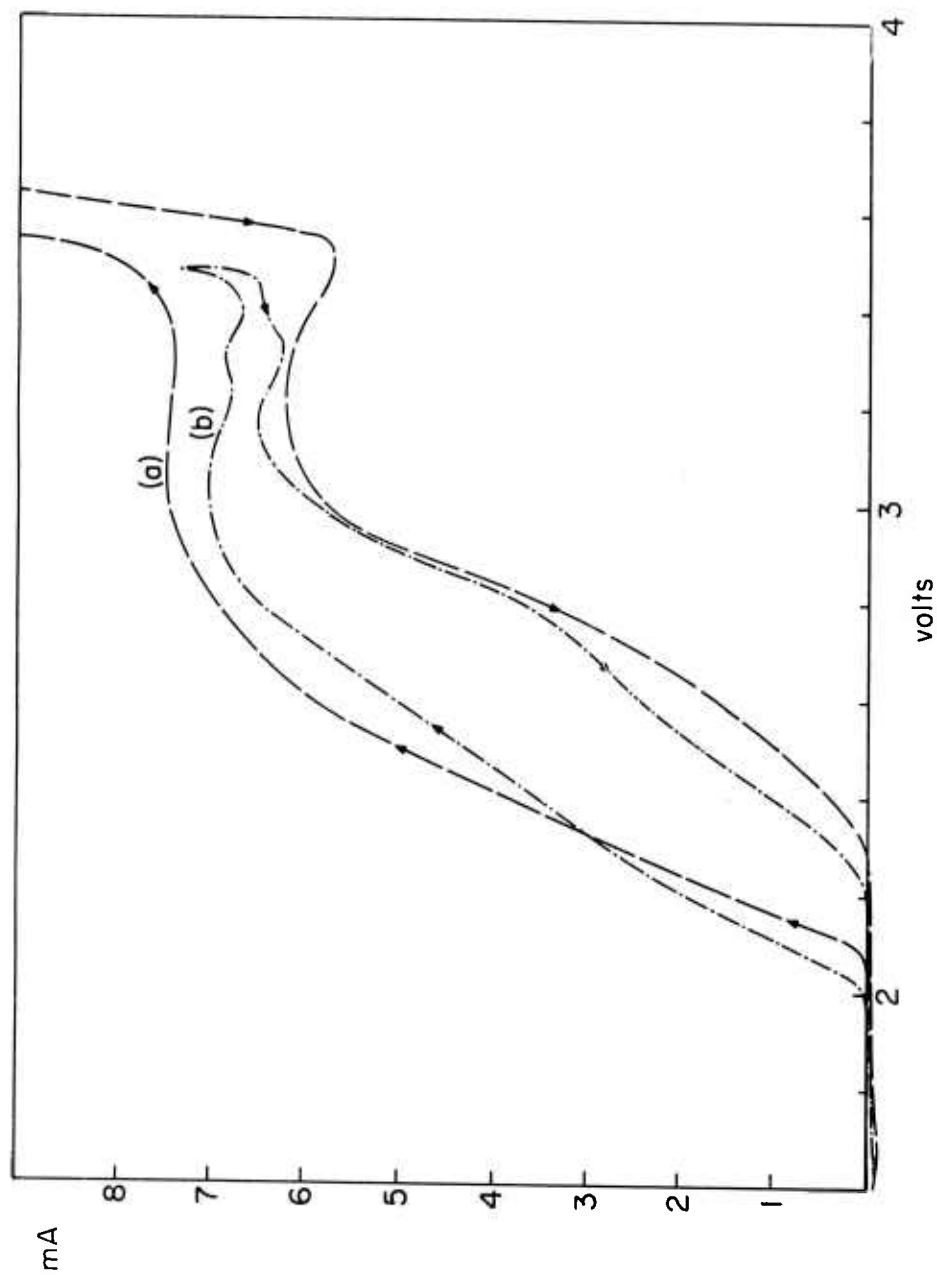


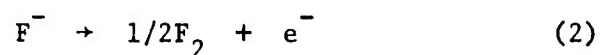
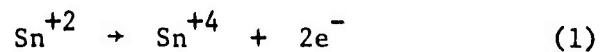
Figure 12. I-V curves of 1.5 mol  $\text{AlF}_3$ .  $t = 520^\circ\text{C}$ ;  
 Au anode; (a)  $v = 33.3 \text{ mV/sec.}$ ;  
 (b)  $v = 8.34 \text{ mV/sec.}$

potential was found to be -3.75V at 600°C, and that  $\text{AlF}_3$  in the solvent is in a complex form such as  $\text{AlF}_6^{-3}$ , which is more stable than pure  $\text{AlF}_3$ , and a higher  $E^\circ$  is required for the decomposition of this complex. The big difference in the deposition potentials explains the fact that codeposition of Al and Nb was never achieved, even at the lowest practical Nb concentration and highest practical Al concentration.

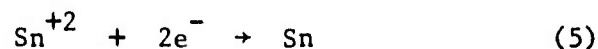
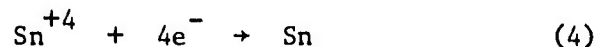
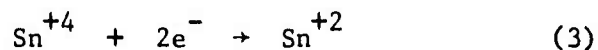
#### 4. Tin Fluoride Decomposition Potential

I-V curves for the decomposition potentials of  $\text{SnF}_2$  in the KF-LiF eutectic were taken. The investigation of this system, however, was only in a preliminary stage, when the compound  $\text{Nb}_3\text{Ge}$  was found to have a superconducting transition temperature of 23°K, and interest shifted to the Nb-Ge system.

Figure 13 and 14 are I-V curves of 0.1%  $\text{SnF}_2$  solution at 655°C. Two rates of scan and two current scales are indicated. The general appearance of the curves is rather complex. Four waves are observed before the solvent decomposition. Sn is known to have two stable valencies,  $\text{Sn}^{+4}$  and  $\text{Sn}^{+2}$ . Since the anode was Au, two anode reactions are possible



The possible cathode reactions are:



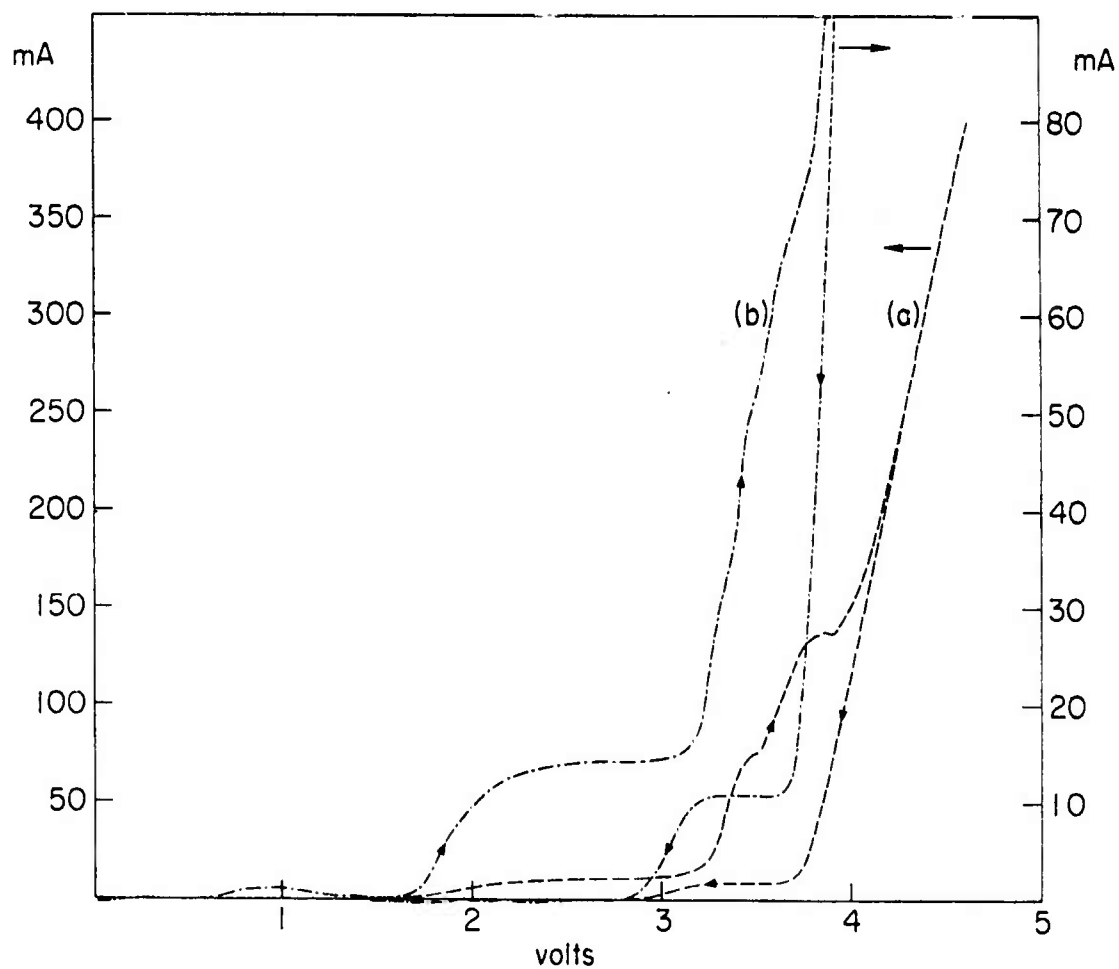


Figure 13. I-V curves of 0.1 mol % of  $\text{SnF}_2$  in KF-LiF eutectic.  $t = 655^\circ\text{C}$ ; Au anode; (a)  $v = 3.33$  mV/sec.; (b)  $v = 166$  mV/sec.

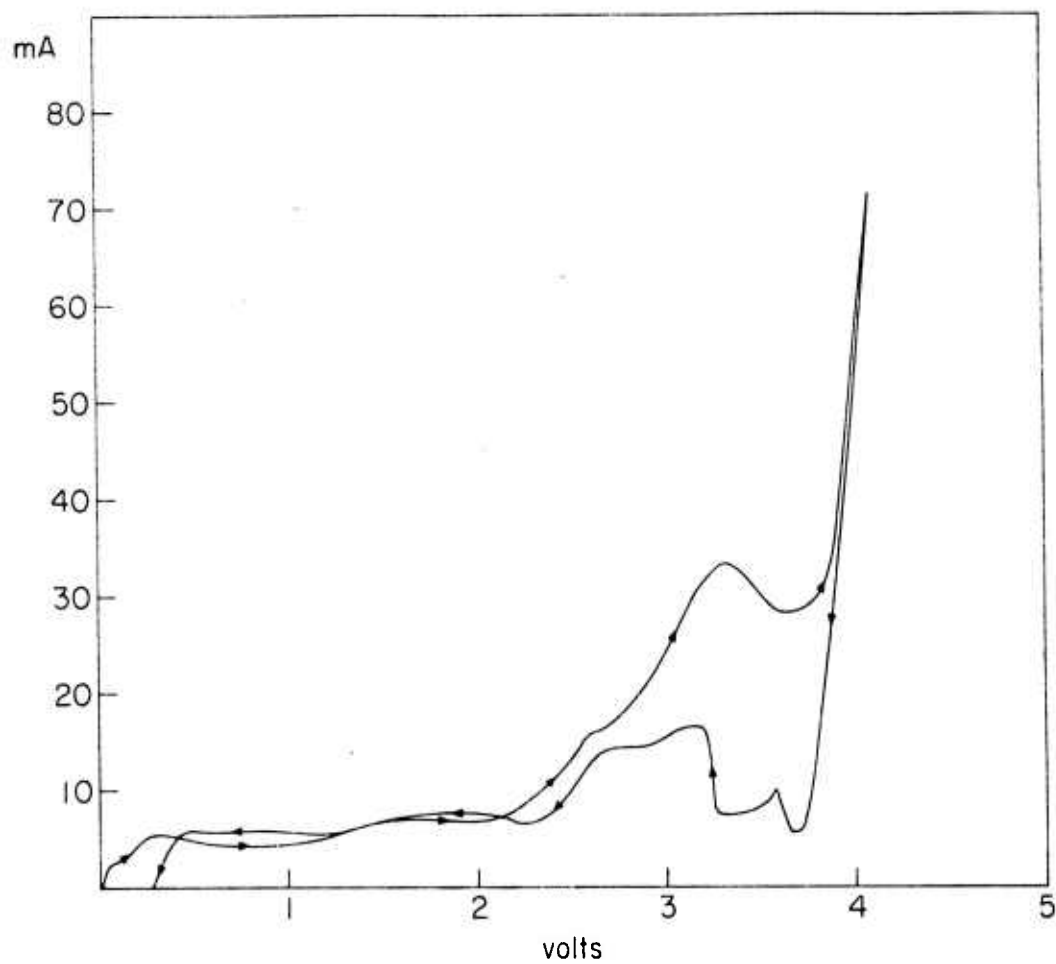


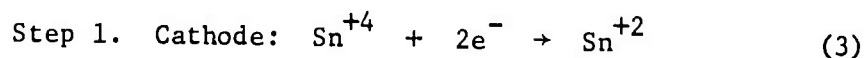
Figure 14. I-V curve of 1.0 mol % of  $\text{SnF}_2$ .  
 $t = 650^\circ\text{C}$ ;  $v = 83 \text{ mV/sec}$ .

A lack of thermodynamic data for the tin fluorides, such as the redox potential of the couple  $\text{Sn}^{+4}/\text{Sn}^{+2}$ , prevents the ordering of the reactions.

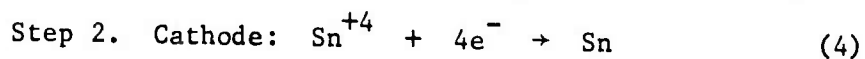
It is known that in the chlorides, the decomposition potential of  $\text{Sn}^{+4}$  is lower than that of  $\text{Sn}^{+2}$ . It is, therefore, reasonable to assume that reaction (4) occurs before (5) in the fluorides, too.

Also, in the chlorides, the redox potential of the couple  $\text{Sn}^{+4}/\text{Sn}^{+2}$  is much below that of the deposition of any ions (reaction (4) or (5)). Interpretation of the curves of Figure 13 can be helped by the fact that the starting salt was  $\text{SnF}_2$ , and, therefore, initially  $\text{Sn}^{+2}$  is the major species.

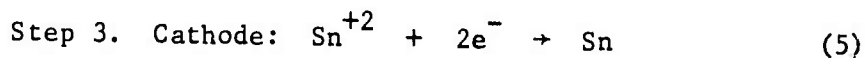
The anodic reaction (1) is believed to occur before (2), and the hypothetical sequence of reactions is the following:



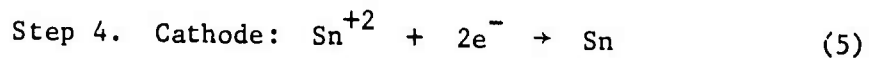
(This step should begin at zero potential or close to it.)



(This with a simultaneous reaction (3).)



(This with simultaneous reactions (3) and (4).)



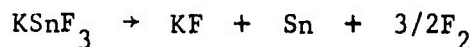
(with simultaneous cathode reactions (3) and (4) and the anode reaction (1).)

The following evidence supports this hypothesis. The first wave begins close to zero potential, and has a rather low limiting current peak, as initially there is a very low concentration of  $\text{Sn}^{+4}$  available for reaction (3). The second step accordingly, should also have a low limiting current as it depends on reaction (3). This is verified in the curves of Figures 13 and 14 where the peak of the second wave is at about -0.75V.

The third wave is observed to have a much higher limiting current, as this wave depends on the more available  $\text{Sn}^{+2}$  for reaction (5). The fourth step begins at -3.24V, and depends on the concentration of  $\text{F}^-$  (reaction (2)) and  $\text{Sn}^{+2}$  (reaction (5)). Considering Step 4 as the ultimate decomposition of  $\text{SnF}_2$ , the break is found at -3.23V. The correction for IR drop is +0.021V, and the concentration correction is +0.276V. The corrected experimental value for  $E^\circ_{\text{decomp}}$  is -2.93V for  $\text{SnF}_2$  in the alkali fluoride melt. Thermodynamic data for the alkali tin fluorides is rather scarce. It is known that the most stable species is  $\text{SnF}_3^-$  and  $\Delta G^\circ_{298} = -11,480$  for the reaction  $\text{Sn}^{+2} + 3\text{F}^- \rightarrow \text{SnF}_3^-$ , after Hall and Slater.<sup>16</sup> The free energy of formation for  $\text{SnF}_2$  is taken from Wicks and Block<sup>15</sup> and extrapolated to 655°C (928°K).

$$\Delta G^\circ_{298^\circ\text{K}} = -126,520 \text{ Cal/mole}$$

Since no data are available for  $\text{SnF}_3^-$  at temperatures other than 298°K, the decomposition free energy change for the reaction



$$\begin{aligned} \text{is taken as } \Delta G^\circ_{\text{decomp}} &= -(-126,520 - 11,480) = \\ &= +138,000 \text{ Cal/mole,} \end{aligned}$$

$$\text{and } E^\circ_{\text{decomp}} = -2.992\text{V at } 928^\circ\text{K.}$$

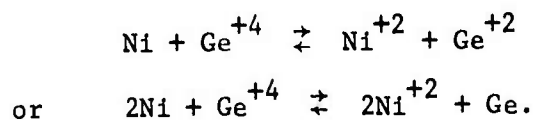


The agreement between this calculated value and the experimental value of -2.93V is very good.

It should be noted that the tin metal was observed to deposit at lower potentials than this value, that is to say, at about -2.00V, and thus providing further support for the hypothesis concerning the reaction sequence. According to this hypothesis, the third wave, initiating at about -1.68V can deposit Sn without fluorine evolution. This value of -1.68V is close to the value for niobium deposition at its first wave (about -1.87V) and a codeposition compatibility was established. Nb and Sn have been codeposited. See Section 6.

#### 5. Germanium Fluoride Decomposition Potentials

I-V curves for 1% of  $K_2GeF_6$  in the LiF-KF eutectic are shown in Figure 15. The decomposition potential is clearly seen to be about -1.71V. In addition to this main wave, a small wave initiates at about -1.1V. The small wave is believed to be due to Ni contamination. Figure 15 is from an experiment, which was prepared by mixing LiF - KF -  $K_2GeF_6$  -  $KHF_2$ , melting and HF treating. On cooling and opening the can system, there was evidence of a severe attack on the Ni tubes of the bubbler and thermocouple well. It is believed that a substitution reaction took place:



Support for this assumption was found when the deposit from electrolysis at a constant voltage of -1.40V was analyzed and proved to be mostly Ni, with traces of Ge. Another electrolysis at a constant voltage of -1.73V gave Ni and  $Ni_3Ge$ .

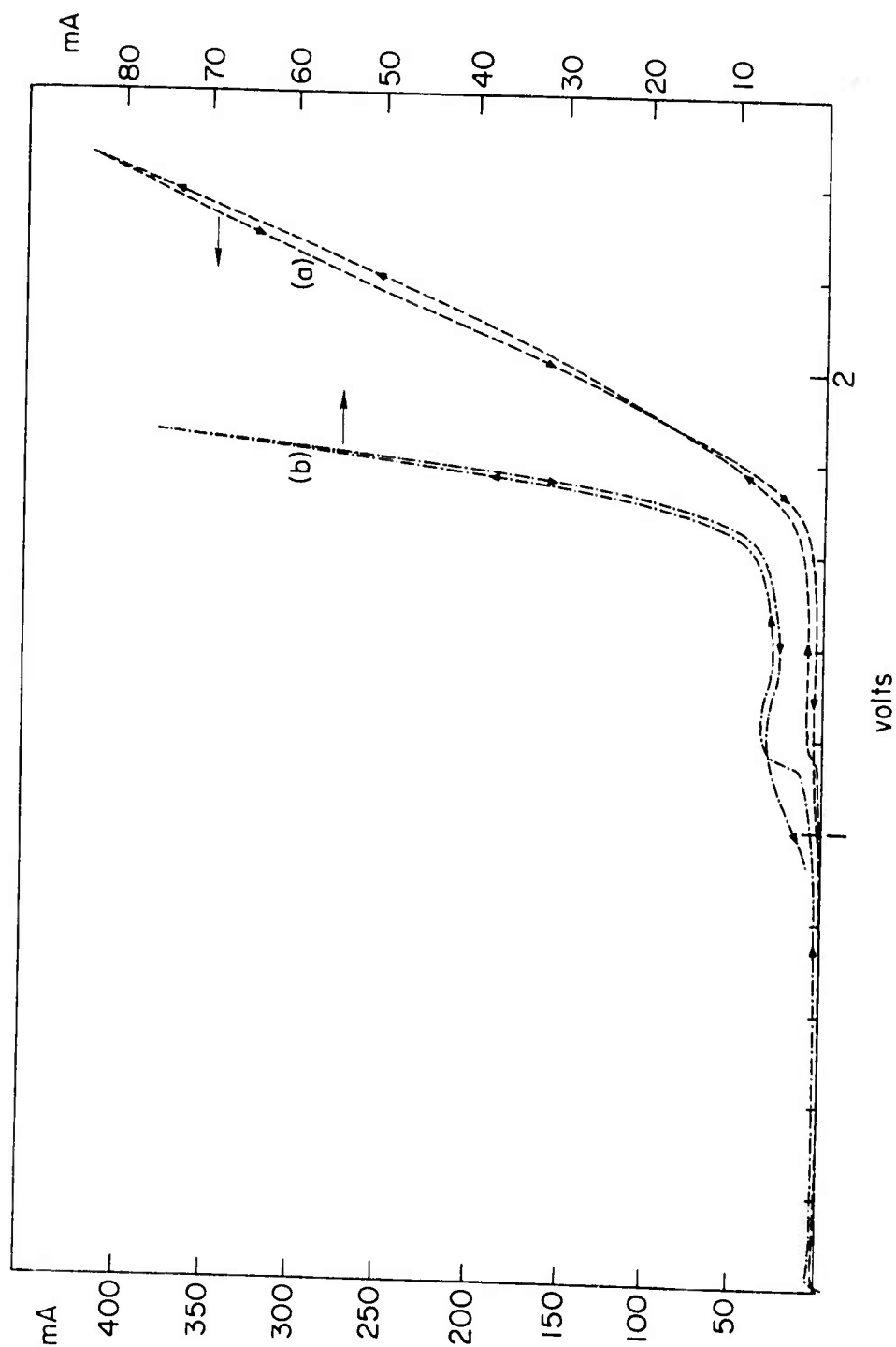


Figure 15. I-V curves of 1.0 mol % of  $K_2GeF_6$  in KF-LiF eutectic.  $t = 753^\circ C$ ; Au anode; (a)  $v = 16.6$  mV/sec.; (b)  $v = 3.33$  mV/sec.

With the addition of Ge and Nb metal chips to the solution used in the earlier experiment, different I-V curves were obtained, as seen in Figure 16. The main wave is now at about -2.42V.

All subsequent electrodeposits from this solution contained only niobium with traces of nickel. No Ge was obtained at potentials lower than -2.30V. The reason for the change in the decomposition potential is not clear. The shape of the latter curves and the wave positions were stable and reproducible.

At the time, it was believed that the species depositing at  $E_{\text{decomp}} = -2.42\text{V}$  was the stable germanium species at equilibrium in the solution. Recalling that for niobium, the first decomposition wave was observed at about -1.80V (at 760°C), it was concluded that niobium was more noble than germanium by about -0.60V. This conclusion, however, was later proved wrong. Niobium metal was dipped in a freshly prepared germanium solution with germanium metal chips. A metallic lump immediately appeared around the niobium metal, and was found to contain Ge and  $\text{Ge}_2\text{Nb}$ . This indicated that Nb metal may not be used as free element or an anode in germanium fluoride solutions. The failure to obtain Ge electrodeposits in all the experiments where Nb metal was used either as chips, an anode, or even as a cathode under low cathodic potential was the result of germanium ions being replaced by niobium. In all these cases, Nb electrodeposits were the only product, though sometimes they contained traces of Ge. Realizing now that Ge is the more noble metal, an experiment with a solution of  $\text{K}_2\text{GeF}_6$  and  $\text{K}_2\text{NbF}_7$  in  $\text{LiF} - \text{KF}$ , and with Ge chips in the crucible was prepared. A Ge anode and Ni cathode were used for the I-V curves, Figure 17, and for a constant voltage electrolysis at -150 mV. A ternary alloy of the

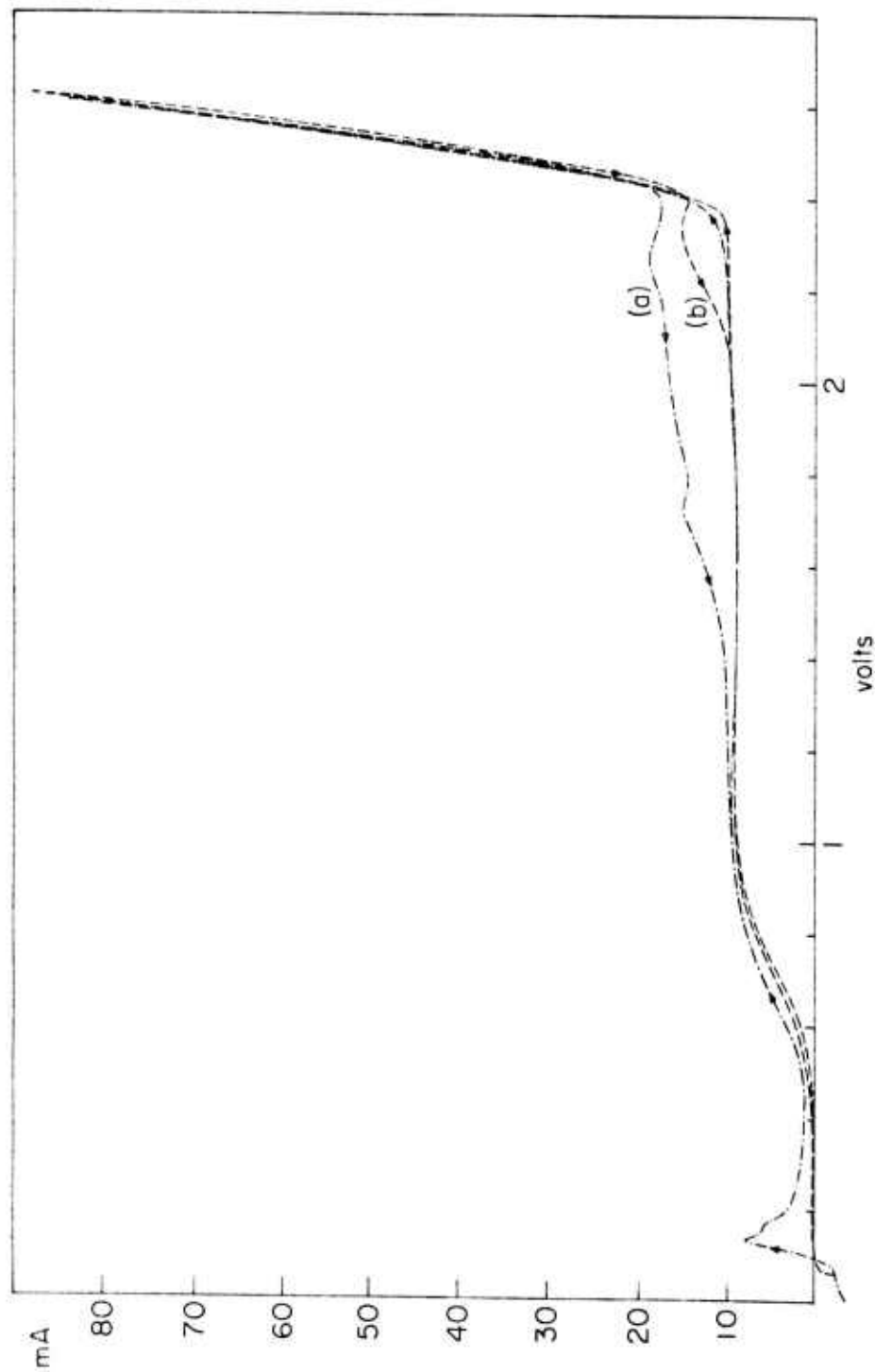


Figure 16. I-V curves of the solution of Figure 15, after addition of Ge and Nb metal chips.  $t = 752^{\circ}\text{C}$ ; Au anode; (a)  $v = 33.3 \text{ mV/sec.}$ ; (b)  $v = 8.34 \text{ mV/sec.}$

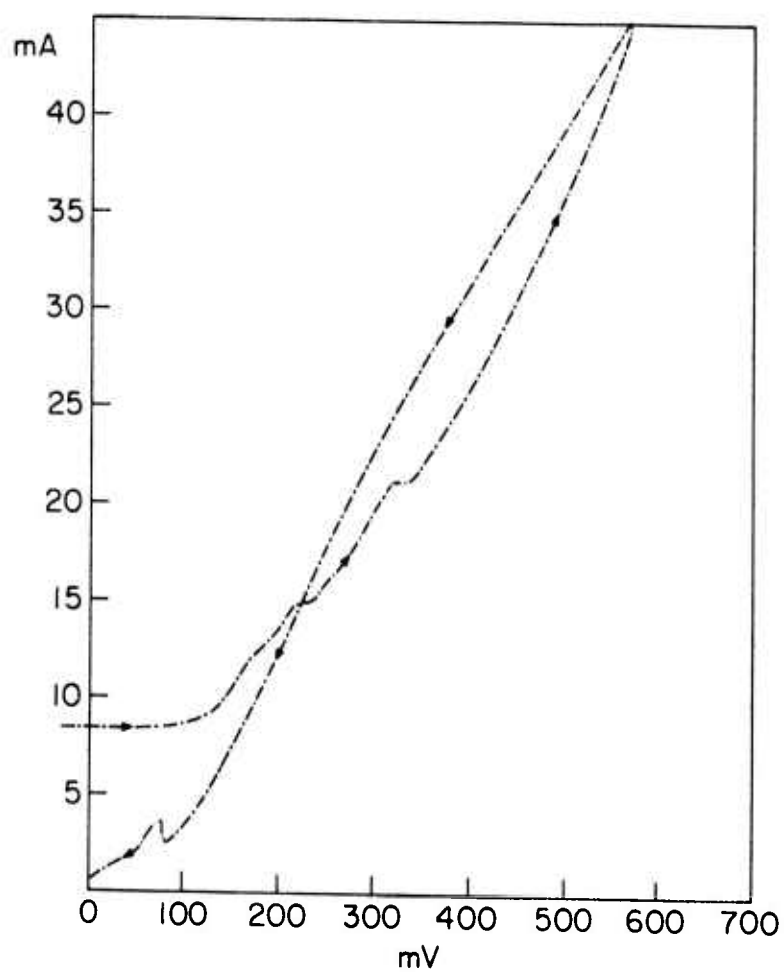


Figure 17. I-V curve of 0.2 mol %  $\text{K}_2\text{NbF}_7$ , 0.2 mol %  $\text{K}_2\text{GeF}_6$  in KF-LiF eutectic. Using Ge anode, and Ni cathode.  $t = 712^\circ\text{C}$ ;  $v = 8.34 \text{ mV/sec}$ .

composition  $\text{Ni}_{2-x}\text{GeNb}_x$  where  $0 \leq x \leq 0.1$  was found. It was concluded that  $\text{Ge}(E_{\text{decomp}} = -1.71\text{V})$  is more noble than  $\text{Nb}(E_{\text{decomp}} = -1.82\text{V})$  by about 100 - 200 mV at  $750^\circ\text{C}$  in the alkali fluoride solvent. This couple is, therefore, compatible for codeposition.

## 6. Alloy Codeposition

(a) Although codeposition of Nb-Al alloys has been tried under a wide range of conditions, codeposition has never been accomplished, Nb being the exclusive electrodeposit in all cases. In light of the recently obtained data on individual decomposition potentials, and available thermodynamic data, it is now concluded that Nb is much more noble than Al in fluoride melts. As the deposition potentials of the two are far apart, no codeposition is feasible. Consequently, the work on Nb-Al codeposition was terminated.

(b) Codeposition of Nb-Sn was accomplished. The work on this system is still in a preliminary stage, as major interest has shifted to the Nb-Ge system. Figure 18 is a micrograph of the cross section of a Ni wire cathode with a  $10\ \mu$  deposit. Chemical analysis by electron microprobe revealed two phases. The phase in the center of the deposit was of the composition  $\text{Nb}_3\text{NiSn}_{0.33}$ ; the other one on both sides of the middle layer, was  $\text{Ni}_4\text{NbSn}_{0.5}$ . The source of Ni could be either the Ni wire substrate or  $\text{NiF}_2$  contamination.

The electrodeposition was performed with a Au anode, Ni cathode, and a fluoride solution of  $\text{K}_2\text{NbF}_7$  - 2 mol %,  $\text{SnF}_2$  - 1 mol %. A constant voltage of -2.00V (Ni vs. Au anode) was used, yielding current density of  $\sim 1.2\ \text{A/cm}^2$ . At this voltage, according to the I-V curves of Figures 5 and 13, the niobium deposits at the first wave, and the tin deposits at its third wave. Recalling the hypothesis concerning the tin reaction series, the third wave



Figure 18. Cross section of Ni wire  
substrate and electrodeposit.  
1050 X.



corresponds to the cathode reaction  $\text{Sn}^{+2} + 2e^- \rightarrow \text{Sn}$  and the anode reaction  $\text{Sn}^{+2} \rightarrow \text{Sn}^{+4} + 2e^-$ . The first wave had zero cathode efficiency. This explains the reason for the high current density used in this experiment, and the very low cathode efficiency. No fluorine evolution is expected at -2.00V for tin, but fluorine does evolve for  $\text{K}_2\text{NbF}_7$  at this voltage. It was found that the gold weight loss was 0.9% for continuous electrolysis at a constant voltage of -2.00V and anode current density of about  $500 \text{ mA/cm}^2$ . Recall that in  $\text{K}_2\text{NbF}_7$  decomposition alone, such current densities were disastrous for the Au anodes. It was, however, possible in this case, since most of the anode current was dissipated via the reaction  $\text{Sn}^{+2} \rightarrow \text{Sn}^{+4} + 2e^-$ .

(c) Codeposition of Nb-Ge was also accomplished. Figures 19 and 20 show a cross section of Ni wire cathode (#900). A coherent layer of an excellent bonding deposit is seen. The layer thickness is about 60 - 80  $\mu\text{m}$ . A ring of particles about a fourth of the way out can be seen. These particles of about 1 - 5  $\mu$ , have a composition of  $\text{Ni}_{2-x}\text{GeNb}_x$ , where x can be as large as 0.1. The rest of the coherent deposit is  $\text{Ni}_2\text{Ge}$ , with Nb traces. The sample was electrodeposited from a fluoride solution of  $\text{K}_2\text{NbF}_7$  0.2 mol %, and  $\text{K}_2\text{GeF}_6$  0.2 mol %. A Ge plate was used as the anode, and Ni wire as the cathode. An I-V curve was first taken (see Figure 17) and a constant voltage electrolysis at -0.15V followed on the same sample. The niobium-rich particles were probably formed during the higher voltage part of the I-V experiment. The total charge transferred in the two parts of the experiment, the I-V and the constant voltage electrolysis were about equal.

This experimental result supports the conclusion of a previous section, namely, that the germanium is more noble than niobium in the fluoride melts by about 100 - 200 mV. Clearly, it is possible to co-deposit the two, and work on the electrodeposition of  $\text{Nb}_3\text{Ge}$  is now in progress.

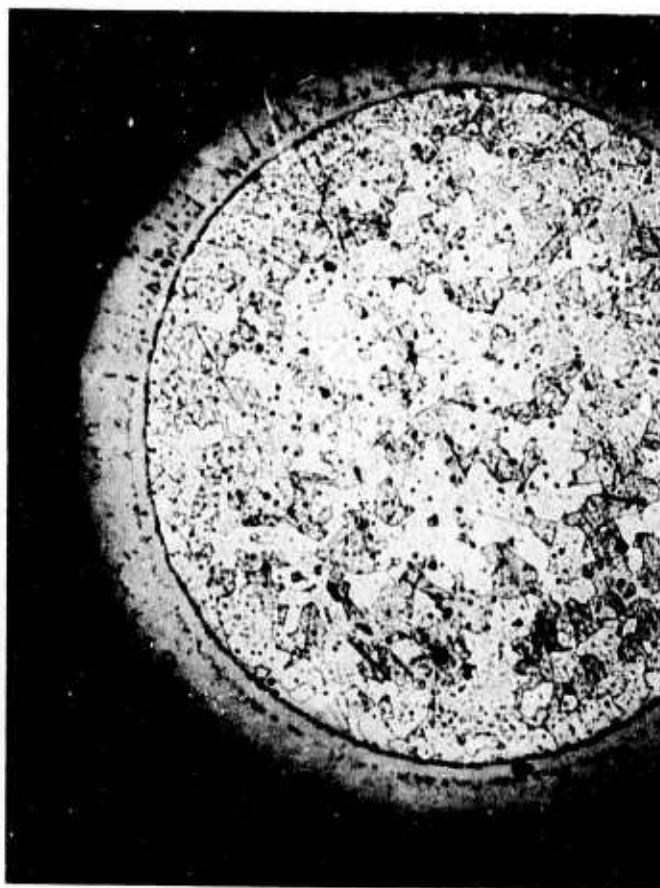


Figure 19. Cross section of Ni wire  
substrate and electrodeposit.  
200 X.

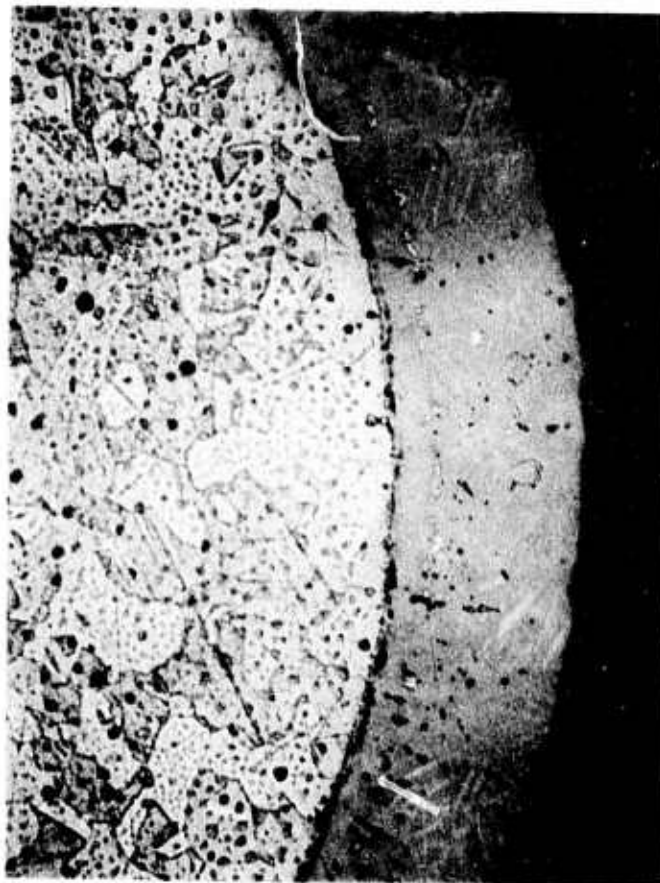


Figure 20. Same as Figure 19. 500 X.

### Conclusions and Future Objectives

(1) Work on the system Nb-Al has been terminated, as it became clear that niobium and aluminum have widely disparate deposition potentials, and are, therefore, incompatible for co-deposition.

(2) Alloys of Nb-Sn were obtained, but the work on this system is only at a very preliminary stage. It is now believed that niobium and tin have close enough deposition potentials to allow them to co-deposit. More work is needed to improve control of stoichiometry and morphology.

(3) Alloys of the Nb-Ge were also obtained, but this work is at a preliminary stage. Germanium was found to be more noble than niobium by about 100 - 200 mV. This difference is close enough so that the two metals can be co-deposited. An advantage of the Nb-Ge system over Nb-Sn and Nb-Al is that when depositing Ge metal alone, it produced a solid, whereas the Al and Sn are deposited as liquid metals at the working temperatures. As liquids, they float to the top of the bath, short-circuiting the electrodes and changing the effective electrode surface areas.

(4) Investigation of the solution of  $K_2SiF_6$  in  $KF - LiF$  will be carried out to study the compatibility of Nb and Si for co-deposition. At present, the superconductor  $Nb_3Si$  can hardly be prepared by other techniques. Non-reproducibility and non-stoichiometric compositions are the general case. However, there is much interest in this compound, as a high superconducting transition temperature, in excess of  $23^\circ K$ , is theoretically predicted for a homogeneous and stoichiometric sample.

### References

1. G. W. Mellors and S. Senderoff, J. Electrochem. Soc. 112, 266 (1965).
2. G. W. Mellors and S. Senderoff, Ibid. 112, 841 (1965).
3. G. W. Mellors and S. Senderoff, Ibid. 113, 60 (1966).
4. G. W. Mellors and S. Senderoff, Ibid. 113, 66 (1966).
5. G. W. Mellors and S. Senderoff, Ibid. 114, 586 (1967).
6. G. W. Mellors and S. Senderoff, Ibid. 118, 220 (1971).
7. C. Decroly, A. Mukhtar, and R. Winand, J. Electrochem. Soc. 115, 905 (1968).
8. W. J. Hamer, M. S. Malmberg, B. Rubin, J. Electrochem. Soc. 112, 750 (1965). and 103, 8 (1956).
9. Iu. K. Delimarskii, and B. F. Markov, Electrochemistry of Fused Salts, The Sigma Press Publishers, New York, N.Y. (1961).
10. G. W. Mellors, and S. Senderoff, J. Electrochem. Soc. 112, 642 (1965).
11. Iu. K. Delimarskii and F. F. Grigorenko, Ukr. Khim. Zh. 22, 567 (1956).
12. H. R. Bronstein and D. L. Manning, J. Electrochem. Soc. 119, 125 (1972).
13. C. F. Baes, Jr., Nuclear Metallurgy, Vol. 15, AIME Symp. on Processing of Nuclear Fuels, pp. 615-644, (1969).
14. O. P. Kolchin and M. A. Vol'dman, Inorg. Materials (USSR) 3, 980 (1967).
15. C. E. Wicks, F. E. Block and U. S. Bur, Mines Bull. 605, 119 (1963).
16. F. M. Hall and S. J. Slater, Australian J. Chem. 21, 2663 (1968).
17. U. Cohen, "Electrodeposition of Nb<sub>3</sub>Al from Molten Salts, I." CMR Report, Stanford University, Stanford, California, (1972).
18. U. Cohen, "Electrodeposition of Nb<sub>3</sub>Al from Molten Salts, II." CMR Report, Stanford University, Stanford, California, (1973).
19. H. W. Jenkins, G. Manantov, and D. L. Manning, J. Electroanal. Chem. 19, 385 (1968).

#### D. Continuous Growth

R. De Mattei

##### Introduction

An important factor in the development of techniques for the continuous growth of crystalline solids during electrochemical crystallization is the control of the interface morphology of the growing solid. Of primary importance in this regard is an understanding of the conditions leading to, and the means of avoiding interface instability, the extreme manifestation being dendritic growth. A dendrite is formed when a microscopic protrusion on the cathode surface has a growth rate which accelerates under the influence of the gradients within the diffusion layer adjacent to that interface. When such a protrusion tip extends far enough from the electrode surface to form its own independent diffusion layer, the dendrite grows at a constant rate.<sup>(1)</sup> See Figure 1.

The mechanism of the deposition process can be broken into two general steps: diffusion of the electrochemically active species to the interface region, and discharge of the electrochemically active species and incorporation of the product into the growing crystallite.<sup>(2)</sup> See Figure 2. As in such series kinetic processes, the rate of the total event, in this case deposition, depends primarily on the slowest step in the kinetic chain. In the case of electrochemical crystallization, this leads to two limiting growth regimes: one in which the diffusion step is the slowest mechanism and one in which interface attachment kinetics dominate. This second condition is most desirable, since the diffusion-limited mechanism favors dendritic growth. The problem thus reduces to finding a set of conditions which will insure

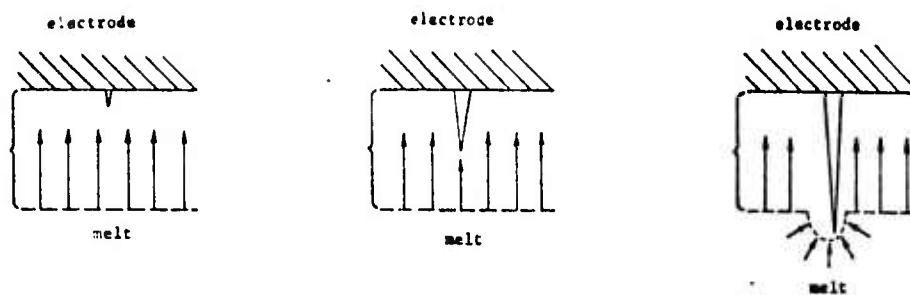


Figure 1. Schematic representation of initiation and growth processes leading to dendrite formation.

Figure 1a. Initiation of surface instability.

Figure 1b. Growth under influence of diffusion layer concentration gradients.

Figure 1c. Formation of independent diffusion layer. Continued growth at linear rate.

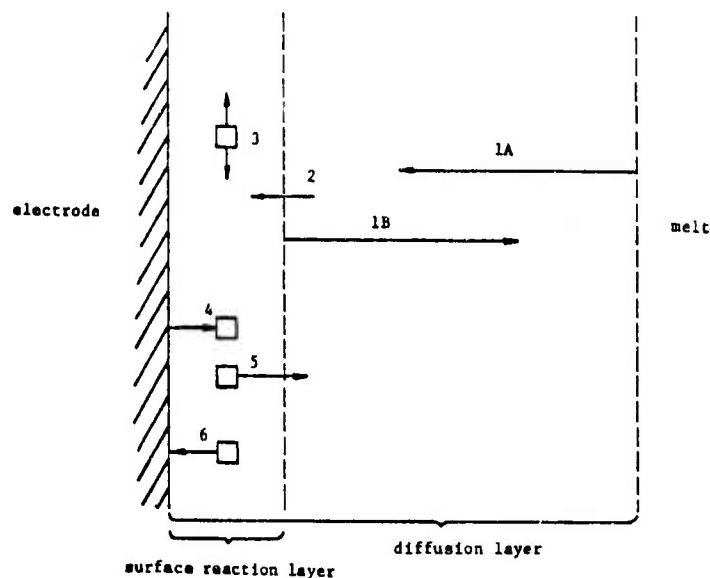


Figure 2. Schematic representation of kinetic processes involved in electrolytic growth.

- 1A Diffusion of solute to electrode interface
- 1B Diffusion of excess solvent, impurities, and electrolysis products away from interface
- 2 Partial desolvation
- 3 Surface diffusion to reaction site
- 4 Electron transfer (single or multistep)
- 5 Diffusion of solvent and electrolysis product away from interface
- 6 Attachment of electrolysis product to interface



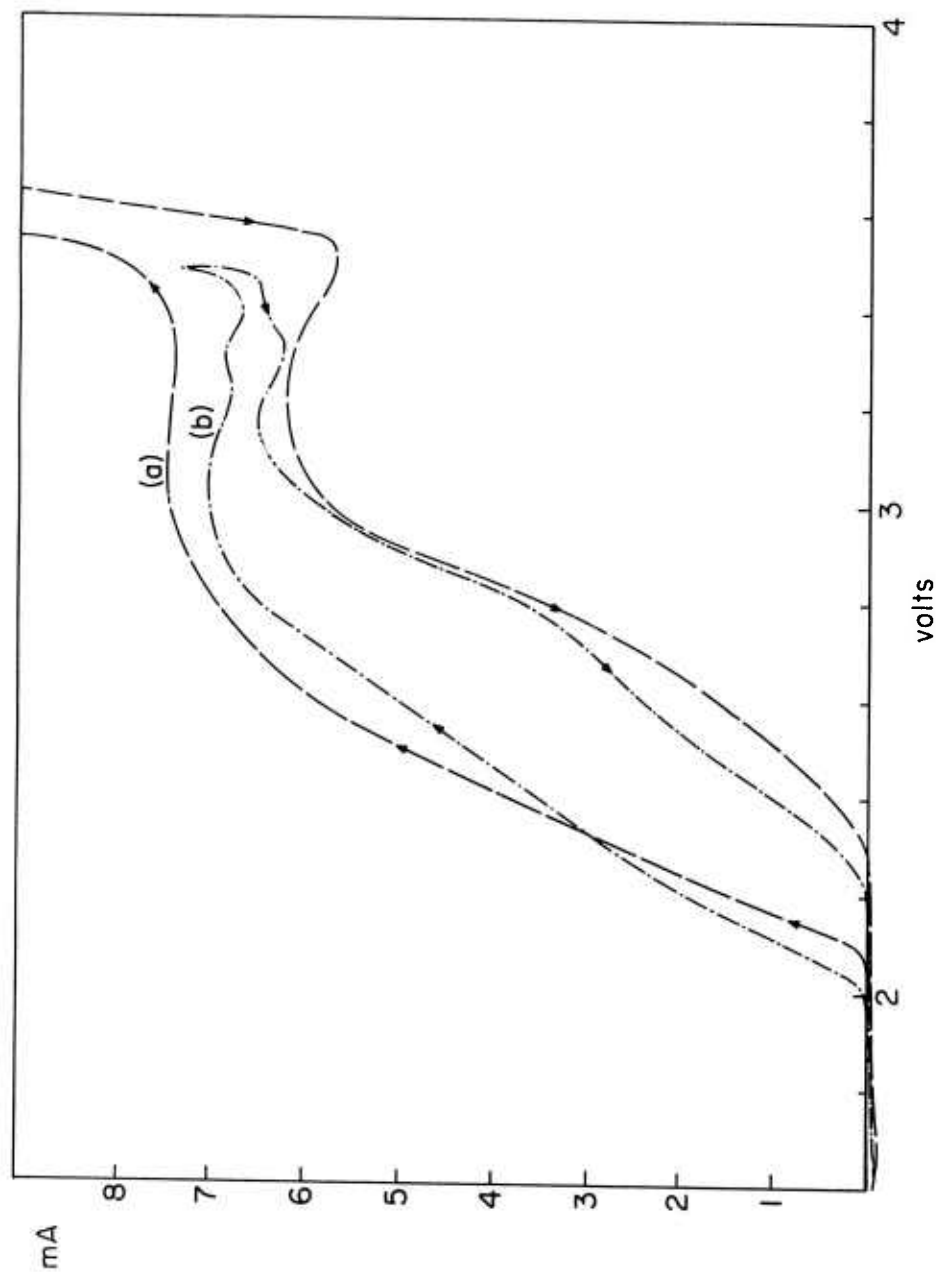


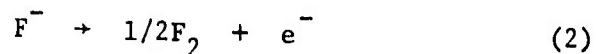
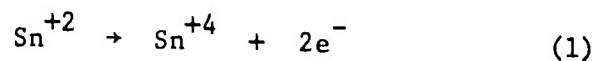
Figure 12. I-V curves of 1.5 mol  $\text{AlF}_3$ .  $t = 520^\circ\text{C}$ ;  
 Au anode; (a)  $v = 33.3 \text{ mV/sec.}$ ;  
 (b)  $v = 8.34 \text{ mV/sec.}$

potential was found to be -3.75V at 600°C, and that  $\text{AlF}_3$  in the solvent is in a complex form such as  $\text{AlF}_6^{-3}$ , which is more stable than pure  $\text{AlF}_3$ , and a higher  $E^\circ$  is required for the decomposition of this complex. The big difference in the deposition potentials explains the fact that codeposition of Al and Nb was never achieved, even at the lowest practical Nb concentration and highest practical Al concentration.

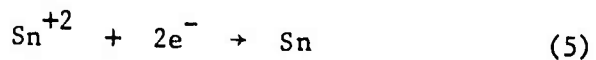
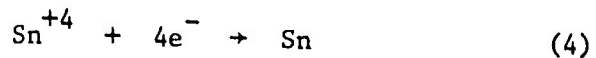
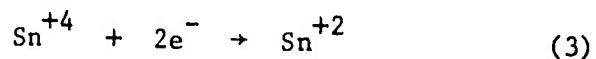
#### 4. Tin Fluoride Decomposition Potential

I-V curves for the decomposition potentials of  $\text{SnF}_2$  in the KF-LiF eutectic were taken. The investigation of this system, however, was only in a preliminary stage, when the compound  $\text{Nb}_3\text{Ge}$  was found to have a superconducting transition temperature of 23°K, and interest shifted to the Nb-Ge system.

Figure 13 and 14 are I-V curves of 0.1%  $\text{SnF}_2$  solution at 655°C. Two rates of scan and two current scales are indicated. The general appearance of the curves is rather complex. Four waves are observed before the solvent decomposition. Sn is known to have two stable valencies,  $\text{Sn}^{+4}$  and  $\text{Sn}^{+2}$ . Since the anode was Au, two anode reactions are possible



The possible cathode reactions are:



rapid transport of the electrochemically active species across the diffusion layer, so that interfacial processes dominate the deposition.

Despic and Purenovic's<sup>(3)</sup> introduction of the concept of a limiting kinetic overpotential for the formation of dendrites gives some insight into the approach to solving the transport problem. This overpotential is given by:

$$\eta_{L,K} = \frac{RT}{\alpha_c F} \ln \frac{nFD}{\delta(x^{1/2}-1)} + \frac{RT}{\alpha_c F} \ln \frac{C_o}{i_o}$$

where  $\alpha_c$  is the cathode transfer coefficient,  $n$  is the number of electrons involved in the electrochemical process,  $D$  is the diffusion coefficient,  $\delta$  is the diffusion layer thickness,  $x$  is the projected experimental time divided by the limiting dendritic induction time,  $C_o$  is the bulk concentration of the electrochemically active species,  $i_o$  is the exchange current density and  $R$ ,  $T$ , and  $F$  have their usual meanings. The larger the value of  $\eta_{L,K}$ , the less the chance for dendritic formation. Since  $\alpha_c$ ,  $n$ , and  $i_o$  are constants of the system under investigation and  $x$  and  $T$  are fixed by choice,  $C_o$ ,  $\delta$ , and  $D$  are free to be varied.

$C_o$  can be increased, but it is subject to certain constraints. The ratio of different electrochemically active species must be maintained such that the desired phase is deposited. The solubility of the components in the melt can limit the concentration increase, as can the melting point of the solution.

Two methods of decreasing the thickness of the diffusion layer,  $\delta$ , have been proposed. Schell and Elwell<sup>(2)</sup> present an equation relating  $\delta$  to the stirred fluid velocity  $u$

$$\delta = Ku^{-1/2}$$

where K is a constant dependent on the viscosity of the solution, its density and the length of the liquid-solid interface. A second method proposed by Despic and Popov<sup>(4)</sup> involves deposition using an applied square wave as the deposition potential. Analysis of the concentration variation with time and application of Nernst's diffusion law gives an expression relating  $\delta$  to the frequency  $\nu$  of the applied potential.

$$\delta = \frac{D^{1/2} \pi^{1/2}}{.606 \nu^{1/2}} = Kv^{-1/2}$$

The diffusion coefficient D can be increased in two ways. The temperature can be increased to increase ion mobility, but care must be taken not to raise the temperature to a point where it can affect the deposit composition as it does in the sodium tungsten bronzes.<sup>(5)</sup> D may also be increased by adding a species to the melt which will lower the viscosity.

Ultrasonic energy introduced into the plating system has also been suggested<sup>(6)</sup> as a means of obtaining good quality deposits. The exact mechanism of this process is not known.

In order to evaluate the effectiveness of some of the above outlined approaches to dendrite suppression, a study of the growth of copper from a low temperature chloride molten salt system was undertaken. This allowed a study of morphological effects and continuous growth under relatively simple conditions. Techniques developed can later be transferred to the more demanding high temperature, atmosphere-controlled systems.

## Research Results

Based on the approaches outlined above, a program was initiated to study the effects of AC potentials, rotating cathodes, and ultrasonic energy on dendrite suppression. Concurrently, an effort was made to continuously pull dendrites from a melt. The first three subsections of this section outline the results of these experiments.

One system suitable for studying the morphology of electrolytically deposited copper is the potassium chloride (KCl) (46 mole %) - zinc chloride ( $\text{ZnCl}_2$ ) eutectic containing 5 mole % cupric chloride ( $\text{CuCl}_2 \cdot 2\text{H}_2\text{O}$ ). This system melts at  $228^\circ\text{C}$  and can be handled in air.

### 1. Deposition in AC Potentials

The first series of experiments were designed to investigate Despic and Popov's<sup>(4)</sup> method of deposition with ac potentials. The results of these experiments were masked under virtually all growth conditions by an "umbrella effect" related to an enhanced rate of dendritic growth near the melt surface. It was found that this phenomenon was most probably due to convective movement of depleted solvent within the diffusion layer, leading to enhanced conditions for dendritic growth near the surface of the melt. See Figure 3.

### 2. Effect of Rotating Cathodes

A second series of experiments to test the effect of a rotating cathode on the characteristics of the deposit were initiated. It was hoped that a reduction in  $\delta$ , the boundary layer width, as suggested by Schell and Elwell<sup>(2)</sup> could be achieved in this manner. The apparatus used allowed cathode rotational speeds of 95, 176, 351, 468, 936, and 1872 rpm. Experiments were

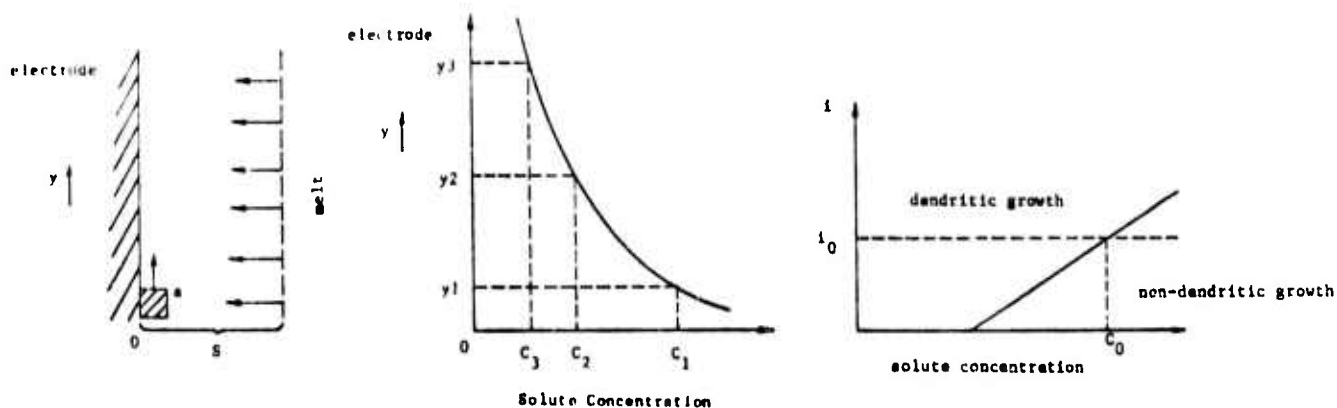


Figure 3. Schematic representation of process leading to umbrella formation.

Figure 3a. Small volume of melt (a) slightly depleted of solute moves in  $y$ -direction due to decreased density. (a) is further depleted as it moves along electrode.

Figure 3b. Schematic plot of solute concentration in depleted region versus vertical position  $y$ .

Figure 3c. Schematic plot of current density ( $i$ ) versus concentration showing region in which dendrites can occur. At an operating current density ( $i_0$ ), under conditions outlined above, a range of morphologies will be obtained on the same electrode.

run using cathodes of both 12 gauge copper wire and 0.25 in diameter copper rod at two different current densities. In all cases, the distribution of the deposit was more uniform from top to bottom with the improvement increasing with rotational speed, Figure 4. Changes in morphology of the deposit were also observed, Figure 5.

### 3. Continuous Pulling of Dendrites

Concurrent with these experiments, copper dendrites were deliberately grown from a 2.5 mole % cupric chloride melt utilizing continuous pulling of the product from the melt. Under proper conditions, dendrites several centimeters long and with morphological variations were obtained, Figure 6.

### 4. Influence of Ultrasonic Energy on Growth Morphology

In order to test the effect of ultrasonic energy on electrochemical deposition, a series of Zn plating experiments was run in an aqueous zincate ( $\text{ZnO}_2^{-2}$ ) solution. An aqueous, rather than molten salt system was chosen initially for the sake of simplicity, as it could be operated at room temperature. The solution used was 10% by weight potassium hydroxide (KOH) in water with 0.1 mole per liter of zinc oxide ( $\text{ZnO}$ ) added. This was electrolyzed in a three-electrode cell with the anode and reference electrode being zinc and the cathode being either zinc or steel. The ultrasonic energy was introduced in one of three ways: (1) on a vibrating cathode (steel, since zinc fractured readily), (2) on an auxiliary rod not involved in the deposition and (3) through the cell bottom. The solution was electrolyzed for two hours at constant current ( $5.4 \text{ ma}$ ,  $2.7 \text{ ma/cm}^2$ ) while both the applied potential and the overpotential were recorded at five minute intervals.



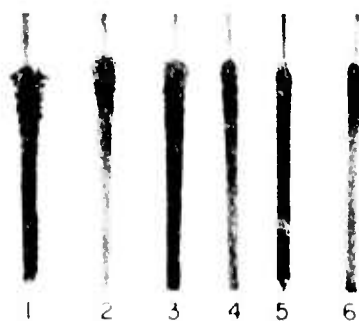


Figure 4. Effect of electrode rotation on deposit distribution.

- From left to right:
- 1)  $i = 3.6 \text{ ma/cm}^2$ , rpm = 0, time = 23 hrs
  - 2)  $i = 3.4 \text{ ma/cm}^2$ , rpm = 94, time = 15 hrs
  - 3)  $i = 4.1 \text{ ma/cm}^2$ , rpm = 176, time = 15 hrs
  - 4)  $i = 3.5 \text{ ma/cm}^2$ , rpm = 468, time = 7 hrs
  - 5)  $i = 3.9 \text{ ma/cm}^2$ , rpm = 936, time = 7 hrs
  - 6)  $i = 4.4 \text{ ma/cm}^2$ , rpm = 1872, time = 6 hrs

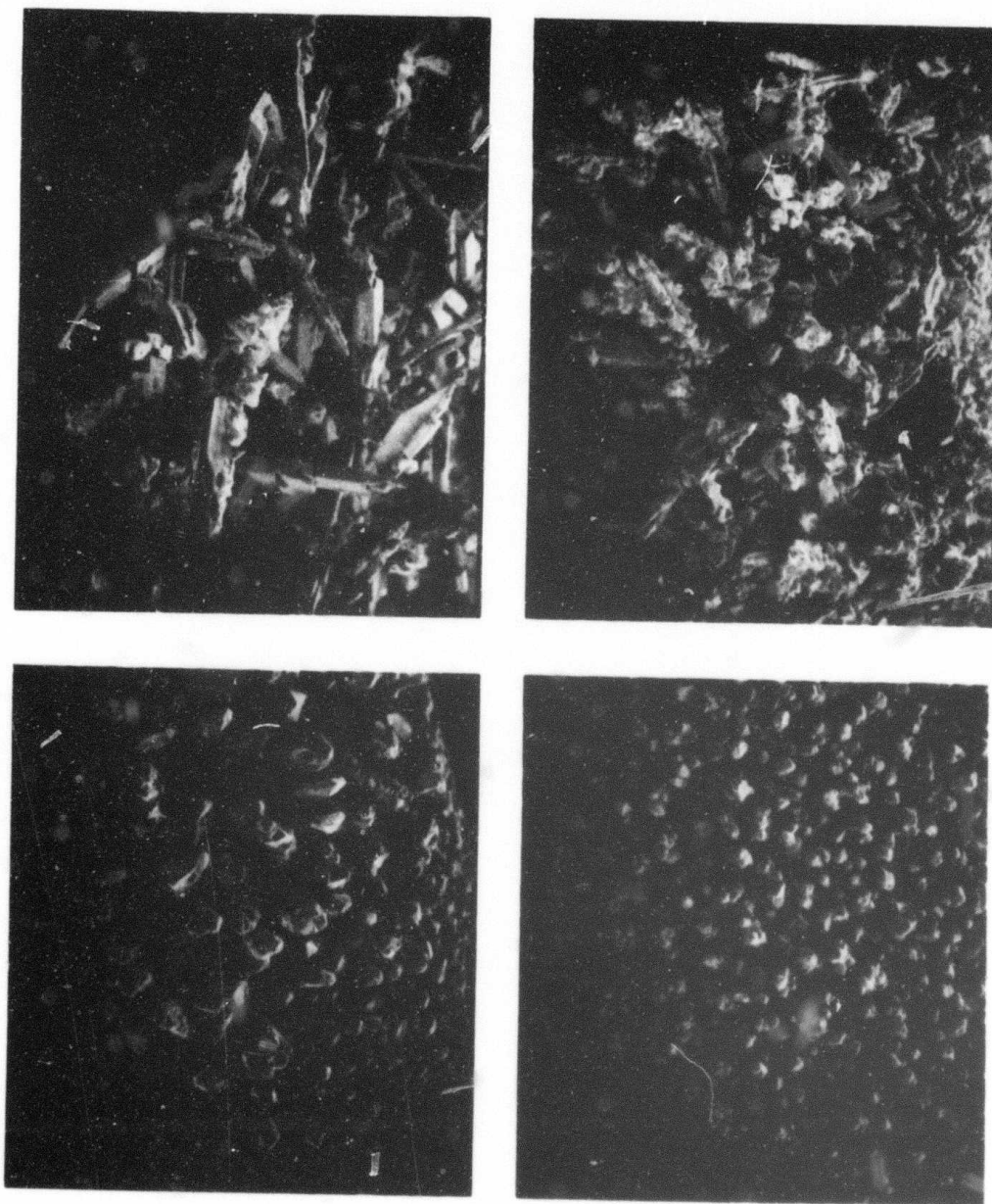
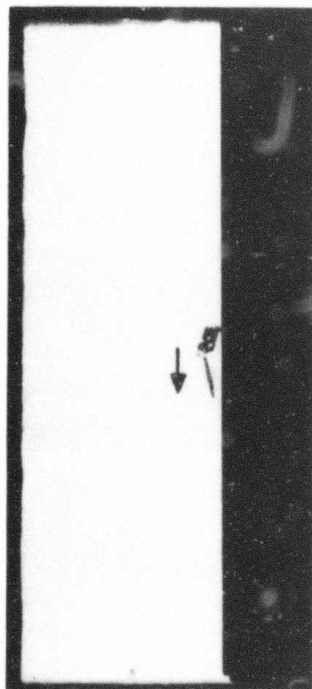
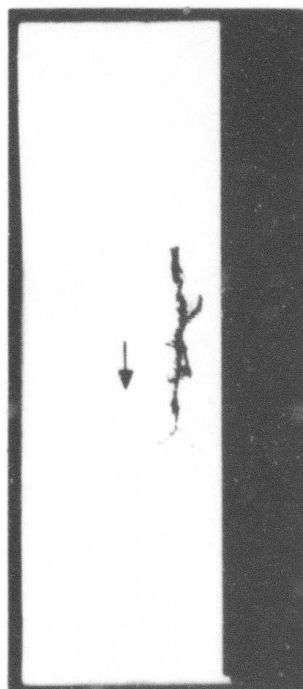
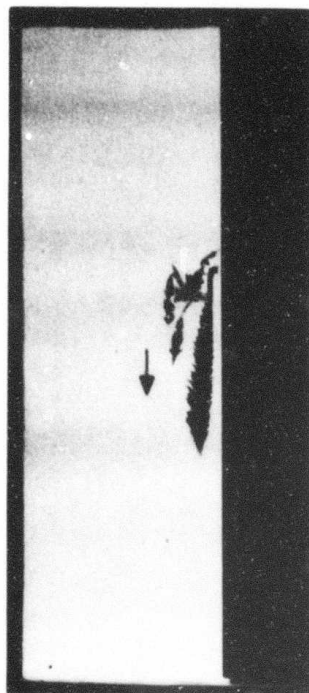


Figure 5. Changes in morphology using rotating electrode.  
20X.

- a)  $i = 5 \text{ ma/cm}^2$ , rpm = 0, time = 17 hrs
- b)  $i = 5 \text{ ma/cm}^2$ , rpm = 94, time = 27.5 hrs
- c)  $i = 5 \text{ ma/cm}^2$ , rpm = 936, time = 20.25 hrs
- c)  $i = 5 \text{ ma/cm}^2$ , rpm = 1872, time = 32 hrs



c)  $I = 30 \text{ ma}$   
 $P = 0.025 \text{ cm/min}$   
 $R = 5 \text{ rpm}$



d)  $I = 30 \text{ ma}$   
 $P = 0.035 \text{ cm/min}$   
 $R = 0 \text{ rpm}$

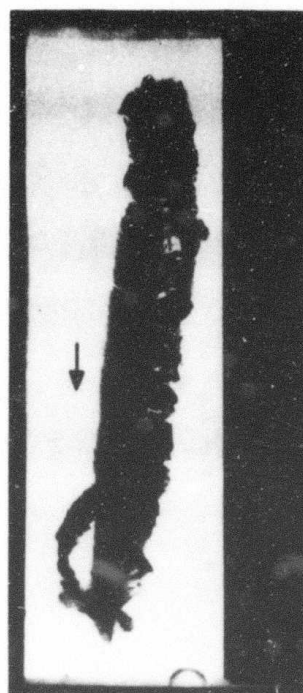


Figure 6. Examples of copper dendrites produced under various conditions. The melt contained was 46 mole %  $\text{KCl}$ , and 54 mole %  $\text{ZnCl}_2$ , plus 2.5 mole %  $\text{CuCl}_2 \cdot 2\text{H}_2\text{O}$ . Arrows indicate growth direction.

Plots of the applied potential and overpotential at 0, 10, 30, 60, and 120 minutes versus ultrasonic power for the vibrating cathode system showed a consistent minimum between the 40% and 50% power setting, Figure 7, (approximately 20-25 watts at 24 KHz). At power levels of 70 to 80%, both potentials became erratic. The cathode efficiency (weight of deposit/weight calculated from Farraday's law) showed a slight improvement at 40% power and dropped to zero at 70% (Figure 8).

The relationship between current density  $i$  and overpotential  $\eta$  is given by<sup>(7)</sup>

$$\eta = \frac{i}{i_o} \frac{RT}{nF} + \frac{i\delta RT}{DC_o F^2 n^2} + \frac{2\gamma V}{nFr}$$

where  $\gamma$  is the interfacial energy between the deposit and the melt,  $V$  is the molar volume of the deposit,  $r$  is the surface radius and the other symbols are as previously defined. Since  $i_o$ ,  $R$ ,  $T$ ,  $n$ ,  $F$ ,  $C_o$ ,  $\gamma$ ,  $V$ , and  $r$  are constant from experiment to experiment and assuming  $i$  at time  $t$  is the same for any power level, then for any two experiments

$$\eta_1 - \eta_2 = \frac{i}{C_o} \frac{RT}{n^2 F^2} \left( \frac{\delta_1}{D_1} - \frac{\delta_2}{D_2} \right)$$

$$\eta_1 - K \frac{\delta_1}{D_1} = \eta_2 - K \frac{\delta_2}{D_2}$$

but if

$$\eta_1 > \eta_2$$

then

$$\frac{\delta_1}{D_1} > \frac{\delta_2}{D_2}$$

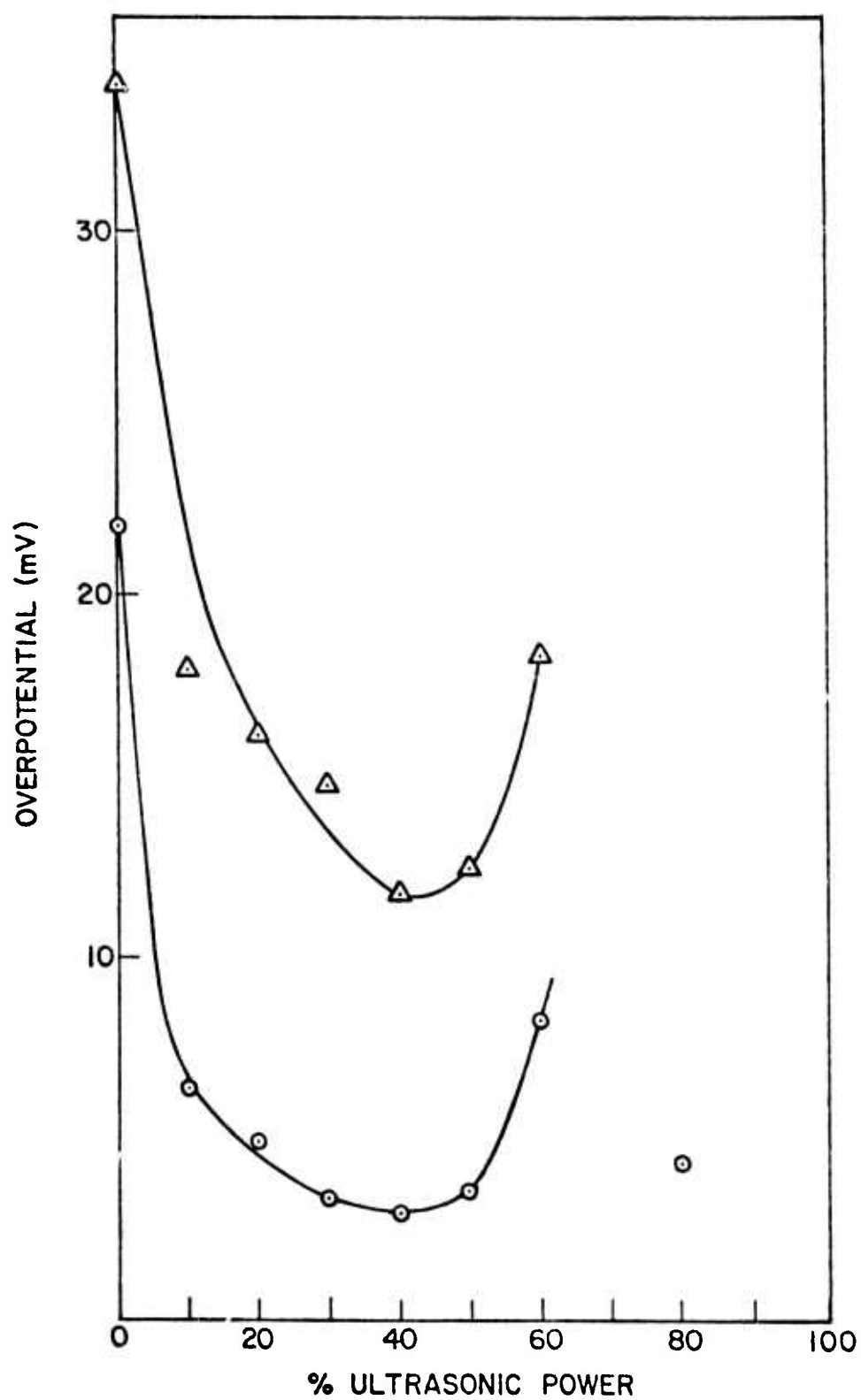


Figure 7. Overpotential and applied potential versus ultrasonic power at time  $t = 120$  minutes.

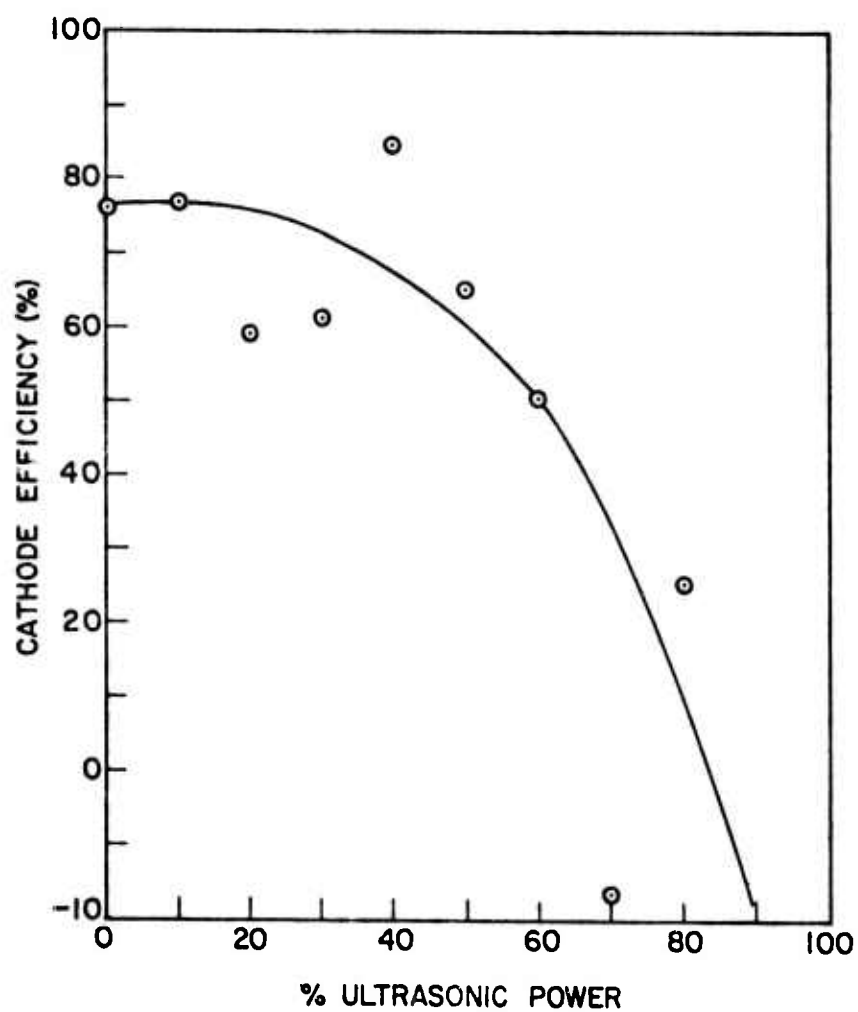


Figure 8. Cathode efficiency versus ultrasonic power.

Thus,  $D_2$  must be greater than  $D_1$ , where  $D_1$  as defined by the experiment may be an effective diffusion coefficient, which includes mass transport due to solution mixing by the ultrasonic energy, and/or  $\delta_1$  must be greater than  $\delta_2$ . These are the conditions necessary to increase the limiting kinetic overpotential for dendrite formation.<sup>(3)</sup> This type of mechanism can explain the overpotential behavior between the 0 and 50% ultrasonic power levels. The changes in overpotential and decrease in cathode efficiency above 50% power may be an indication of the onset of a second reaction induced by the ultrasonic energy. Such reactions have been reported.<sup>(8)</sup>

The data for the other methods of power introduction are not yet complete, owing to equipment limitation, but the same trends as outlined above are observed.

#### Future Plans

As a result of the above experiments, a new approach to the problem of continuous growth and interface (dendrite) control has evolved. The copper and zincate plating systems were only of limited utility because the growth habit during electrochemical crystallization was not well-defined. A new system based on  $\text{Na}_2\text{WO}_4$ - $\text{WO}_3$  melts is now under investigation. Large sodium tungsten bronze crystals ( $\text{Na}_x\text{WO}_3$   $0.1 > x > 1$ ) with well-defined morphologies can be produced from the melts at relatively high growth rates in the presence of suitable electric potentials, Figure 9. The growth of  $\text{Na}_x\text{WO}_3$  crystals from tungstate melts provides a better system for investigating the limits of interface stability, since it is much easier to alter the quality of crystal which can be readily grown under a wide range of

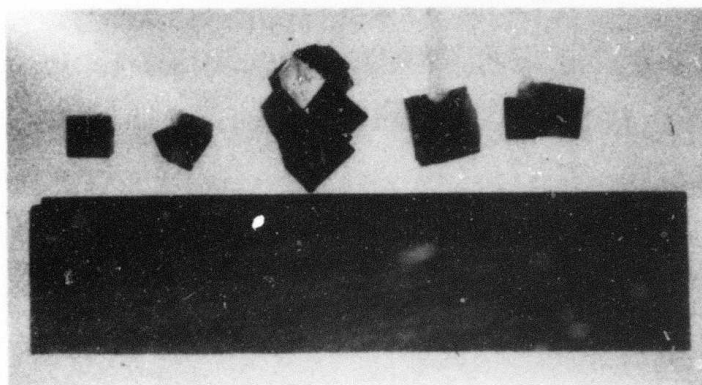


Figure 9. Examples of  $\text{Na}_x\text{WO}_3$  grown from a  $\text{Na}_2\text{WO}_3$  (75 m/o) -  $\text{WO}_3$  melt at  $750^\circ\text{C}$ .

From left to right:

- 1) Applied voltage (v) = 1.11 to 1.20 volts  
Current (I) = 5 ma  
Time (T) = 63.5 hours
- 2) v = 1.25 to 1.18 volts  
I = 20 to 18.8 ma  
T = 23.3 hours
- 3) v = 1.50 to 1.30 volts  
I = 40 ma  
T = 26.4 hours
- 4) v = 1.10 to 1.22 volts  
I = 0.95 to 8 ma  
T = 97.6 hours
- 5) v = 1.17 to 1.22 volts  
I = 5 to 10 ma  
T = 149.4 hours



conditions, than it is to improve the interface stability in a system which is far from yielding stable growth conditions.

Experiments will be designed which will permit continuous pulling of  $\text{Na}_x\text{WO}_3$  from the melt.  $\text{Na}_x\text{WO}_3$  crystals remelt when exposed to air at high temperatures. A study of the appropriate conditions necessary to inhibit remelting has been initiated, along with measurements of the variation in the electrical conductivity of the melt with composition, and the effect of voltage on crystal composition as a function of bath composition. The major thrust of this phase of the program, however, will be specific experiments designed to develop an understanding of and techniques for Czachralski growth of  $\text{Na}_x\text{WO}_3$  with an applied electric potential difference.

### References

- (1) A. R. Despic and K. I. Popov, Modern Aspects of Electrochemistry, Ed. by B. F. Conway and S. O'M. Bockris, Plenum Press, New York, p. 199 (1972).
- (2) H. J. Scheel and D. Elwell, J. Electrochem. Soc. 120, (6), 818.
- (3) A. R. Despic and M. M. Purenovic, J. Electrochem. Soc. 121 (3), 329.
- (4) A. R. Despic and K. I. Popov, J. Applied Electrochem. 1, 275.
- (5) H. R. Shanks, J. Crystal Growth, 13/14, 433.
- (6) C. T. Walker and R. Walker, Electrodeposition and Surface Treat. 1, (6), 457.
- (7) J. L. Barton and J. O'M. Bockris, Proc. Roy. Soc. 268 (A), 485.
- (8) A. Weisslu, Chem. Eng. Prog. - Ultrasonic Symp. 1, 22.